

Strain-induced γ' -coarsening during aging of Ni-based superalloys under uniaxial load: modeling and analysis

Von der Fakultät für Angewandte Naturwissenschaften

der Universität Bayreuth

zur Erlangung der Würde eines

Doktor-Ingenieurs (Dr.-Ing.)

genehmigte Dissertation

von

M. Sc. Leslie T. Mushongera

aus

Bindura, Zimbabwe

Erstgutachter: Prof. Dr.-Ing Heike Emmerich

Zweitgutachter: Prof. Dr. Mathias Göken

Drittgutachter: Prof. Dr. Robert Spatschek

Tag der mündlichen Prüfung: 28.07.2016

Lehrstuhl für Material- und Prozesssimulation

Universität Bayreuth

2016

Abstract

Turbine blades which are used in the hot paths of aerospace or industrial gas turbines are usually manufactured as casted single crystalline parts. However, even though grain boundaries are excluded, the degradation behavior of respectively developed single crystal nickel-base superalloys, is still quite complex involving a number of very different microscopic effects. One of these is the diffusion-limited coarsening of the γ' -precipitates. Long-term aging or creep loading along the $\langle 100 \rangle$ crystallographic orientation results in the anisotropic coarsening of the γ' -precipitates. In the end, the microstructure contains quite large, irregularly shaped precipitates or plate-like precipitates aligned either parallel (P -type rafts) or perpendicular (N -type rafts) to the loading direction. This behavior is detrimental for the properties of these materials since their superior properties emanate from the size, morphology and distribution of the γ' -precipitates [R. Reed: Cambridge University Press, (2006)]. In order to efficiently design these materials, the phenomenon of coarsening should be known in detail to optimize the materials accurately.

On this background, the general objective of this thesis is to develop an integrated computational approach for simulating morphological evolution in single crystal Ni-base superalloys. As a first step towards that aim, a multi-component phase field model coupled to inputs from CALPHAD-type and kinetic databases for the relevant driving forces was developed based on the grand-potential formalism similar to Plapp [Phys. Rev. E, 84: 031601 (2011)]. The thermodynamic formulation of the model was validated by comparisons to ThermoCalc equilibrium calculations and DICTRA sharp-interface simulations. Phase field approaches that allow for anisotropies of the interfacial energy sufficiently high so that the interface develops sharp corners due to missing crystallographic orientations were formulated. This called for a regularization that enforces local equilibrium at the corners, and the method of Eggeleston et al. [Physica D 150, 91 (2001)], generalized to arbitrary crystal symmetries and rotations of the crystalline axes was adapted for that context. Mechanical effects accounting for the contributions from the misfit, anisotropic and inhomogeneous elasticity and creep loading were integrated physically consistent. The mechanical effects are incorporated into the phase field model via the Allen-Cahn equation based on Steinbach [Physica D, 217, 153 (2006)] and Fleck et. al [Philos. Mag., 90, 265 (2010)]. The relaxed displacement fields required to calculate the elastic driving force was obtained by solving the mechanical equilibrium using an iterative Jacobi relaxation scheme using a staggered grid based on the finite difference method.

Morphological evolution and kinetics in single crystal Ni-base superalloys was studied. To gain insight in optimized alloying, a systematic computational measure to assess and track the evolution anisotropic microstructures was integrated in the model. Previously, focusing on the solidification behavior, Heckl et al. [Metal. and Mater. Trans. A, 41, 202 (2010)] discussed Ruthenium (Ru) as a possible Rhenium (Re) replacement-candidate for next generation Ni-based superalloys. Employing phase field simulation studies, we performed virtual experiments of the coarsening behavior in Re and Ru containing alloys. The simulations revealed that the degradation of the γ - γ' microstructure via coarsening is considerably slower in Re-containing superalloys. We observed that an increase in the Re content strongly reduces the γ' -coarsening kinetics and the simulations explicitly resolved the time dependence of that slow down beyond experiment. Likewise, it was found that Ru variations have no significant effect on the coarsening kinetics. The simulations revealed the mechanism by which Re reduces coarsening kinetics. The simulations showed that Re slows interface mobility by accumulating along the path of moving γ/γ' -interfaces, a behavior we attribute to its low diffusivity and low solubility in the γ' -precipitate. The virtual experiments allowed for a systematic quantification of the relative contribution of each solute in a superalloy to coarsening. This can be understood as a first step toward a simulation-based design and optimization of alloy composition.

Contents

List of Figures	iii
List of Tables	v
1 Introduction	1
2 Phase field modeling of interdiffusion-limited transformations on the basis of a grand-potential formalism	8
2.1 Diffuse-interface modeling	9
2.1.1 Thermodynamics	10
2.1.2 Grand-potential density for binary alloys	11
2.1.3 Extension to multicomponent alloys	12
2.2 Phase-field equation	15
2.2.1 Numerical solution	16
2.2.2 Stationary solution	17
2.2.3 Dynamic solution	18
2.3 Multi-component diffusion equations	18
2.3.1 Numerical solution	20
2.4 Model validation: Application to $\gamma \rightarrow \gamma'$ transformation	21
2.4.1 Validation of the interface kinetics	21
2.4.2 Validation of equilibrium multi-component concentration profiles	23
2.5 Conclusion	26
3 Modeling of structural transformations in Ni-base superalloys	28
3.1 Equilibrium precipitate morphologies due to anisotropic interfacial energy	29
3.1.1 Phase-field model	30
3.1.2 Inclusion of anisotropic interfacial energy	32
3.1.3 Numerical implementation	35
3.1.4 Volume preservation	37
3.1.5 Equilibrium shape of a particle in a matrix	38
3.2 Modeling of strain-induced effects	43
3.2.1 Inclusion of mechanical effects	45
3.2.2 Equilibrium morphology of a coherent γ' -precipitate	58
3.2.3 Effect of elastic inhomogeneity on morphological evolution	61
3.3 Conclusion	64
4 Effect of Re on directional γ'-coarsening in commercial single crystal Ni-base superalloys: A phase-field study	67
4.1 Model description	69
4.1.1 Determination and rescaling of input parameters	69
4.2 Multiple γ' -precipitate rafting	73
4.2.1 Characteristics of γ' -rafting in elastically inhomogeneous superalloys	73
4.2.2 Quantification of anisotropic γ' -coarsening kinetics	76
4.3 Isolated γ' -precipitate rafting	79

4.3.1	γ' -rafting kinetics with contributions from solute diffusivity	80
4.3.2	Rate-limiting effect of Re	82
4.4	Conclusion	84
5	Phase-field study of anisotropic γ'-coarsening kinetics in Ni-base superalloys with varying Re <i>and</i> Ru contents	87
5.1	Simulation parameters	90
5.1.1	Thermodynamic parameters	91
5.1.2	Kinetic parameters	92
5.1.3	Material parameters	94
5.2	Coarsening law during non-directional γ' -coarsening	95
5.2.1	Stress-free binary alloys	95
5.2.2	Stress-free multi-component alloys	97
5.2.3	Elastically stressed Ni-base superalloys with different Re contents	99
5.3	Influence of Re <i>and</i> Ru additions on cube \rightarrow plate-like transformation	101
5.4	Conclusion	105
6	Summary	107
7	Zusammenfassung	112
8	Appendix A: Model equations and simulation algorithm	114
9	Appendix B: Coupling of eigenstrain to concentration fields	118
	References	123

List of Figures

1	Strained coherent γ/γ' -interface in a negatively misfitting superalloy.	1
2	Coarsening of the γ' -precipitates in the single crystal CMSX4 at 1273.15 K. The top row is the prediction of coarsening using the phase field method and the bottom row is the experimental observation.	3
3	Illustration of the common tangent plane construction for a ternary alloy (based on [59]). A common tangent plane is connected to both free energy surfaces and this can be used to find a set of tie-lines and a corresponding set of equilibrium compositions.	14
4	Schematic illustration of a DICTRA one-dimensional simulation set-up	21
5	Time evolution of the Al concentration profiles during $\gamma \rightarrow \gamma'$ transformation in a binary Ni-20 wt.%Al alloy. The precipitate evolves until the equilibrium volume fraction of 56% is reached. In the initial stages, the γ' -precipitate grows at a much faster rate due to the presence of a relatively large amount of free Al solutes in the γ -matrix. As the Al solutes become depleted in the matrix the γ' -precipitate growth rate starts to decelerate until it eventually stops.	22
6	Comparison of phase field and DICTRA predictions of γ' -volume fraction during growth in the Ni-9.6wt.%Al alloy at 1273.15 K.	23
7	Evolution of Ta and Cr profiles during γ' -growth in CMSX4 at 1273.15 K.	24
8	Comparison of equilibrium phase concentrations of CMSX4 and CMSX6 obtained from phase-field simulations and ThermoCalc.	25
9	The interface width ξ/ξ_0 as a function of the crystalline orientation angle θ_0 of the rotated anisotropy function	34
10	The dimensionless growth velocity $v/K\mu_0$ as a function of the crystalline orientation angle θ_0 of the rotated anisotropy function	34
11	Illustration of the numerical implementation of the anisotropic phase-field model using a staggered grid.	35
12	Comparison of the equilibrium shapes obtained from the varying interface width formulation and the varying interfacial energy formulation.	38
13	Parametric plot of the anisotropy function $\alpha(\theta)$ and the related Wulff construction.	39
14	Comparison of the parametric Wulff construction and the phase field contours	40
15	Comparison of the rotated Wulff construction with phase field contours.	42
16	Numerical implementation of the mechanical equilibrium using a staggered grid.	53
17	Sphere to cube transition	58
18	Phase-field simulation of microstructural evolution during precipitation of the γ' -phase in Ni-base superalloys at 1273.15 K.	59
19	In this figure, we show the non-dimensional elastic driving force for phase transformation $\delta f_{el}/\delta h$. The elastic driving force is larger along the $\langle 111 \rangle$ -crystallographic directions than along the $\langle 100 \rangle$ -crystallographic directions. The anisotropic elastic driving forces results in faster growth rates along the $\langle 111 \rangle$ -crystallographic directions than along the $\langle 100 \rangle$ -crystallographic directions which gradually transforms the morphology of the γ' -precipitates from the initial spheres to cubes.	60
20	Generation of initial microstructure used in the simulations.	62
21	Morphological evolution during coarsening in an elastically anisotropic and homogeneous system ($C_{ij}^{\gamma'} = C_{ij}^{\gamma}$). (i) $t = 0$ h; (iii) $t = 24$ h; (iii) $t = 48$ h.	63

22	Morphological evolution in an elastically anisotropic and inhomogeneous system ($C_{ij}^{\gamma'} = 0.75C_{ij}^{\gamma}$). (i) $t = 0$ h; (ii) $t = 24$ h; (iii) $t = 48$ h.	63
23	Morphological evolution in an elastically anisotropic and inhomogeneous system ($C_{ij}^{\gamma'} = 0.5C_{ij}^{\gamma}$). (i) $t = 0$ h; (ii) $t = 24$ h; (iii) $t = 48$ h.	64
24	Schematic illustration of solute flux during rafting.	67
25	Concentration field (wt.%) of (a) Ta in CMSX6; (b) Re in CMSX4 after 28 h under a compressive strain ($\varepsilon_a = -0.2\%$) along the [010] direction.	74
26	Time evolution of the γ' -volume fraction during coarsening under no applied strain ($\varepsilon_a = 0.0\%$) and under compressive strain ($\varepsilon_a = -0.2\%$).	75
27	Comparison of the aspect ratio AR calculated using different phase field quantification routines.	77
28	Time evolution of the aspect ratio during rafting in CMSX4 and CMSX6.	78
29	Dimensionless elastic driving force during rafting under a compressive load.	79
30	Time evolution of the aspect ratio AR of an isolated γ' -precipitate for different choices of Re diffusivity \tilde{D}_{Re} during P -type rafting under an applied compressive strain ($\varepsilon_a = -0.2\%$) along the [010] direction.	80
31	Aspect ratios AR of an isolated γ' -precipitate after 5 h of exposure under compression ($\varepsilon_a = -0.2\%$) as a function of the diffusivity of a species.	81
32	Concentration field of Re during rafting under an applied compressive strain ($\varepsilon_a = -0.2\%$) along the [010] direction.	83
33	Coarsening at 1273.15 K in CMSX4 with a misfit of -0.14% at $t = 0, 14, 28, 42$ h. The size of the simulation domain is $3.5 \times 3.0 \mu m^2$. (a) Non-directional coarsening with contributions from misfit and elastic inhomogeneity, (b) Rafting with contributions from misfit, elastic inhomogeneity, and compressive strain $\varepsilon_a = -0.2\%$ applied parallel the (010)-crystallographic direction.	88
34	Cube \rightarrow plate-like transformation of an isolated γ -precipitate during coarsening in CMSX4 under a compressive strain applied parallel the (010)-crystallographic plane.	89
35	Origin of coarsening in a binary Ni-Al alloy.	96
36	Ostwald ripening of spherical precipitates in a multi-component alloy.	98
37	Log-log plot of coarsening kinetics.	100
38	Elastic energy density during cube \rightarrow plate-like transition of precipitate after applying a compressive strain ($\varepsilon_a = -0.2\%$) parallel to the (010)-crystallographic plane. The precipitate elongates along the elastically soft [010]-crystallographic direction.	102
39	Aspect ratios after 5 h of rafting at 1273.15 K as a function of Ru contents for different constant Re and Re contents for different constant Ru.	103
40	Concentration field of Re during rafting under an applied compressive strain ($\varepsilon_a = -0.2\%$) along the [010] direction.	104
41	Simulation of γ' -growth using EP (Eqs. (101-165)) and system number 2 of size of $351 \times 351 \Delta x$ at $t=0, 2.5, 4.5$ and 9.0 hr. The color depicts the elastic driving force for phase transformation.	121
42	Simulation of γ' -growth using EPC (Eqs. (203-211)) and system number 2 of size of $351 \times 351 \Delta x$ at $t=0, 3.5, 6.5$ and 11 hr.	121
43	CPU time to reach the equilibrium precipitate volume fraction for different system sizes for EP (in blue) and EPC (in red). The CPU time for any system size to reach equilibrium is faster for EP than EPC.	122

List of Tables

1	The composition in wt.% of the superalloys under study.	24
2	Standard heat treatment of the CMSX4 sample.	61
3	The composition of the superalloys under study.	70
4	Thermodynamic factors X_i/X_0 for CMSX4, equilibrium diffusion potentials μ_i^{eq}/μ_0 , equilibrium Gibbs free energies $f_{ch}^{p,eq}/f_0$ and equilibrium phase concentrations $c_i^{p,eq}$ (in wt.%) at 1273.15 K.	71
5	Thermodynamic factors X_i/X_0 for CMSX6, equilibrium diffusion potentials μ_i^{eq}/μ_0 , equilibrium Gibbs free energies $f_{ch}^{p,eq}/f_0$ and equilibrium phase concentrations $c_i^{p,eq}$ (in wt.%) at 1273.15 K.	71
6	The scaled diffusion matrix D_{ij}^γ for CMSX4 at 1273.15 K.	72
7	The scaled diffusion matrix D_{ij}^γ for CMSX6 at 1273.15 K.	72
8	Elastic constants (in GPa) used in the simulations.	73
9	Composition of 12 model Ni-base superalloys in wt.%.	90
10	The equilibrium phase compositions (in J/mol) at 1273.15 K.	91
11	The equilibrium diffusion potentials (in J/mol) at 1273.15 K.	91
12	The equilibrium Gibbs free energies (in J/mol) at 1273.15 K.	92
13	Diffusion coefficients (m^2s^{-1}) at 1273.15 K of 12 model Ni-base superalloys.	92
14	Diffusion coefficients (m^2s^{-1}) at 1273.15 K of 12 model Ni-base superalloys (continued).	93
15	Diffusion coefficients (m^2s^{-1}) at 1273.15 K of 12 model Ni-base superalloys (continued).	94
16	Thermodynamic factors X_{ii} (J/mol-at) at 1273.15 K.	94

Nomenclature

δ	Lattice misfit
δ_{ik}	Kroneker's delta
μ_i	diffusion potential field of species i
μ_i^{eq}	Equilibrium diffusion potential of species i
Ω	Grand potential functional
ϕ	Phase field order parameter
σ	Isotropic interfacial energy
σ_{ik}	Elastic stress
\tilde{D}_i	Diffusivity strength
Δx	Grid spacing
ε_{ik}	Elastic strain tensor
ε_{ik}^0	Stress-free strain (eigenstrain) tensor
\vec{u}	Displacement
ξ	Interface width
a	Interfacial length-scale
$C_{ij}^{\gamma'}$	Stiffness tensor for the precipitate phase
C_{ij}^{γ}	Stiffness tensor for the matrix phase
$c_i^{p,eq}$	Equilibrium phase composition of solute i
D_{ij}	Diffusion matrix
F	Free energy functional
$f_{ch}^{p,eq}$	Equilibrium free energy density of phase p
K	Kinetic coefficient
M_{ij}^p	Atomic mobility matrix of phase p
U	Interfacial energy-scale
v	Interface velocity
X_{ij}^p	Thermodynamic factor matrix of phase p

1 Introduction

Technologically relevant single crystal Ni-base superalloys exhibit essentially two phase microstructures consisting of γ' -precipitates coherently embedded in a continuous γ -matrix. In Ni-base superalloys used for high temperature applications such as aero engine or power plant gas turbine blades, the second phase γ' -precipitates are generated through solid \rightarrow solid transformation from the parent γ -matrix. While the continuous γ -matrix has a disordered fcc^1 (A1) crystal structure, the precipitates are of the ordered $fcc(L1_2)$ crystal structure. Due to the different partitioning behavior of solutes, the compositions of the two solid phases are often different. The difference in composition and structural arrangements of the two phases is accompanied by a difference in the lattice parameters. To maintain lattice continuity across the phase boundary, local elastic deformations are required as illustrated in Fig 1 (a) which generates coherency strain energy. The resulting coherency strain energy as illustrated in Fig 1 (b) plays a critical role in determining the transformation path and microstructure evolution during solid-state transformations.

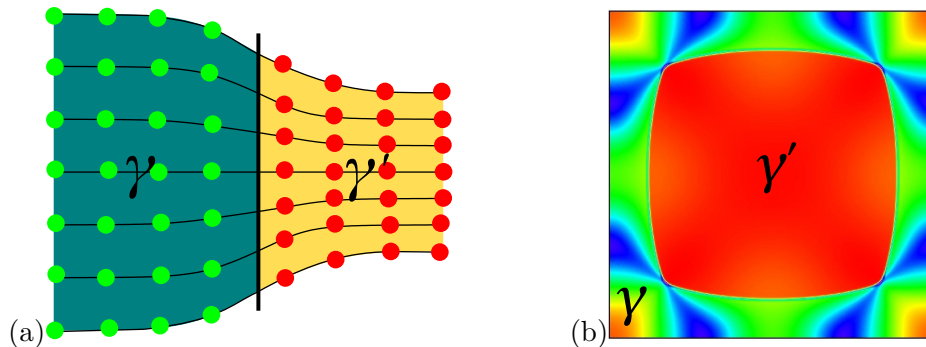


Figure 1: Coherent γ/γ' -interface in a negatively misfitting superalloy. To maintain mechanical continuity across the phase boundary, anisotropic elastic deformations appear in its vicinity. The anisotropic elastic deformations determine the transformation path and microstructure evolution during solid-state transformations.

In a two phase system, the morphology of the second phase γ' -precipitates is determined by the interplay of the isotropic interfacial energy and anisotropic elastic energy. The magnitude of the misfit generally influences the morphology of the γ' -precipitates, e.g., alloys with a zero misfit generally have spherical precipitates whereas those with a non-zero misfit have cuboidal or plate-like precipitates. While the interfacial energy (which is generally isotropic in Ni-base superalloys [48]) favors a spherical precipitate morphology, the elastic energy due to the coherency strain is minimized when the precipitates exhibit a cuboidal morphology as shown in Fig 1 (b) or plate-like precipitates. This statement is equivalent to the stipulation that the strain energy effect be stronger

¹ fcc - face-centered cubic

than the surface effect. A variation of the relative strengths of the two effects would result in a continuous transition from rather spherically shaped particles to equiaxial morphologies [41]. The precipitates acquire morphologies for which the total energy is minimum and the rate at which the morphologies are formed is affected by the kinetics of the transformation which is influenced by the diffusion of solutes in the system.

In the last few years or so, phase field modeling has become an important tool for the quantitative study of microstructure evolution in complex binary and multi-component metallic alloys. Various aspects relevant in materials science ranging from the initial solidification to late-stage solid-state transformations have so far been successfully addressed using phase field modeling techniques as discussed in the review articles by Emmerich [17], Asta et. al [1], and Wang et. al [80]. The major advantage of this approach is given by its great flexibility of modeling, which allows to address even complex systems involving several different physical mechanisms at the same time. The general idea behind phase-field modeling is to include an order parameter, that denotes the phases in a given system. Taking for example a two phase system - the order parameter has a constant value in each bulk phase, e.g., $\phi = 1$ in the matrix phase and $\phi = 0$ in the precipitate phase. Then, the interface between different phases is represented by a smooth transition region where the order parameter varies smoothly from 0 to 1. Thus, the interface width is smeared over a finite width. In contrast to the sharp interface models, the explicit tracking of the interface is unnecessary in phase field modeling. In phase field modeling, free moving interfaces between different phases are not treated as geometric boundaries, i.e. boundary conditions do not have to be applied explicitly at the interfaces. Rather, all the information about the motion and precise location of the phase boundaries is implicitly contained in the phase field, which obeys a partial differential equation that is solved within the whole computational domain [24]. The formulation of a phase field model generally starts from a functional that includes the necessary interfacial, thermodynamic and material descriptions. Depending on the system, as many as possible degrees of freedom can be incorporated in the functional, e.g., thermodynamic, elastic, plastic, magnetic contributions etc.

The general aim of this doctoral thesis is to comprehensively study morphological evolution and respective kinetics in commercial single crystal Ni-base superalloys. For this particular purpose, an advanced phase field simulation tool linked to high quality thermodynamic and kinetic databases that obey the CALPHAD² standard is developed. Using the developed simulation tool we:

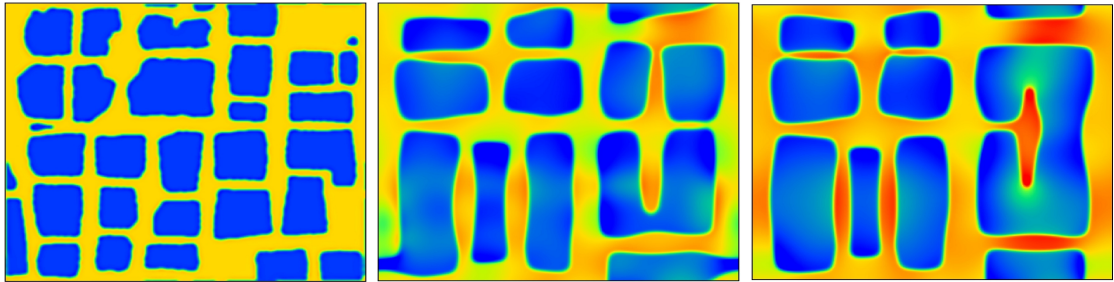
- analyze the contributions from interfacial energy, misfit, anisotropic and inhomogeneous elasticity to (i) non-directional γ' -coarsening and (ii) directional γ' -coarsening, i.e., rafting under external loading applied along a $\langle 100 \rangle$ crystallographic direction,
- perform systematic virtual experiments to identify the influence of refractory el-

²CALculation of PHase Diagrams

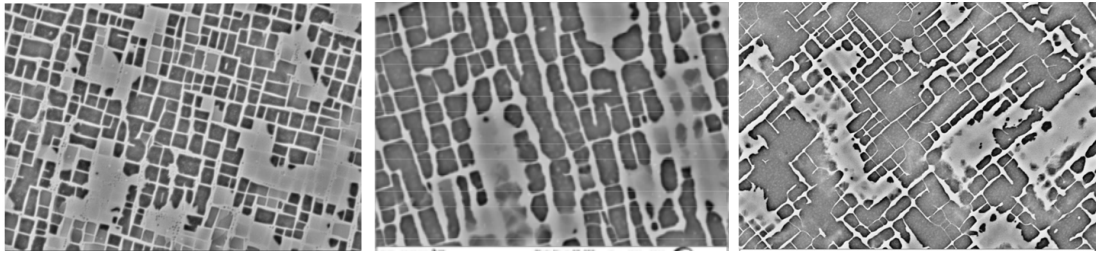
elements like Re, W, Ru, etc., on coarsening and perform a sensitivity studies to optimize alloy chemistry with respect to coarsening,

- identify the mechanism by which elemental diffusion and segregation affect coarsening,
- identify the temporal law during coarsening in elastically stressed multi-component alloys.

Most phase field models for solid→solid transformations are limited to the case of the technologically less interesting Ni-Al binary alloy. As a result, the contributions of inter-diffusion to coarsening have largely been ignored in the numerical studies. Nonetheless, a number of experimental studies, amongst them [32, 63, 86], reveal a substantial contribution from diffusion-particularly in the γ -matrix to the kinetics of phase transformations in Ni-base superalloys. Most phase field models focus mainly on the mechanics, however, to efficiently simulate microstructural evolution in Ni-base superalloys, it is vital not to neglect the relevant contribution from multi-component thermodynamics. Although Ni-



(a) Phase field simulation of non-directional γ' -coarsening showing the segregation of solutes.



(b) SEM photographs of the time evolution during long-term aging at $t=0, 250$ and 500 h [44].

Figure 2: Coarsening of the γ' -precipitates in the single crystal CMSX4 at 1273.15 K. The top row is the prediction of coarsening using the phase field method and the bottom row is the experimental observation.

Al alloys can be used as a pseudo for the analysis of the more chemically complex Ni-base superalloys; binary and multi-component alloys are totally different systems. Ni-base superalloys can contain up to a dozen alloying elements, which results in a more complex

chemical and mechanical behavior of Ni-base superalloys under thermo-mechanical exposure. To accurately simulate the microstructure evolution in Ni-base superalloys with the realistic kinetics, it is important to take into account the contributions of the diffusivities and partitioning behaviors of all alloying elements. It is one of the key results of this work that certain elements, particularly the refractory elements may have a large impact on the nature and kinetics of coarsening, even when they are present in the alloys in relatively small amounts. In this thesis, single crystal Ni-base superalloys with up to 8 alloying components are numerically studied.

This thesis is organized as follows:

Chapter 2, presents the derivation and validation of the multi-component thermodynamic formulation of the phase field model. The multi-component thermodynamic formulation is extended based on the model for binary alloys derived from a grand-potential functional [58]. The extended phase field model uses inputs from the commercial TTNi8³ and MobNi1⁴ databases for the thermodynamic and kinetic driving forces, respectively. Due to the absence of kinetic data for the γ' -phase, symmetric diffusion matrices are adopted in the model for both the γ -matrix and γ' -precipitates. Using a symmetric model for diffusion eliminates the need to incorporate the anti-trapping current in the diffusion equations. The Allen-Cahn equation and set of diffusion equations are solved numerically on uniform square grids using explicit finite-difference methods.

The crystalline nature of solids results in the anisotropy of many thermo-physical parameters like the interfacial energy, lattice misfit, elastic anisotropy etc [10, 41, 59]. Some of the parameters vary with different crystallographic orientations and their orientational dependence determines certain material properties. The morphology of γ' -precipitates is determined by the interplay between interfacial energy and the coherency strain energy; these can be anisotropic to varying strengths depending on the material system [26, 41]. How to incorporate the anisotropy of these two contributions is the challenge in phase field modeling. How to incorporate the anisotropic interfacial and elastic energies is done in **chapter 3**. First, we study two approaches of including a highly anisotropic interfacial energy in phase field models. We use approaches that allow for anisotropies sufficiently high so that interface develops sharp corners due to missing crystallographic orientations: the classical one that allows for the interface to vary with orientation and more recent formulation that has a constant interface width. Second, an approach of incorporating mechanical effects in phase field models is formulated and implemented. For solid-state transformations in Ni-based superalloys e.g., precipitation, coarsening etc., we have to account for at least elastic contributions arising from the misfit and elastic inhomogeneity in addition to the surface effects and thermodynamics. We use the approach of Steinbach et al. [69] to model the dependence of the total strain on the phase field by postulating equal elastic stresses in the two bulk phase at the interface region. In this approach, elastic inhomogeneity and anisotropy are incorporated by assuming a phase dependence of the cubic elastic constants. We demonstrate that both a

³ThermoTech

⁴Thermo-Calc Software AB

high anisotropy of the interfacial energy and anisotropic elasticity lead to cuboidal precipitate morphologies. However, the incorporation of the two anisotropies in one phase field model requires precise knowledge of their relative weighting.

In **chapter 4**, the influence of rhenium (Re) on the kinetics of coarsening is studied. For a comparative study, two single crystal superalloys are simulated; the Re-containing CMSX4 and the Re-free CMSX6. Phase field simulations are done for two cases: with contributions from (i) isotropic interfacial energy, misfit and elasticity inhomogeneity (ii) isotropic interfacial energy, misfit and elasticity inhomogeneity and under external loading along a $\langle 100 \rangle$ crystallographic direction. For the sake of comparison, the initial microstructure for the phase field simulations is obtained from SEM⁵ photographs of “as-heat” treated samples of CMSX4 and CMSX6. The results are compared qualitatively to the experimental observations e.g., in the case of non-directional coarsening in Fig 2b. The idea to numerically study the influence of Re on coarsening is motivated by the experimental studies [32, 63, 86] which observed a marked reduction of the coarsening kinetics due to Re additions. To characterize the kinetics of coarsening, a quantification routine is integrated in the simulation tool. The formation of vastly irregularly shaped precipitates during coarsening presents a problem in finding a global measure that quantifies the evolution of such a microstructure. The quantification routine in this work uses the aspect ratio calculated on the basis of interface orientations as the global measure. A unique feature of this routine is that it quantifies at each time step, the coarsening of anisotropic and coalesced precipitates.

In **chapter 5**, virtual experiments to determine the influence of varying rhenium (Re) and ruthenium (Ru) additions on the kinetics of coarsening are done. The experiments are performed on 12 different virtual superalloys, with systematically varied Re *and* (Ru) contents. The decision to jointly vary the Re and Ru additions is motivated by the studies [12, 35, 36], which proposed Ru as a possible Re replacement-candidate to reduce the formation of the detrimental topologically close packed phases during solidification. Given the identified positive role of Ru in suppressing the formation of the detrimental phases, simulations are done to reveal its influence on coarsening. Additionally, in this chapter, we perform studies to identify the temporal law during the non-directional coarsening of the virtual superalloys. Coarsening kinetics in technical alloys is generally quantified using the classical LSW⁶-theory [49, 75]. The classical theory was based on the strict assumptions of a vanishing volume fraction of stress-free coherent precipitates in binary systems. Given the long recognized role of elastic fields during solid-solid transformations, we discuss the applicability of the LSW-theory to multi-component alloys with an elastic misfit. We extend the classical LSW-theory for binary alloys to multi-component diffusion based on scaling argument similar to the one established by Müller-Krumbhaar [53]. We demonstrate the principle feasibility of our simulation tool in identifying the coarsening exponents during non-directional coarsening.

⁵Scanning Electron Microscopy

⁶ Lifshitz, Slyosov and Wagner theory

Finally, **chapter 6** gives a comprehensive conclusion of the thesis by discussing the results and the potential of the phase field model for further extensions and applications.

In this thesis, a step-wise development of a quantitative phase-field model for modeling microstructural evolution in multi-component systems is presented. The step-wise development is categorized into three sub-divisions listed as:

- *Formulation and validation of multi-component thermodynamics*; this is based on the numerical calculation of Eqs. (30)-(47), giving rise to the results in chapter 2.
- *Coupling of anisotropic effects* in chapter 3 which is subdivided as:
 - inclusion of anisotropic surface effects done in Eqs. (50)-(67). The resulting model formulations are used to study equilibrium morphologies in solid-solid systems,
 - inclusion of anisotropic and inhomogeneous elastic effects resulting in model equations (109)-(119) which are the basis of the applied studies in chapters 4 and 5.
- *Application to solid-state transformations in Ni-base superalloys*: The application of the equations (109)-(119) is done in chapter 4 and 5 to study microstructural evolution in commercial Ni-base superalloys.

Apart from being of scientific importance via aiding the understanding the behavior of metallic alloys, the thesis casts a foundation of basic knowledge required for the development of a quantitative simulation tool, highlighting the limitations and challenges to be overcome in the development.

Some parts of this thesis have been published in the following:

- L. Mushongera, M. Fleck, J. Kundin, and H. Emmerich. Effect of Re on directional γ' -coarsening in commercial single crystal Ni-base superalloys: A phase field study, *Acta Mater.*, 93:60, 2015
- L. Mushongera, M. Fleck, J. Kundin, F. Querfurth, and H. Emmerich. Phase-field study of anisotropic γ' -coarsening kinetics in Ni-base superalloys with varying Re and Ru contents, *Adv. Eng. Mater.*, DOI: 10.1002/adem.201500168, 2015.
- J. Kundin, L. Mushongera, and H. Emmerich. Phase-field modeling of microstructure formation during rapid solidification in Inconel 718 superalloy, *Acta Mater.* 95, 343, 2015.
- J. Kundin, L. Mushongera, T. Göehler, and H. Emmerich. Phase-field modeling of the gamma prime coarsening behavior in nickel based superalloys. *Acta Mater.*, 60:3758, 2012.
- M. Fleck, L. Mushongera, D. Pilipenko, K. Ankit, and H. Emmerich. On phase-field modeling with a highly anisotropic interfacial energy. *Eur. Phys. J. Plus*, 126:95, 2011.

2 Phase field modeling of interdiffusion-limited transformations on the basis of a grand-potential formalism

Phase field methods based on the Allen-Cahn and/or Cahn-Hilliard equations have been used extensively for studying microstructural evolution in elastically stressed solids (see review by Wang et al. [80]). Various phase field formulations have been derived to study phase transformations in Ni-base superalloys. For example, phase field models formulated on a purely elasticity framework [33, 44, 48], have been used to study non-directional coarsening and rafting in Ni-base superalloys. In these models, the mechanical effects are incorporated by coupling an elastic energy term to the free energy. On another level, phase field models with contributions from plastic strains [6, 88, 89, 90, 92] have also been developed to study rafting. In these models, plastic effects are included by adding an eigenstrain in the elastic energy term that accounts for the dislocations in the system. Furthermore, [30] has used an elasto-viscoplastic model to study microstructure evolution under creep loading in Ni-base superalloys. All the models formulated using these various frameworks [6, 30, 33, 48, 88, 89, 90, 92] converge in identifying the lattice misfit, elastic inhomogeneity and applied load as the driving forces for rafting. The resulting microstructures obtained using the different approaches are also qualitatively similar although quantitative comparisons [89] have revealed that the kinetics of evolution does differ. The mechanical effects of the phase field model in this work are incorporated on an elastic framework similar to [44, 69].

Most of the phase field models are limited to the case of the binary Ni-Al system. Although binary Ni-Al alloys can be used as a pseudo for the analysis of the more chemically complex Ni-base superalloys, the binary and multi-component alloys are totally different. Ni-base superalloys can contain up to a dozen alloying elements. This results in a more complex chemical and mechanical behavior of Ni-base superalloys under high temperature exposure. To accurately simulate the microstructure evolution and capture the realistic kinetics in Ni-base superalloys, it is important to develop a multi-component phase field model that takes into account the contributions of the diffusivities and the segregation behavior of all alloying elements.

The aim of this chapter is to develop a numerical tool that can be used to analyze the moving boundary problem involving multi-component solute interactions. The thermodynamic formulation presented in this chapter shall be the basis of the model extension in the following chapter. The multi-component thermodynamic formulation of the model is extended based on the model for binary alloys [58]. A symmetrical model for diffusion, i.e., equal diffusion matrices for the matrix and the precipitates, is used in the simulations. To test the ability of the model to capture the correct kinetics in a multi-component system, phase field and DICTRA/ThermoCalc⁷ simulations are compared for the simple case of a $\gamma \rightarrow \gamma'$ phase transformation at a temperature of 12713.15 K. The results show a convincing quantitative agreement between the sharp interface and diffuse interface models.

⁷Thermo-Calc Software AB

This chapter is organized as follows; in the following, the extension of the binary model [58] to a multi-component model is presented. This is followed by the derivation of the explicit model equations and formulation of their numerical solutions based on the finite difference method (FDM). The thermodynamic consistency of the model is then tested by comparing phase-field simulations of $\gamma \rightarrow \gamma'$ transformation against DICTRA and ThermoCalc simulations.

Part of this chapter is published in [L. Mushongera, M. Fleck, J. Kundin, and H. Emmerich, *Acta Mater.*, 93:60, 2015].

2.1 Diffuse-interface modeling

A non-conserved field variable $\phi(\vec{x}, t)$ is introduced to describe the coherent two phase γ/γ' microstructure of Ni-base superalloys. Fixed values of the phase field variable ϕ are assigned to represent the two coherent phases, 1 for the matrix and 0 for the precipitate. Furthermore, the interface between the two bulk phases is postulated to be smooth and smeared over a finite width. In general, the basic starting point for the derivation of phase field models is a relevant thermodynamic potential to which various degrees of freedom are coupled. In this work, a grand-potential functional whose mesoscopic variables are ϕ and μ , is introduced to describe the γ/γ' microstructure. The grand-potential formalism is based on the work of Plapp [58]. The grand-potential functional is given as the integral of the grand-potential densities of a given volume domain

$$\Omega[\phi(\vec{x}, t)] = \int_V \omega(\phi, \mu, T) dV, \quad (1)$$

on the region V . We consider the grand-potential density to be a sum of the interfacial and thermodynamic grand-potential densities

$$\omega(\phi, \mu) = \omega_{int}(\phi, \nabla\phi) + \omega_{ch}(\phi, \mu). \quad (2)$$

Since the aim of this chapter is to test the thermodynamic formulation of the model via analytical and DICTRA simulations, we limit to the interfacial and thermodynamic terms. For now, we ignore elastic effects. The issue of incorporating elastic effects in the phase field model shall be discussed in the following Chapter 3. The interfacial grand-potential density is described as

$$\omega_{int}(\phi, \nabla\phi) = \frac{3\sigma\xi}{2}(\nabla\phi)^2 + \frac{6\sigma}{\xi}g_{dw}(\phi), \quad (3)$$

allows for the formation of two bulk domains with values $\phi = 0$ and $\phi = 1$ separated by interfaces which are smeared over a finite width. The parameter σ corresponds to the equilibrium interface energy and ξ is the interface width. The term $\nabla\phi$ is the gradient energy and is a double well potential function that guarantees that the grand-potential functional has two minima, at $\phi = 0$ and $\phi = 1$ corresponding to the bulk phases. The gradient energy term and the double well potential determine the interface in a

counteracting manner; the interface tends to be sharp to reduce the regions where the interfacial grand-potential density is positive. The interfacial grand-potential density $g_{dw}(\phi)$ is positive when $0 \leq \phi \leq 1$; as a counteracting effect, the interface tends to be diffuse to reduce the the energy associated with the gradient of the phase field [4]. The assignment of fixed values to represent the two coherent phases, 1 for the matrix and 0 for the precipitate requires that the double well potential $g_{dw}(\phi)$ has two minima, at 0 and 1, thus

$$g_{dw}(0) = g_{dw}(1), \quad (4)$$

$$\left. \frac{\partial g_{dw}}{\partial \phi} \right|_{\phi=0,1} = 0, \quad (5)$$

$$\left. \frac{\partial^2 g_{dw}}{\partial \phi^2} \right|_{\phi=0,1} > 0. \quad (6)$$

The above stipulated conditions satisfy the common tangent construction. A simple choice of a double well potential is

$$g_{dw}(\phi) = \frac{6\sigma}{\xi} \phi^2(1 - \phi)^2. \quad (7)$$

This potential represents an equilibrium two phase scenario whereby the two bulk phases corresponding to the equally deep wells have the same grand-potential densities. However, this scenario is rather unphysical in material systems. A rather more physical system is that which represents two phases with different thermodynamic grand-potential densities. This representation can be achieved by inclusion of an interpolation function to couple the different thermodynamic grand-potential densities. Addition of interpolated thermodynamic grand-potential densities to the double well potential as in Eq. (2) tilts it by an amount that is proportional to the local driving force for phase transformations [25]. In this case, one phase is favored to grow at the expense of the other.

2.1.1 Thermodynamics

The thermodynamic contribution $\omega_{ch}(\phi, \mu)$ in Eq. (1) is postulated as the interpolation of the bulk grand-potential densities

$$\omega_{ch}(\phi, \mu) = \omega_{ch}^{\gamma}(\mu)h(\phi) + \omega_{ch}^{\beta}(\mu)h(1 - \phi), \quad (8)$$

where an interpolation function $h(\phi)$ is used to describe material properties. The interpolation function should vary smoothly between the fixed values, $\phi = 0$ and $\phi = 1$ and should satisfy the conditions

$$\begin{cases} h(0) & = 0 \\ h(1) & = 1 \\ \left. \partial_{\phi} h(\phi) \right|_{\phi=0,1} & = 0. \end{cases} \quad (9)$$

A third order polynomial of type

$$h(\phi) = \phi^2(3 - 2\phi), \quad (10)$$

that satisfies the above conditions is chosen as the interpolation function. The thermodynamic grand-potential densities of the phases can be obtained by a Legendre transform of the free energies [58]

$$\omega^p(\mu) = f_{ch}^p(c, T) - \mu c^p, \quad (p = \gamma \text{ or } \gamma'), \quad (11)$$

where $f_{ch}^p(c, T)$ is the parabolic free energy of phase p .

2.1.2 Grand-potential density for binary alloys

We start by looking at the construction of parabolic free energies for binary alloys similar to Plapp [58]. For a binary alloy, the free parabolic wells in concentration for the bulk phase p is described as

$$f_{ch}^p(c^p, T) = \frac{1}{2}X^p(c^p - A^p)^2 + B^p, \quad (p = \gamma \text{ or } \gamma'), \quad (12)$$

The first derivative of the free energy (12) with respect to the concentration yields its diffusion potential

$$\begin{aligned} \mu &= \frac{\partial f_{ch}^p(c, T)}{\partial c} \\ &= X^p(c^p - A^p). \end{aligned} \quad (13)$$

The phase dependent constants A^p and B^p are related to the equilibrium compositions $c^{p,eq}$ which are evaluated via the common tangent construction. The second derivative of the free energy (12) with respect to the concentration

$$\begin{aligned} X^p &= \frac{\partial}{\partial c} \left(\frac{\partial f_{ch}^p}{\partial c} \right) \\ &= \frac{\partial}{\partial c} \left(\underbrace{\frac{\partial f_{ch}^p}{\partial c}}_{\mu} \right) = \frac{\partial \mu}{\partial c}, \end{aligned} \quad (14)$$

yields the thermodynamic factor. This value corresponds to the curvature of the free energy curves of the phases. The thermodynamic factor can be calculated for a specific alloy and temperature from DICTRA/MobNi1 database. As a standard condition for thermodynamic stability of the parabolic free energy of phase p (12), the condition

$$X^p = \frac{\partial}{\partial c} \left(\frac{\partial f_{ch}^p}{\partial c} \right) > 0, \quad (15)$$

should be satisfied. Inserting equation (13) into (12) yields an expanded form of the parabolic free energies

$$\begin{aligned}
f_{ch}^{ph} &= \frac{1}{2}X^p(c^p - A^p)^2 + B^p \\
&= \frac{1}{2}\underbrace{X^p(c^p - A^p)}_{\mu}(c^p - A^p) + B^p \\
&= \frac{1}{2}\mu(c^p - A^p) + B^p.
\end{aligned} \tag{16}$$

Inserting (16) in the Legendre transform (11), we get the thermodynamic grand-potential density of a phase p for a binary alloy

$$\begin{aligned}
\omega^p(\mu) &= f_{ch}^p - \mu c^p \\
&= \frac{1}{2}\mu(c^p - A^p) + B^p - \mu c^p \\
&= -\frac{1}{2}\mu(c^p + A^p) + B^p \\
&= -\frac{1}{2}\mu\left(\frac{\mu}{X^p} + 2A^p\right) + B^p \\
&= -\frac{1}{2}\frac{\mu^2}{X^p} - \mu A^p + B^p.
\end{aligned} \tag{17}$$

Inserting (17) for each phase in (8), we get the explicit form of the thermodynamic contribution for a binary system

$$\begin{aligned}
\omega_{ch}(\phi, \mu) &= \omega_{ch}^\gamma(\mu)h(\phi) + \omega_{ch}^{\gamma'}(\mu)h(1 - \phi) \\
&= \left(-\frac{1}{2}\frac{\mu^2}{X^\gamma} - \mu A^\gamma + B^\gamma\right)h(\phi) \\
&\quad + \left(-\frac{1}{2}\frac{\mu^2}{X^{\gamma'}} - \mu A^{\gamma'} + B^{\gamma'}\right)h(1 - \phi).
\end{aligned} \tag{18}$$

In the following, we now extend this formulation to multi-component systems. The situation will naturally be different due multiple solute interactions and the presence of thermodynamic factor matrices for the two phases.

2.1.3 Extension to multicomponent alloys

Now we extend the formulation of [58] for binary alloys by including the multiple solute interactions. The parabolic free energy of phase p in a multi-component system becomes

$$f_{ch}^p(c^p, T) = \sum_i \left(\frac{1}{2} \sum_j \chi_{ij}^p (c_i - A_i^p)^2 \right) + B^p, \quad (p = \gamma \text{ or } \gamma'), \tag{19}$$

where i and j are the species in a multi-component system. The first derivative of the

free energy with respect to the concentration yields its diffusion potential

$$\begin{aligned}\mu_i &= \frac{\partial f_{ch}^p(c, T)}{\partial c} \\ &= \sum_j \chi_{ij}^p (c^p - A^p),\end{aligned}\tag{20}$$

Inserting the expression for the chemical potential (20) in the parabolic free energy of a multi-component system (19) yields

$$\begin{aligned}f_{ch}^p(c^p, T) &= \sum_i \left(\frac{1}{2} \sum_j \chi_{ij}^p (c_i - A_i^p)^2 \right) + B^p, \\ &= \sum_i \left(\frac{1}{2} \underbrace{\sum_j \chi_{ij}^p (c_i - A_i^p) (c_i - A_i^p)}_{\mu_i} \right) + B^p, \\ &= \sum_i \left(\frac{1}{2} \mu_i (c_i - A_i^p) \right) + B^p.\end{aligned}\tag{21}$$

Using the Legendre transform (11), we get the grand-potential density of a phase p

$$\begin{aligned}\omega^{ph}(\mu) &= f_{ch}^{ph} - \sum_i \mu_i c_i^{ph} \\ &= -\frac{1}{2} \sum_i \mu_i \left(\sum_j \chi_{ij}^p \mu_j + 2A_i^{ph} \right) + B^{ph} \\ &= \sum_i \left[-\frac{1}{2} \sum_j \chi_{ij}^p \mu_i^2 - \mu_i A_i^{ph} \right] + B^{ph} \\ &= -\sum_i \left(\frac{1}{2} \sum_j \chi_{ij}^p \mu_j - A_i^p \right) \mu_i + B^p.\end{aligned}\tag{22}$$

Using Eq. (22) to expand Eq. (8) yields the thermodynamic grand-potential density of a multi-component system

$$\begin{aligned}\omega_{ch}(\phi, \mu) &= \omega_{ch}^\gamma(\mu) h(\phi) + \omega_{ch}^{\gamma'}(\mu) h(1 - \phi), \\ &= h(\phi) \left(-\sum_i \left(\frac{1}{2} \sum_j \chi_{ij}^\gamma \mu_j^2 - A_i^\gamma \mu_i \right) + B^\gamma \right) \\ &\quad + [1 - h(\phi)] \left(-\sum_i \left(\frac{1}{2} \sum_j \chi_{ij}^{\gamma'} \mu_j^2 - A_i^{\gamma'} \mu_i \right) + B^{\gamma'} \right).\end{aligned}\tag{23}$$

Since, the generalized susceptibility can be defined as the second derivative of the grand-potential with respect to the diffusion potential, the parameter χ_{ij} can be interpreted as a generalized susceptibility [58], which corresponds to the inverse of the thermodynamic factor matrix. More precisely, χ_{ij} are the components of the matrix $\hat{\chi}$ which is the inverse of the thermodynamic factor matrix \hat{X} . The indices i, j denote the species in the Ni-base superalloy excluding the base element Ni. More details on multi-component systems with two or more phases can be found in [45, 46].

Common tangent construction

When two connected phases are in chemical equilibrium with each other, the diffusion potentials need to be continuous at the common interface, i.e. $\mu_i^{\gamma,eq} = \mu_i^{\gamma',eq}$. The equilibrium values $c_i^{p,eq}$ and $f_{ch}^{p,eq}(c_i^{p,eq})$ are found by the common tangent construction. The illustration in Fig. 3 shows the parabolic free energies for a ternary system with two phases γ and γ' in equilibrium. Similar to the case of binary alloys, the equilibrium compositions $c_i^{p,eq}$ of the two phases can be found via the common tangent construction which also identifies the general minimum free energy. In the case of binary alloys, a tangent line connects the two phases, which identifies the phase equilibrium compositions. In ternary alloys, there is a common tangent plane that is connected to both free energy surfaces and this can be used to find a set of tie-lines and a corresponding set of equilibrium compositions. By projecting the connection of common tangent plane to both free energy surfaces onto the composition plane as shown in Fig. 3, the $\gamma + \gamma'$ phase field is defined for a particular temperature.

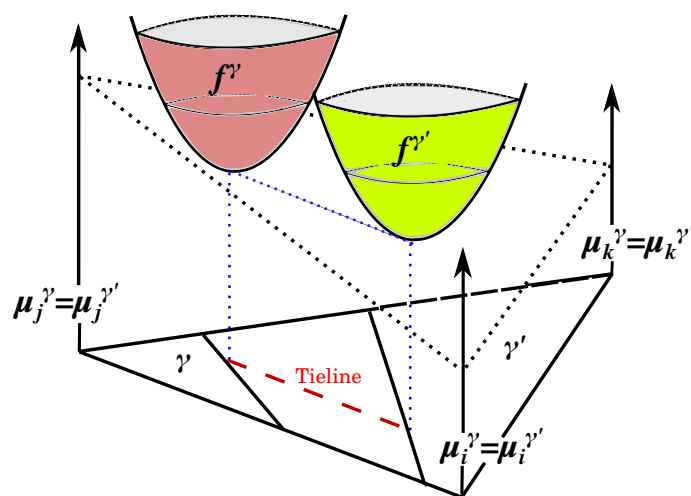


Figure 3: Illustration of the common tangent plane construction for a ternary alloy (based on [59]). A common tangent plane is connected to both free energy surfaces and this can be used to find a set of tie-lines and a corresponding set of equilibrium compositions.

The phase dependent constants A_i^p and B^p in Eqs. (19)-(23) are related to the equi-

librium compositions $c_i^{p,eq}$ and the equilibrium free energy densities $f_{ch}^{p,eq}(c_i^{p,eq})$, respectively. To determine the constant B^p , the parabolic free energy in Eq. (19) is used. This expression is inverted to yield,

$$B^p = f^{p,eq} - \sum_i \sum_j \left(\frac{1}{2} \frac{(\mu_i^{eq})^2}{X_{ij}^p} \right) \mu_j^{eq}. \quad (24)$$

To calculate the constant A_i^p , the first derivative of the parabolic free energies with respect to the compositions as in Eq. (20) is simply inverted to yield

$$A_i^p = c_i^{p,eq} + \frac{\mu_i^{eq}}{\sum_j X_{ij}^p}. \quad (25)$$

Once all the values have been calculated, one can simply fit all the obtained parameters into the free energies to get the grand potential densities.

2.2 Phase-field equation

The evolution of the phase field is assumed to evolve towards the minimization of the potential Ω

$$\frac{\partial \phi}{\partial t} = -\frac{K}{3\sigma\xi} \frac{\delta \Omega}{\delta \phi}, \quad (26)$$

where, the constant K is the kinetic coefficient which is related to the motion of the interface. The variation of the grand potential functional to the phase field is evaluated according to

$$\frac{\delta \Omega}{\delta \phi(\vec{x})} = \frac{\partial \omega}{\partial \phi} - \sum_{\psi} \partial_{\psi} \frac{\partial \omega}{\partial (\partial_{\psi} \phi)}, \quad (27)$$

where ψ is the spatial coordinate. At a constant temperature, the variation of the grand-potential functional in Eq. (1) with respect to ϕ and μ results in

$$\begin{aligned} \delta \Omega = & \int dV \left\{ -3\sigma\xi \nabla^2 \phi + \frac{6\sigma}{\xi} g'(\phi) \right. \\ & \left. + h'(\phi) \left(\frac{\partial \omega_{ch}(\mu)}{\partial h} \right) \right\} \delta \phi \\ & + \left\{ h(\phi) \frac{\partial \omega_{ch}^{\gamma}(\mu)}{\partial h} + [1 - h(\phi)] \frac{\partial \omega_{ch}^{\gamma}(\mu)}{\partial h} \right\} \delta \mu, \end{aligned} \quad (28)$$

with the requirement that $\partial_{\phi} h(\phi)|_{\phi=0,1} = 0$ such that the driving force vanishes outside of the interfacial region. From this expression, the variational derivative with respect to

the order parameter ϕ can be written as

$$\frac{\delta\Omega}{\delta\phi} = -3\sigma\xi\nabla^2\phi + \frac{6\sigma}{\xi}g'_{dw}(\phi) + h'(\phi)\left(\frac{\partial\omega_{ch}}{\partial h}\right). \quad (29)$$

Substituting the functional derivative (29) into (26) results in the explicit phase field equation

$$\begin{aligned} \frac{\partial\phi}{\partial t} &= -\frac{K}{3\sigma\xi}\frac{\delta\Omega}{\delta\phi} \\ &= -\frac{K}{3\sigma\xi}\left(-3\sigma\xi\nabla^2\phi + \frac{6\sigma}{\xi}g'_{dw}(\phi) + h'(\phi)\left(\frac{\partial\omega_{ch}}{\partial h}\right)\right) \\ &= K\left(\nabla^2\phi - \frac{2}{\xi^2}g'_{dw}(\phi) - \frac{1}{3\sigma\xi}h'(\phi)\left(\frac{\partial\omega_{ch}}{\partial h}\right)\right), \end{aligned} \quad (30)$$

where the thermodynamic driving force for phase transformation is given as the partial derivation of the grand-potential density with respect to the interpolation function

$$\begin{aligned} \frac{\partial\omega_{ch}}{\partial h} &= \omega_{ch}^\gamma(\mu) - \omega_{ch}^{\gamma'}(\mu) \\ &= \left(\sum_i\left(\frac{1}{2}\chi_{ij}^\gamma\mu_j^2 - A_i^\gamma\mu_i\right) + B^\gamma\right) - \sum_i\left(\frac{1}{2}\chi_{ij}^{\gamma'}\mu_j^2 - A_i^{\gamma'}\mu_i\right) + B^{\gamma'} \\ &= \sum_i\left(\frac{1}{2}\sum_j\Delta\chi_{ij}\mu_j - \Delta A_i\right)\mu_i + \Delta B, \end{aligned} \quad (31)$$

where $\Delta B = B^\gamma - B^{\gamma'}$, $\Delta A_i = A_i^\gamma - A_i^{\gamma'}$ and $\Delta\chi_{ij} = \chi_{ij}^\gamma - \chi_{ij}^{\gamma'}$. Long term microstructural evolution in Ni-base superalloys is characterized by the degradation of microstructures via the coarsening of precipitates which leads to the reduction of the interfacial energy. An efficient phase field model should correctly reproduce the experimental energies of the interfaces. When the size of the domain is much larger than the interfacial width, the microstructural evolution is barely controlled by the interfacial width. If one is not interested in the initial stages of microstructural evolution, then the reproduction of experimental interfacial energies in the model is not necessary. Furthermore, for diffusion-limited transformations, the interface width should be much larger than the grid size Δx . An optimal choice for the interface width should be around $\xi \approx 2.5\Delta x$. The mesh size Δx for phase-field simulations should be small enough to resolve interfaces. It is worth noting that the interface width ξ is a numerical parameter rather than a physical entity whose value is chosen purely for numerical reasons.

2.2.1 Numerical solution

Discretizing the time evolution of the phase-field equation (30) using the finite difference method we get

$$\phi^{n+1}(i, j) = \phi^n(i, j) + \frac{\Delta\phi^n(i, j)}{\Delta t} \Delta t, \quad (32)$$

where n is the time index and $\Delta\phi^n(i, j)$ is the change ϕ between n and $n+1$. Discretizing in space we get

$$\begin{aligned} \frac{1}{K} \frac{\Delta\phi^n(i, j)}{\Delta t} &= \frac{1}{(\Delta x)^2} (\phi^n(i+1, j) + \phi^n(i-1, j)) \\ &+ \frac{1}{(\Delta x)^2} (\phi^n(i, j+1) + \phi^n(i, j-1)) \\ &- \frac{1}{(\Delta x)^2} (4\phi^n(i, j)) - \frac{2}{\xi^2} g'_{dw}(\phi^n) \\ &- \frac{1}{3\sigma\xi} h'(\phi^n) \left(\sum_i \left(\frac{1}{2} \sum_j \Delta\chi_{ij} \mu_j - \Delta A_i \right) \mu_i + \Delta B \right), \end{aligned} \quad (33)$$

where i, j are spatial indices.

2.2.2 Stationary solution

The variation of the grand-potential functional Ω with the respect to ϕ gives the driving force for phase transition. At equilibrium the grand-potential densities of the two phases are equal, $\omega^\gamma(\mu) = \omega^{\gamma'}(\mu)$ which implies that the thermodynamic driving force $\partial\omega_{ch}/\partial h$ in Eq. (30) vanishes. Thus, the equilibrium solution for a planar interface is obtained by minimizing the variation of the grand potential Ω with respect to ϕ

$$\begin{aligned} \frac{\delta\Omega}{\delta\phi} &= \frac{\delta}{\delta\phi} \omega_{int}(\phi, \nabla\phi) = 0 \\ &\frac{\delta}{\delta\phi} \left(\frac{3\sigma\xi}{2} (\nabla\phi)^2 + \frac{6\sigma}{\xi} g_{dw}(\phi) \right) \\ &= -3\sigma\xi \frac{\partial^2\phi}{\partial x^2} + \frac{6\sigma}{\xi} g'(\phi) = 0. \end{aligned} \quad (34)$$

At equilibrium, the interfacial grand-potential density $\omega_{int}(\phi, \nabla\phi)$ only adds to the energy within the interface [58]. Therefore the contribution $\omega_{int}(\phi, \nabla\phi)$ can be assumed to be equal to the interface energy σ

$$\int_{-\infty}^{\infty} \left(\frac{3\sigma\xi}{2} \left(\frac{\partial\phi_0}{\partial x} \right)^2 + \frac{6\sigma}{\xi} g(\phi_0) \right) dx = \sigma. \quad (35)$$

From this, it can be seen that interfacial properties can be controlled without taking into account the bulk thermodynamics. A solution for a planar interface along the x

direction can be obtained by minimizing Ω with respect to ϕ

$$-3\sigma\xi\frac{\partial^2\phi}{\partial x^2} + \frac{6\sigma}{\xi}g'_{dw}(\phi) = 0. \quad (36)$$

The solution is independent of the grand-potential densities of the two bulk phases. There are four steady-state solutions of Eq. (36) for a planar interface along the x direction. Two solutions are of a single matrix $\phi = 0$ and single precipitate $\phi = 1$ everywhere in the domain. Another is solution of a continuous interface between the matrix and precipitate phases; however, this solution is unstable. There is also a non-trivial two-phase solution with an interface at position x_0

$$\phi_0(x) = \frac{1}{2} \left(1 + \tanh \frac{x - x_0}{\xi} \right) \quad (37)$$

where ξ is the interface thickness.

2.2.3 Dynamic solution

Now considering the case of a small but non-vanishing driving force, i.e., $\mu_0 = \text{const.}$ Such a scenario leads to a steady-state motion of the planar interface. To examine a planar steady state interface, Eq. (37) is switched to a coordinate frame moving at a constant velocity v . Therefore, $\partial\phi/\partial t$ changes to $-v(\partial\phi/\partial t)$. Since the phase field ϕ is considered to be a non-conserved order parameter, the dynamics of the phase field model are described through the Allen Cahn equation

$$\frac{\partial\phi}{\partial t} = K \left(\nabla^2\phi - \frac{2}{\xi^2}g'_{dw}(\phi) - \frac{\lambda}{3\sigma\xi}h'(\phi)\mu_0 \right). \quad (38)$$

The steady state motion of the planar interface can be solved analytically by the following expression

$$\phi(x, t) = \frac{1}{2} \left(1 + \tanh \frac{x - vt}{\xi} \right). \quad (39)$$

Evaluating further, the theoretical interface velocity is given by

$$v = \frac{K}{\sigma}\mu_0. \quad (40)$$

where K is the kinetic coefficient and σ is the isotropic interfacial energy.

2.3 Multi-component diffusion equations

To account for the transport of solutes in a multi-component alloy, a set of i diffusion equations is required. The derivation of the diffusion equations is started from the conservation condition

$$\frac{\partial \bar{c}_i(\phi)}{\partial t} + \vec{\nabla} \cdot \vec{j}_i = 0, \quad (41)$$

where $\bar{c}_i(\phi)$ is the local concentration and \vec{j}_i is the flux of solutes which is given by

$$\vec{j}_i = - \sum_j \left(M_{ij}^p \vec{\nabla} \mu_j \right), \quad (p = \gamma \text{ or } \gamma'), \quad (42)$$

where M_{ij}^p is the atomic mobility matrix. Further evaluation yields the equation of motion for a given species i

$$\frac{\partial \bar{c}_i(\phi)}{\partial t} - \sum_j \vec{\nabla} \left(M_{ij}^p \vec{\nabla} \mu_j \right) = 0. \quad (43)$$

The non-equilibrium concentration profile is related to the grand-potential functional Ω via the variational derivative with respect to μ

$$\begin{aligned} \bar{c}_i(\phi) &= -\frac{\delta \Omega}{\delta \mu_i} = -h(\phi) \frac{\partial \omega^\gamma}{\partial \mu_i} - (1-h(\phi)) \frac{\partial \omega^{\gamma'}}{\partial \mu_i} \\ &= -h(\phi) \frac{\partial}{\partial \mu_i} \left[-\sum_i \left(\frac{1}{2} \chi_{ij}^\gamma \mu_j^2 - A_i^\gamma \mu_i \right) + B^\gamma \right] \\ &\quad - (1-h(\phi)) \frac{\partial}{\partial \mu_i} \left[-\sum_i \left(\frac{1}{2} \chi_{ij}^{\gamma'} \mu_j^2 - A_i^{\gamma'} \mu_i \right) + B^{\gamma'} \right] \\ &= h(\phi) \left[\sum_i \left(\chi_{ij}^\gamma \mu_j + A_i^\gamma \right) \right] + (1-h(\phi)) \left[\sum_i \left(\chi_{ij}^{\gamma'} \mu_j + A_i^{\gamma'} \right) \right]. \end{aligned} \quad (44)$$

Note here that $c^p = \sum_i \left(\chi_{ij}^p \mu_j + A_i^p \right)$. Inserting Eq. (44) into (41) we obtain

$$\begin{aligned} \sum_j \vec{\nabla} \left(M_{jk}^p \vec{\nabla} \mu_k \right) &= \frac{\partial \bar{c}_i(\phi)}{\partial t} \\ \sum_j \vec{\nabla} \left(M_{jk}^p \vec{\nabla} \mu_j \right) &= \frac{\partial}{\partial t} \left\{ h(\phi) \left[\sum_i \left(\chi_{ij}^\gamma \mu_j + A_i^\gamma \right) \right] \right. \\ &\quad \left. + (1-h(\phi)) \left[\sum_i \left(\chi_{ij}^{\gamma'} \mu_j + A_i^{\gamma'} \right) \right] \right\}. \\ \sum_j \vec{\nabla} \left(M_{ij}^p \vec{\nabla} \mu_j \right) &= \sum_{jk} (\bar{\chi})_{ij} \frac{\partial \mu_i}{\partial t} + \Delta A_j \frac{\partial h}{\partial \phi} \frac{\partial \phi}{\partial t} \\ \sum_{jk} (\bar{\chi})_{ij}^{-1} \vec{\nabla} \left(M_{jk}^p \vec{\nabla} \mu_k \right) &= \frac{\partial \mu_i}{\partial t} + \sum_{jk} (\bar{\chi})_{ij}^{-1} \Delta A_j \frac{\partial h}{\partial \phi} \frac{\partial \phi}{\partial t}. \end{aligned} \quad (45)$$

Evaluating further, we obtain the equations for the evolution of the diffusion potential

fields

$$\begin{aligned} \frac{\partial \mu_i}{\partial t} &= \sum_{jk} (\bar{\chi})_{ij}^{-1} \vec{\nabla} \left(M_{jk}^p \vec{\nabla} \mu_k \right) \\ &\quad - \sum_j (\bar{\chi})_{ij}^{-1} \Delta A_j \frac{\partial h}{\partial \phi} \frac{\partial \phi}{\partial t}, \end{aligned} \quad (46)$$

where the concentration difference $\Delta A_i = A_i^\gamma - A_i^{\gamma'}$ is independent from the phase field. Here, we defined the interpolated susceptibility matrix $\bar{\chi}_{ij}(\phi)$ as $\bar{\chi}_{ij}(\phi) = h(\phi)\chi_{ij}^\gamma + h(1-\phi)\chi_{ij}^{\gamma'}$, with $\chi_{ij}^p = \partial c_i^p / \partial \mu_j$. At this stage, we point out that in general we have to take the inverse of the susceptibility matrix at each grid-point and each time step. This is obviously computationally expensive. To simplify Eq. (46), we adopt equal matrices for the two phases, that: $\chi_{ik}^\gamma = \chi_{ik}^{\gamma'}$ and $M_{ij}^\gamma = M_{ij}^{\gamma'}$. In the case of equal mobility and thermodynamic matrices for the two phases, the phase-field dependence drops and Eq. (46) simplifies to

$$\frac{\partial \mu_i}{\partial t} = \sum_j D_{ij} \left(\nabla^2 \mu_j \right) - \frac{\Delta A_i}{\chi_i} \frac{\partial h}{\partial \phi} \frac{\partial \phi}{\partial t}, \quad (47)$$

where the diffusion coefficient is defined as $D_{ij} = M_{ij} / \chi_i$. It should be noted here that $X_i = 1/\chi_i$.

2.3.1 Numerical solution

Discretizing the time evolution of the diffusion equation in Eq. (47) using the finite difference approach we get

$$\mu^{n+1}(i, j) = \mu^n(i, j) + \frac{\Delta \mu^n(i, j)}{\Delta t} \Delta t. \quad (48)$$

Discretizing in space as well we get

$$\begin{aligned} \frac{\Delta \mu^n(i, j)}{\Delta t} &= \sum_j \frac{D_{ij}}{(\Delta x)^2} (\mu^n(i+1, j) + \mu^n(i-1, j)) \\ &\quad + \sum_j \frac{D_{ij}}{(\Delta x)^2} (\mu^n(i, j+1) + \mu^n(i, j-1)) \\ &\quad - \sum_j \frac{D_{ij}}{(\Delta x)^2} (4\mu^n(i, j)) - h'(\phi^n) \frac{\Delta A_i}{\chi_i} \frac{\Delta \phi^n(i, j)}{\Delta t}, \end{aligned} \quad (49)$$

where i and j are spatial indices.

2.4 Model validation: Application to $\gamma \rightarrow \gamma'$ transformation

As a basic validation of our extended phase field model, predictions by the PFM⁸ are compared with one-dimensional ThermoCalc equilibrium calculations as well as DICTRA sharp interface simulations. The phase-field simulations are performed without the contributions from elasticity since the ThermoCalc and DICTRA models do not include elasticity. In PFM, a thin strip of γ -matrix of length $L_x = 1000\Delta x$ and width $L_y = 50\Delta x$ is used. A γ' -precipitate of size $50\Delta x \times 50\Delta x$ is embedded on the left side

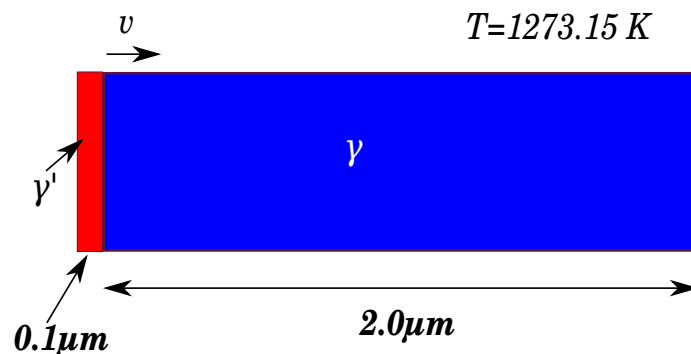


Figure 4: Schematic illustration of a DICTRA one-dimensional simulation set-up. Due to the lack of kinetics data for the γ' -precipitate, the concentration in phase is fixed to the equilibrium value pre-calculated in ThermoCalc.

of the γ -matrix. A uniform grid spacing $\Delta x = 8.6$ nm and interface width $\xi = 2\Delta x$ are chosen. Furthermore, for the phase-field set-up to resemble a one-dimensional system, appropriate boundary conditions are chosen. For the phase fields ϕ , Dirichlet boundary conditions are applied on all domain boundaries. For the diffusion potential field μ , Von Neumann boundary conditions are applied on the left boundary while Dirichlet boundary conditions are set for the rest of the boundaries. A time step of $\Delta t = 5 \times 10^{-3}$ s is used in the phase field simulations. The interfacial energy is assumed to be isotropic with a value of 80 mJ/m².

2.4.1 Validation of the interface kinetics

For the validation of interface kinetics, we restrict to the simple case of $\gamma \rightarrow \gamma'$ transformation in a binary Ni-Al alloy. A phase-field simulation of the diffusion-controlled growth of a γ' -precipitate in the Ni-20 wt.%Al alloy at 1273.15 K until equilibrium is performed. The Al content of the alloys is chosen in a manner that the simulations

⁸ Phase Field Method

at 1273.15 K fall within the two phase $\gamma - \gamma'$ region of the NiAl phase diagram. A DICTRA sharp-interface simulation is also done at the same length- and time-scale and the results are compared. In the DICTRA sharp-interface set-up, a thin region of the γ' -precipitate of thickness $0.2 \mu\text{m}$ is placed in the γ -matrix of size $2 \mu\text{m}$. The system is closed. At time $t > 0$ s, the γ' -precipitate is expected to grow into the γ -matrix. In both the DICTRA and PFM simulations, the initial composition of Al is set to 20 wt.% everywhere throughout the γ -matrix. The composition of Al in the γ' -precipitate is set to be the equilibrium composition 22.87 wt.%, a value calculated in advance from ThermoCalc. This is done because the DICTRA model does not account for diffusion in the γ' -precipitate.

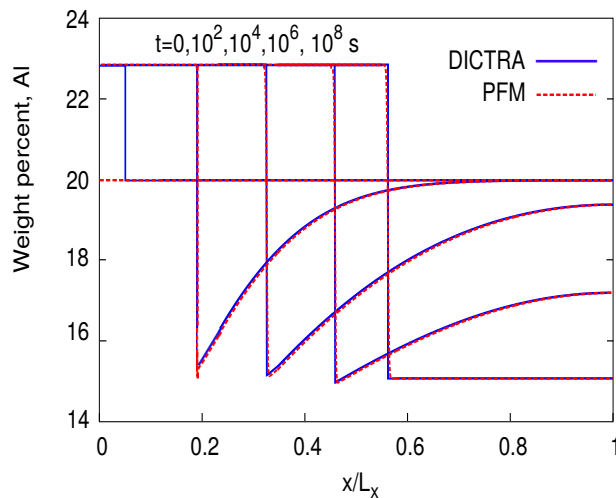


Figure 5: Time evolution of the Al concentration profiles during $\gamma \rightarrow \gamma'$ transformation in a binary Ni-20 wt.%Al alloy. The precipitate evolves until the equilibrium volume fraction of 56% is reached. In the initial stages, the γ' -precipitate grows at a much faster rate due to the presence of a relatively large amount of free Al solutes in the γ -matrix. As the Al solutes become depleted in the matrix the γ' -precipitate growth rate starts to decelerate until it eventually stops.

The plot in Fig 5 shows the time evolution of the Al concentration profiles. It can be seen that the precipitate evolves until the equilibrium volume fraction of 0.56 or 56% is reached. This equilibrium value is identical to the one predicted by ThermoCalc equilibrium calculations. In the initial stages, the precipitate grows at a much faster rate due to the presence of a relatively large amount of free Al solutes in the γ -matrix. As the Al solutes become depleted in the matrix, the precipitate growth rate starts to decelerate until it eventually stops. One can view the equilibrium regime as the state when the amount of Al solutes in the γ -matrix is so low that it can not sustain further growth of the precipitate.

The plot in Fig. 6 shows a plot of the comparison of the evolution of the γ' -precipitate volume fraction as a function of the real time. Provided that the PFM operates in a

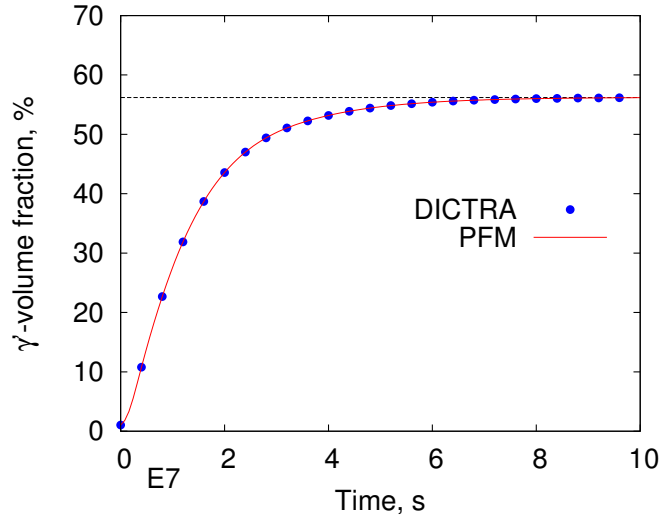


Figure 6: This figure shows the evolution of the γ' -volume fraction as a function of time during growth in Ni-20wt.%Al at 1273.15 K. The precipitate is allowed to grow for a time of 1×10^9 s. The phase-field results are represented by the solid red line while DICTRA results are denoted by the blue dots. The dashed black line represents the equilibrium γ' -volume fraction predicted by ThermoCalc.

sharp interface limit, where the interface width is negligibly small compared with the diffusion length as well as the total length L_x of the system, the resulting growth kinetics are in good agreement with the DICTRA simulations. If, however, the phase field width is chosen to be in the same order of magnitude as the diffusion length, then it is already known that the growth kinetics predicted from a diffuse interface model such as the PFM differ quite substantially from corresponding sharp interface results. This problem can be cured up to some extent by a thin interface analysis as proposed by Karma and coworkers [40] or as more recently discovered be introducing a kinetic cross coupling between the phase field and the diffusion field [5, 7]. Within our current formulation, we include none of these advanced techniques, because according to our observations this issue seems to be much less critical for coarsening than it is for growth.

2.4.2 Validation of equilibrium multi-component concentration profiles

Here, we validate our extended multi-component model via ThermoCalc calculations with respect to equilibrium phase concentrations. Quasi one-dimensional phase-field simulations of the $\gamma \rightarrow \gamma'$ phase transformation at 1273.15 K for CMSX4 and CMSX6 superalloys with compositions given in Table 1 are performed.

	Al	Co	Cr	Mo	Re	Ta	Ti	W	Ni
CMSX4	5.6	9.6	6.4	0.6	3.0	6.5	1.0	6.4	base
CMSX6	4.8	5.0	9.8	3.0	-	2.0	4.7	-	base

Table 1: The composition in wt.% of the superalloys under study.

The initial composition of each species is set to be uniform in both the γ' -precipitate and the γ -matrix. For both the phase and concentrations fields: Dirichlet boundary conditions are applied on all domain boundaries. The precipitate growth is limited by solute diffusion until the equilibrium volume fraction of about 56% is reached. Fig. 7 shows the PFM predictions of the time evolution of a) Ta and b) Cr concentration profiles in the CMSX4 superalloy.

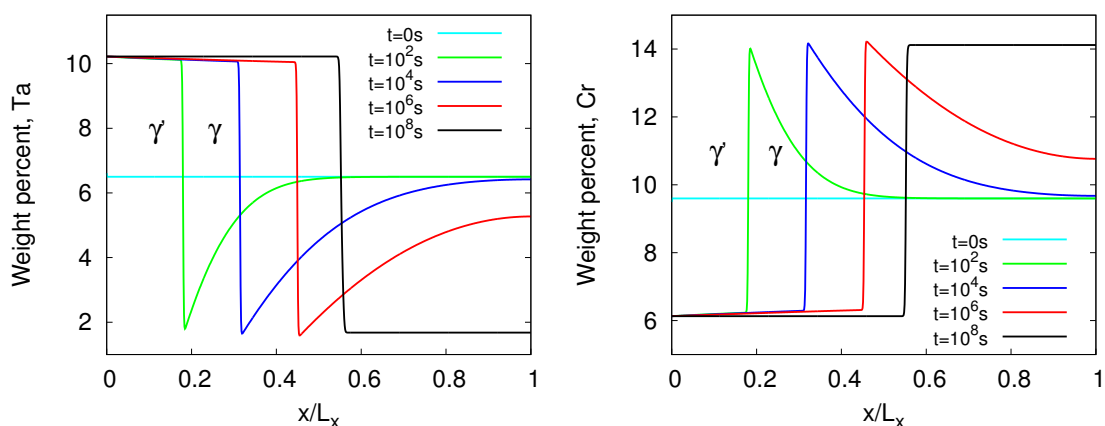


Figure 7: Evolution of Ta and Cr profiles during γ' -growth in CMSX4 at 1273.15 K.

As the precipitate grows, Ta diffuses from the γ -matrix into the γ' -precipitate which allows the precipitate to grow further in size. On the other hand, as the precipitate grows, Ta solutes become depleted in the matrix. The depletion of Ta solutes in the matrix leads to a reduction of the growth rate of the precipitate and eventual cessation of growth. Cr is rejected by the precipitate, which results in its pile-up in the γ -matrix. The counteracting mechanisms of absorption and rejection of solutes by the γ' -precipitate controls the motion of the interface. This is in contrary to the Ni-Al case where only the absorption of Al was responsible for the interface motion. We now compare the concentration profiles obtained from PFM at $t = 10^8$ s with corresponding ThermoCalc equilibrium calculations. Since ThermoCalc only calculates equilibrium values, we plot only the final concentrations of PFM to the equilibrium values from ThermoCalc. A comparison of equilibrium concentration profiles from PFM and bulk concentrations obtained from ThermoCalc for CMSX4 and CMSX6 are shown in Fig. 8 a) and b), respectively. The PFM predictions are in good agreement with the ThermoCalc results. In the phase-field profiles, the concentrations are measured from the precise location which is defined by the 0.56 location on the abscissa of the plot. The precise location of

the interface is identified as the position when $\phi = 0.5$, which corresponds to the middle of the hyperbolic tangent phase-field profile.

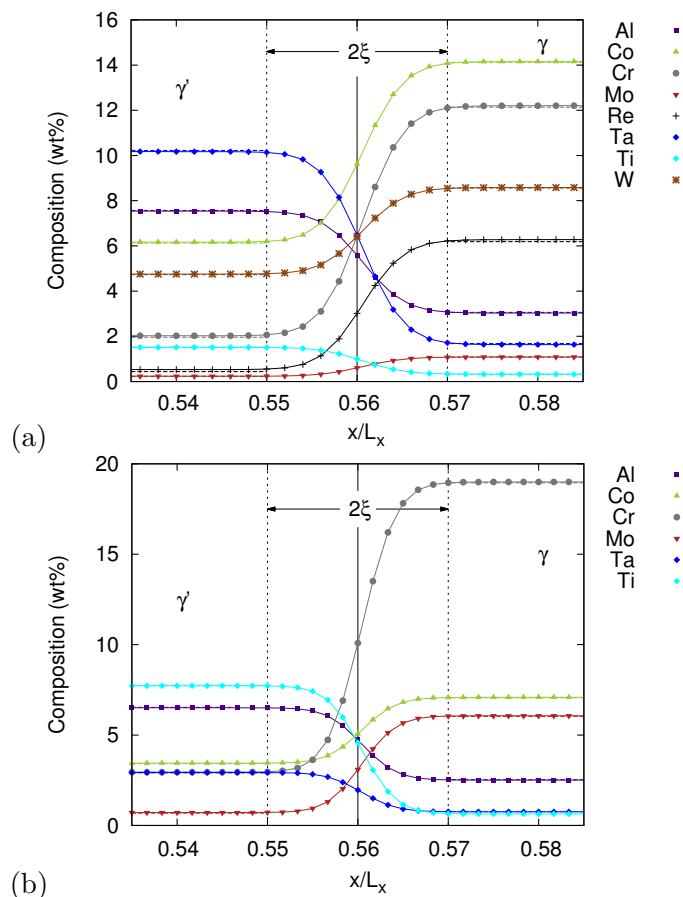


Figure 8: This figure shows the equilibrium phase concentrations obtained from phase-field simulations (linespoints) and ThermoCalc (dashed lines) in (a) CMSX4 and (b) CMSX6 after the $\gamma \rightarrow \gamma'$ transformation at 1273.15 K. These profiles correspond are the plots obtained at time, 1×10^9 s. The precise location of the interface is described by the 0.56 location on the abscissa of the plots.

The diffuse interface of width 2ξ in the concentration profiles from PFM emanates from the coupling of the thermodynamic properties of the bulk phases using the interpolation function $h(\phi)$. Fig. 8 also shows the general partitioning behavior of the solutes in Ni-base superalloys. The solutes Al, Ni and Ti-which are known to be γ' -formers, tend to partition more to the γ' -precipitate while Co, Cr, Mo, W and Re tend to partition more to the γ -matrix. In the following chapters, the influence of the partitioning behavior on the precipitate morphology and evolution kinetics shall be studied in detail.

2.5 Conclusion

A multi-component phase-field model based on the grand-potential formalism was presented. The model can be used to study morphological evolution in microstructures of arbitrary misfits, elastic inhomogeneities and external loads. As opposed to the well-known Kim-Kim-Suzuki model [42], the need to solve the equilibrium condition at each time step is eliminated. By virtue of the diffusion potential being the dynamic variable, the equilibrium condition is automatically satisfied in the multi-component model. This greatly reduces the computational costs when alloys with a multiple number of elements are simulated. The diffusion equations in the model use diffusion matrices to take into account the cross interactions between the solutes. The phase field model uses thermodynamic and kinetic input values obtained by CALPHAD tools. To circumvent the lack of kinetic data for the ordered γ' -phase in Ni-base superalloys, the multi-component model uses a symmetric model which assumes equal diffusion in both solid phases.

The thermodynamic consistency of the model was tested by comparing phase-field simulations to DICTRA and ThermoCalc simulations. DICTRA sharp interface calculations provide a simple approach for quantitative studies of diffusion-controlled phase transformations. The elemental partitioning behavior observed in phase-field simulations is consistent with observations from DICTRA and ThermoCalc. Furthermore, the predictions of interface kinetics by the phase field model were in agreement with one dimensional DICTRA simulations. The observed agreements of the two interface models demonstrate the ability of the phase field model to efficiently and accurately study the microstructure evolution in Ni-base superalloys. Rather than limiting to the Ni-Al alloy as it is done in most phase-field simulations, it makes a lot of sense to study real Ni-base superalloys as it will be done in the rest of this work.

As a possibility for further development, the multi-component phase field model can be further extended by coupling it through some interface to thermodynamic and kinetic databases to obtain the relevant driving forces. This could be of particular importance for non-isothermal transformations where thermodynamic and kinetic parameters have to be recalculated for each temperature.

The presented phase field model will be applied in the next chapters to solve realistic materials problems in multi-component alloys. For the simulation of solid-solid transformations, the multi-component phase field model will be coupled to elastic effects using linear elastic constitutive relations.

3 Modeling of structural transformations in Ni-base superalloys

Generally, phase field models for solid-solid transformations in Ni-base superalloys assume the interfacial energy to be isotropic. Thus in these models, the cuboidal shape of the γ' -precipitates is attributed to cubic elasticity [44, 48, 50, 85, 89]. Li et al. [48] argued that the anisotropy of the interfacial energy is relatively small at the high temperatures at which precipitate growth and coarsening in Ni-base superalloys occur. This argument justifies the assumption of isotropic interfacial energies in phase field models. Nonetheless, the true extent of the effects of the “small” anisotropy of the interfacial energy on precipitate morphology is yet unclear. Therefore, it would be inaccurate to neglect the contributions from the anisotropy of the interfacial energy on the precipitate morphology during solid-solid transformations in Ni-base superalloys. But including the anisotropy of the interfacial energy in phase field models with elastic effects requires the knowledge of the relative weighting of the contributions from interfacial energy and elastic anisotropies. This is surely tough to quantify due to the lack of experimental data of the anisotropy of the interfacial energies in Ni-base superalloys. The aim of this chapter is to show that the interfacial energy anisotropy and elastic anisotropy can both lead to the formation of precipitates with four-fold symmetry. To understand the effects, we first study precipitate morphologies in the presence of anisotropy of the interfacial energy only and then in the presence of isotropic interfacial energy and elastic anisotropy.

Methods of introducing a weak interfacial anisotropy into phase field models, without intending to describe the development of corners and facets, has been already known for quite a long time (see, for example, [11, 29, 40, 43, 52, 81]). In these formulations, the anisotropy comes into the phase field model, by allowing the gradient energy coefficient to depend on the interfacial orientation. For this kind of anisotropic phase field models, McFadden et al. [52] could show that the usual Gibbs-Thomson equation for the dependence of the diffusion potential on both the interfacial curvature and the orientation is recovered in the sharp interface limit. An undesired side effect of the formulation, using an orientation-dependent gradient energy coefficient, is the resulting kinetic anisotropy in such phase field models. For quantitative simulations, this kinetic anisotropy has to be counterbalanced by an appropriately chosen anisotropic kinetic coefficient [40]. Recently, other anisotropic phase-field formulations were proposed, where also the energy hump, that has to be overcome for the transformation, is chosen to depend on the orientation [51, 71]. These formulations neither lead to an intrinsic kinetic anisotropy nor involve an interface width that varies with orientation.

Mechanical effects are typically incorporated in phase-field models by coupling an elastic energy term to the free energy functional (see, for example, review by [80]). The models (e.g., [33, 37, 48]) use a Cahn-Hilliard type fourth order partial differential equation for the concentration, the order parameter in the Landau sense. The misfit-strain effects are incorporated by the application of the Vegard’s law to NiAl binary alloys, by assuming that the local equilibrium volume of the elementary cell depends linearly on the local concentration of Al. The resulting volume differences between the Al-rich and the Al-depleted regions are mapped to an eigenstrain which couples to the local

concentration field. However, the local concentration vector in the bulk in these models is constant which is not consistent with the solute depletion and enrichment zones observed in multi-component Ni-base superalloys e.g., in [35, 36, 61]. In order to circumvent this, one can introduce a dimensionless order parameter, which distinguishes between the phases similar to [23, 69]. Then thermodynamics couple to this field, resulting in a formulation, where an Allen-Cahn type second order equation couples to a set of second order multi-component diffusion equations. The local concentration vector in the Allen-Cahn type description is not constant within the bulk which is consistent with the solute depletion and enrichment zones observed in technical alloys.

The chapter is split into two subsections. In subsection 3.1 two different formulations of including the anisotropy of the interfacial energy are presented. The study focuses on the case of strong anisotropies leading to equilibrium shapes with sharp corners due to missing high-energy orientations. In subsection 3.2, two formulations of including anisotropic elasticity are presented. Microstructure evolution in Ni-base superalloys is then studied for two scenarios; first microstructure evolution is studied in the presence of the misfit and elastic inhomogeneity. Secondly, microstructure evolution is studied in the presence of the misfit and elastic inhomogeneity and applied load.

Parts of this chapter have been published in [Eur. Phys. J. Plus, 126:95, 2011.] and [Acta Mater., 93:60, 2015].

3.1 Equilibrium precipitate morphologies due to anisotropic interfacial energy

The crystalline nature of solids results in anisotropy of many thermophysical parameters. In particular, the interfacial energy between different phases is often found to be a function of the crystallographic orientation of the interface. Using the well-known Wulff theorem, the orientational dependency of the interfacial energy $\sigma(\theta)$ can be related to the equilibrium shape of a particle embedded in a matrix phase, and vice versa [10]. For sufficiently small anisotropies, the equilibrium shape is smooth. However, as the anisotropy increases the equilibrium particle morphology develops straight edges, known as facets, as well as corners, where certain interfacial orientations are excluded from the particle shape. However, developing phase-field models for strongly anisotropic interfacial energies, i.e. also accounting for sharp corners and facets, turns out to be challenging due to two principle difficulties [70]: First, sharp corners that arise due to missing orientations in the equilibrium shape are related to the non-convexity of the parametric inverse interfacial energy plot $1/\sigma(\theta)$. This eventually leads to ill-posed phase-field equations for these orientations, which have to be regularized. The second problem is that ideal straight facets require sharp cusp-like minima in the interfacial energy $\sigma(\theta)$. Then, the non-differentiability there results in undefined equilibrium and motion equations for interfaces having the orientation of a facet. To cure the problem of ill-posed phase-field equations for high-energy orientations Kobayashi et al. [43], as well as Eggleston et al. [16] suggest a regularization method, where the polar plot of the inverse of the interfacial energy is convexified. Recently, there were also a number of

attempts to regularize the phase-field by including higher-order terms [34, 71, 83, 84]. In this respect, also sharp interface equilibrium shapes have been studied [68]. The other challenging issue of anisotropic interfacial energies is faceting, due to non-differentiable cusps in the γ -plots. The easiest way to circumvent this problem is to use approximative rounded γ -functions, as throughly discussed in [15].

In section. 3.1 two different anisotropic phase-field formulations, using a simple two-phase model involving only one particle and one matrix phase. We focus on the case of strong anisotropies leading to equilibrium shapes with sharp corners due to missing high-energy orientations. To be able to recover accurately equilibrium shapes with corners due to missing orientations, we apply the regularization technique of Eggleston et al. [16]. This method is reformulated in terms of the phase field's unit normal-vector, being advantageous in two respects: first, a gain in the computational performance, and second, an increase in the numerical accuracy due to a more accurate measure of the phase field orientation even in the vicinity of the corners. Furthermore, we generalize the method to arbitrary crystal symmetries and discuss also rotations of the particle's crystalline orientation. We also discuss the numerical implementation of the presented two phase-field models. To achieve the necessary numerical accuracy and stability, we develop a new and efficient explicit finite difference algorithm, by combining the two-step differentiation of Debierre et al. [15] with a staggered grid formulation.

3.1.1 Phase-field model

First, a phase-field $\phi(\vec{x}, t)$, which discriminates between the two different phases is introduced. To distinguish between the phases, the fixed value 0 is assigned to the precipitate phase and 1 to the matrix phase. The total free energy of the a system is given as integral over the free energy density $f(\phi, \nabla\phi)$, which decomposes into interfacial, $f_{int}(\phi, \nabla\phi)$, and bulk contributions, $f_{bulk}(\phi)$

$$F[\phi(\vec{x}, t)] = \int_V \underbrace{(f_{int}(\phi, \nabla\phi) + f_{bulk}(\phi))}_{f(\phi, \nabla\phi)} dV \quad (50)$$

The interfacial contribution $f_{int}(\phi, \nabla\phi)$ depends on both the phase field ϕ and its gradient $\nabla\phi$. For the isotropic phase-field model, we can write the interfacial contribution as

$$f_{int}(\phi, \nabla\phi) = U \left(\frac{a^2}{2} (\nabla\phi)^2 + g(\phi) \right) \quad (51)$$

where, $g(\phi) = \phi^2(1 - \phi)^2$ is the double well potential, guaranteeing that the free energy density has two local minima at $\phi = 0$ and $\phi = 1$, that corresponds to the two distinct phases of the system. The phase field parameters U and a define, respectively, the interfacial energy scale and the characteristic length scale over which the phase field varies. The bulk contribution to the free energy density has to interpolate between the different bulk free energies f_p and f_m of the particle and the matrix phase, respectively.

We write

$$f_{bulk}(\phi) = h(\phi)f_m + (1 - h(\phi))f_p \quad (52)$$

where the interpolation function $h(\phi)$ has to be monotonic between $\phi = 0$ and $\phi = 1$, and has to satisfy the conditions $h(0) = 0$ and $h(1) = 1$. Furthermore, we demand $\partial_\phi h(\phi)|_{\phi=0,1} = 0$, since the minima of the total free energy density should remain at 0 and 1 also for sufficiently small but non-vanishing bulk free energy densities, $f_{m,p} \neq 0$.

The phase-field evolution shall obey a dissipative Allen-Cahn equation

$$\frac{\partial \phi}{\partial t} = -K \frac{\delta F}{\delta \phi} \quad (53)$$

where K is the kinetic coefficient, and $\delta F/\delta \phi$ denotes the functional derivative of the free energy functional with respect to the phase field order parameter. Generally, this derivative can be written as

$$\frac{\delta F}{\delta \phi} = \frac{\partial f}{\partial \phi} - \nabla \cdot \frac{\partial f}{\partial (\nabla \phi)} \quad (54)$$

where the last term denotes the divergence of the partial derivative of the free energy density with respect to the gradient of the phase field $\nabla \phi$. Before introducing anisotropy into the phase-field model, we discuss the steady state motion of the planar interface. In this case, the phase-field equation of motion Eq. (53) reduces to an effectively one dimensional equation, and we obtain in the isotropic case

$$\frac{\partial \phi}{\partial t} = KU \left(a^2 \frac{\partial^2 \phi}{\partial n^2} - g'(\phi) \right) - K(f_m - f_p)h'(\phi) \quad (55)$$

where the $'$ denotes the derivative with respect to ϕ , and $\partial/\partial n$ indicates the spatial derivative along the interface-normal direction \vec{n} .

We find an analytic steady state solution, that connects the particle and the matrix phase

$$\phi_0(\vec{x}, t) = \frac{1}{2} \left(1 + \tanh \left(2 \frac{\vec{x} \cdot \vec{n} - v_n t}{\xi} \right) \right) \quad (56)$$

where $\xi = 2\sqrt{2}a$ is the actual interface width, and $v_n = 3\sqrt{2}aK(f_m - f_p)$ denotes the steady state interface velocity. Then, using this solution of the planar front motion, we can calculate the total free energy of the heterogeneous two-phase system at bulk equilibrium, i.e. $f_m = f_p$, which relates to the interface energy density of the phase-field model

$$\sigma \equiv \int_{-\infty}^{\infty} U \left(\frac{a^2}{2} (\vec{n} \cdot \nabla \phi_0)^2 + g(\phi_0) \right) dn = \frac{\xi U}{12} \quad (57)$$

In Fig. 9, we show that in the quasi one dimensional case, i.e. planar interface with fixed orientation, the phase field simulations reproduce this functional behavior from

the steady state solution Eq. (56) very nicely, even in the presence of anisotropy, as will be discussed below. It is possible to write down the isotropic phase-field model in terms of the more easy to grasp parameters σ , denoting the interfacial energy density, and the actual interface width ξ instead of the two scales a and U . Then, we obtain the free energy functional, how may

$$F[\phi(\vec{x}, t)] = \int_V \left(\frac{3\sigma\xi}{4} (\nabla\phi)^2 + \frac{12\sigma}{\xi} g(\phi) + f_{bulk}(\phi) \right) dV. \quad (58)$$

3.1.2 Inclusion of anisotropic interfacial energy

Now we introduce the desired orientational anisotropy into the phase-field model as done in our work [24]. In this subsection, we aim to discuss two different anisotropic formulations: The **Varying Interface Width** formulation, denoted by **VIW**, and the **Varying Interfacial Energy** formulation, indicated by **VIE**. The first model corresponds to rather common anisotropic phase-field formulations, being frequently used in the literature. Here, the characteristic length scale a and thus also the interface width ξ is considered to vary with the interface orientation

$$a^{(\text{VIW})} \equiv a_0\alpha(\theta) \quad (59)$$

where $\alpha(\theta)$ denotes the anisotropy function. We call this model the Varying Interface Width formulation, denoted by VIW. The interface-orientation-angle θ is related to the gradient of the phase-field, $\tan\theta = \partial_y\phi/\partial_x\phi$, where ∂_x and ∂_y abbreviate the partial derivatives $\partial/\partial x$ and $\partial/\partial y$, respectively. In the present work, we restrict to a two dimensional description, where a single angle is sufficient to describe the orientation of the interface.

On the other hand, for the second and less common anisotropic phase-field model, the interfacial energy scale U is regarded to depend on the interface orientation

$$U^{(\text{VIE})} \equiv U_0\alpha(\theta) \quad (60)$$

We call this model the Varying Interfacial Energy formulation, abbreviated by VIE. The derivative of the anisotropy function $\alpha(\theta)$ with respect to the gradient of the phase-field $\nabla\phi$ is given by

$$\frac{\partial\alpha(\theta)}{\partial(\partial_x\phi)} = -\alpha'(\theta)\frac{\partial_y\phi}{(\nabla\phi)^2}, \quad (61)$$

$$\frac{\partial\alpha(\theta)}{\partial(\partial_y\phi)} = \alpha'(\theta)\frac{\partial_x\phi}{(\nabla\phi)^2}. \quad (62)$$

where, in this respect, the $'$ denotes the derivative with respect to the orientation. Inserting either Eq. (59) or Eq. (60) into Eq. (50) yields the anisotropic free energy functional,

from which the functional derivative has to be taken according to Eq. (54). Finally, inserting this expression into the Allen-Cahn Eq. (53), we obtain the phase-field kinetic equation

$$\frac{1}{K} \frac{\partial \phi}{\partial t} = \partial_x \left(\frac{\partial f_{int}}{\partial (\partial_x \phi)} \right) + \partial_y \left(\frac{\partial f_{int}}{\partial (\partial_y \phi)} \right) - U g'(\phi) + \mu_0 h'(\phi). \quad (63)$$

where we introduced the difference in the diffusion potentials between the particle and the matrix phase, $\mu_0 \equiv f_p - f_m$, and

$$\frac{\partial f_{int}^{(VIW)}}{\partial (\partial_x \phi)} = U \left(a^2(\theta) \partial_x \phi - a(\theta) a'(\theta) \partial_y \phi \right), \quad (64)$$

$$\frac{\partial f_{int}^{(VIW)}}{\partial (\partial_y \phi)} = U \left(a^2(\theta) \partial_y \phi + a(\theta) a'(\theta) \partial_x \phi \right). \quad (65)$$

Usually, the kinetic equation is found to be further evaluated, i.e. the partial derivatives are taken analytically (see for instance [16]). However, since we will calculate these derivatives numerically later on, similarly to [15, 40], we prefer to keep the above style of presentation. For the varying interface energy formulation, we can proceed in a similar way only using Eq. (60) instead of Eq. (59). Thus for the partial derivatives with respect to the gradient of the phase-field we obtain instead

$$\frac{\partial f_{int}^{(VIE)}}{\partial (\partial_x \phi)} = U(\theta) a^2 \partial_x \phi - U'(\theta) \frac{a^2}{2} \partial_y \phi - U'(\theta) g(\phi) \frac{\partial_y \phi}{(\nabla \phi)^2}, \quad (66)$$

$$\frac{\partial f_{int}^{(VIE)}}{\partial (\partial_x \phi)} = U(\theta) a^2 \partial_y \phi + U'(\theta) \frac{a^2}{2} \partial_x \phi + U'(\theta) g(\phi) \frac{\partial_x \phi}{(\nabla \phi)^2}. \quad (67)$$

The main difference between the two models is of course, that in the second model, the height of the double well hump is considered to depend on the interface orientation [51].

However, we would also like to point out another significant difference between the models: The anisotropy function $\alpha(\theta)$ enters as a square into the first VIW⁹ model, while this is not the case for the second VIE¹⁰ formulation. This is especially surprising, since taking the square of a periodic function can lead to a doubling of its period.

⁹Varying Interface Width formulation

¹⁰Varying Interfacial Energy formulation

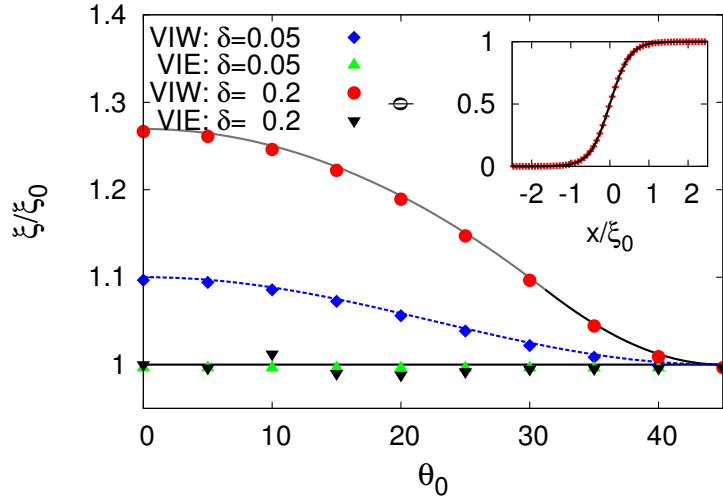


Figure 9: The figure summarizes the results of the one dimensional studies of the growth of the planar front due to a constant diffusion potential μ_0 using the two different anisotropic phase-field formulations. Here, VIW means the phase-field formulation with a varying interface width, while VIE denotes the phase-field formulation where the interfacial energy is chosen to be orientationally dependent. The interface width ξ/ξ_0 as a function of the crystalline orientation angle θ_0 of the rotated anisotropy function (90) is shown. The symbols denote the phase-field results, and the theoretical expectations from the analytic steady state solution Eq. (56) are indicated by the corresponding solid lines. For the case of $\delta = 0.2$ the convexification method explained in section. 3.1.5 is employed, as indicated by the gray line color.

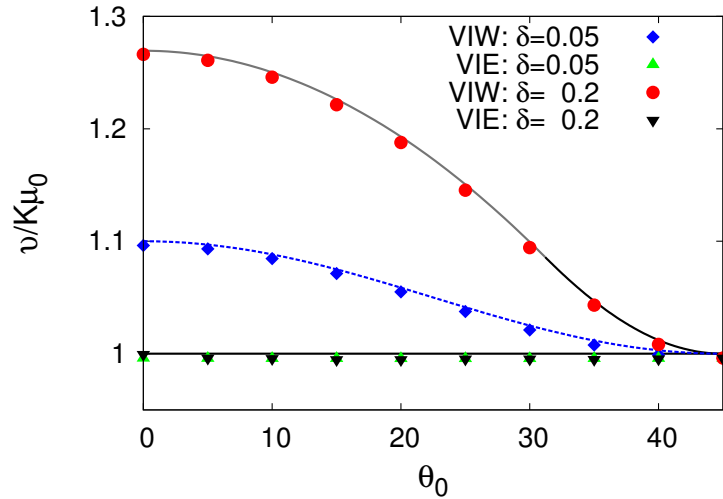


Figure 10: The figure summarizes the results of the one dimensional studies of the growth of the planar front due to a constant diffusion potential μ_0 using the two different anisotropic phase-field formulations. Here, VIW means the phase-field formulation with a varying interface width, while VIE denotes the phase-field formulation where the interfacial energy is chosen to be orientationally dependent. The dimensionless growth velocity $v/K\mu_0$ as a function of the crystalline orientation angle θ_0 of the rotated anisotropy function (90) is shown. For the case of $\delta = 0.2$ the convexification method explained in section. 3.1.5 is employed, as indicated by the gray line color.

Thus, in the present context of an anisotropy function representing the crystalline symmetry, a naive expectation is that using the same function $\alpha(\theta)$ the two models should sometimes lead to different crystalline symmetries. However, we never observed such an effect and therefore believe that the present formulations are correct.

3.1.3 Numerical implementation

To solve the phase-field Eq. (63) numerically, an explicit finite difference method with a uniform square mesh is developed. The mesh size is $h = 0.1\xi$ and the computational domain considered is the quadrant $h \leq x \leq Mh$ and $h \leq y \leq Nh$ where M and N are integers. The domain is surrounded by a one-grid-point boundary containing the boundary information. Then, $\phi_{i,k}$ shall denote the discretized phase-field at the point $(x = ih, y = kh)$. For the approximation of the time derivative, we use a standard explicit Euler scheme with a time step Δt .

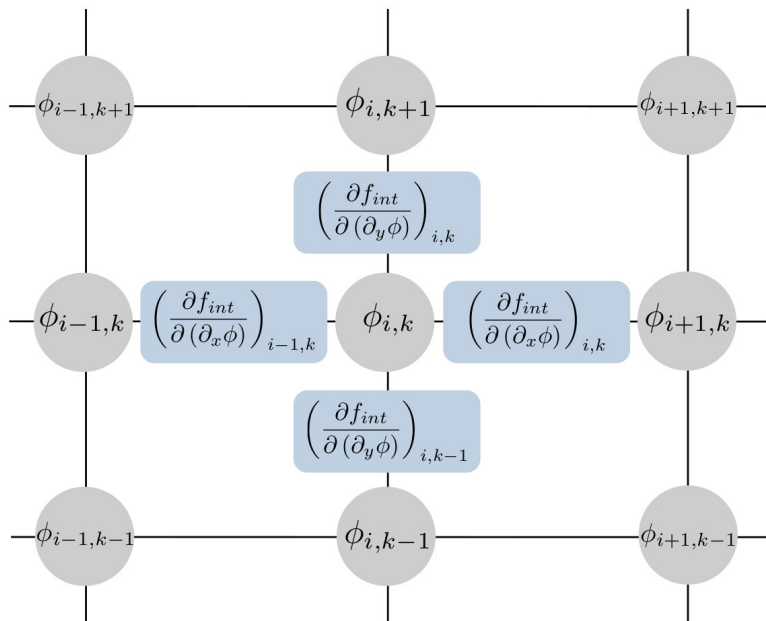


Figure 11: Illustration of the numerical implementation of the anisotropic phase-field model using a staggered grid [57, 67]. The phase-field is considered to “live” on the nodal points indicated by the circles. However, the derivatives of the interfacial free energy density with respect to either $\partial_x \phi$ or $\partial_y \phi$, i.e. Eqs. (64) and (64), “live” on at points shifted by $h/2$ in the x - or in the y -direction, respectively, as highlighted by the boxes.

However, more critical are the approximations to the spatial derivatives, and in order to achieve the desired accuracy, we develop a staggered grid formulation [57, 67]. This implies, that we proceed in two steps using alternately forward and backward first order finite difference schemes. For the sake of brevity, we demonstrate this procedure only for the VIW– formulation. The application to the VIE– formulation is straight forward.

In the bulk regime, where $|\nabla\phi| < 10^{-8}$, we set all contributions in the phase-field equation involving gradients to be zero. Conversely, when $|\nabla\phi| \neq 0$, we have to build an approximative expression for $\partial f_{int}^{(VIW)}/\partial(\partial_x\phi)$ “living” at points, on a grid, which is shifted along the x – axis by $h/2$ and $\partial f_{int}^{(VIW)}/\partial(\partial_y\phi)$ “living” at points shifted along the y – axis by $h/2$ (see Fig. 11). To construct the partial derivatives 64 and 65 of the interfacial free energy at these intermediate nodal points, we need expressions for the phase-field gradients in between the grid points. Therefore, we define

$$(\partial_x\phi)_{i+\frac{1}{2},k} = [\phi_{i+1,k} - \phi_{i,k}]/h, \quad (68)$$

$$(\partial_x\phi)_{i,k+\frac{1}{2}} = [\phi_{i+1,k+1} + \phi_{i+1,k} - \phi_{i-1,k} - \phi_{i-1,k+1}]/4h, \quad (69)$$

$$(\partial_y\phi)_{i+\frac{1}{2},k} = [\phi_{i+1,k+1} + \phi_{i,k+1} - \phi_{i,k-1} - \phi_{i+1,k-1}]/4h, \quad (70)$$

$$(\partial_y\phi)_{i,k+\frac{1}{2}} = [\phi_{i,k+1} - \phi_{i,k}]/h, \quad (71)$$

where Eqs. (69) and (70) correspond to appropriately averaged centered differencing approximations. Apart from the phase field gradients, it is also required to write down expressions for the anisotropy function $\alpha(\theta)$ and its first derivative $\alpha'(\theta)$. Since both these functions exhibit periodicity reflecting the crystalline anisotropy, it is possible to write them in terms of powers of $\sin\theta$ and $\cos\theta$. Then the latter terms are related to the unit normal vector, which can be efficiently approximated by

$$(\cos\theta)_{i+\frac{1}{2},k} = (n_x)_{i+\frac{1}{2},k} = (\partial_x\phi/|\nabla\phi|)_{i+\frac{1}{2},k}, \quad (72)$$

$$(\sin\theta)_{i+\frac{1}{2},k} = (n_y)_{i+\frac{1}{2},k} = (\partial_y\phi/|\nabla\phi|)_{i+\frac{1}{2},k}, \quad (73)$$

and corresponding expressions at the sites in between grid points in the y –direction. Using de Moivre’s formula, the above mentioned anisotropy function (81) and its derivative (82) can be expressed analytically in terms of powers of sinusoidal functions [9],

$$\alpha_{\nu,\delta}(\theta) = 1 + \delta \left(1 + \sum_{k=0}^{[\nu/2]} (-1)^k \binom{\nu}{2k+1} n_x^{\nu-(2k-1)} n_y^{2k+1} \right), \quad (74)$$

$$\alpha'_{\nu,\delta}(\theta) = -\nu\delta \left(\sum_{k=0}^{[\nu/2]} (-1)^k \binom{\nu}{2k} n_x^{\nu-2k} n_y^{2k} \right). \quad (75)$$

where $\binom{\nu}{k}$ denotes the binomial coefficient, and we directly write n_x and n_y instead of

$\cos \theta$ and $\sin \theta$. Now, using Eqs. (68)–(75) we compute the derivatives $\partial f_{int}^{(VIW)}/\partial(\partial_x \phi)$ at $(i + 1/2, k)$ and $\partial f_{int}^{(VIW)}/\partial(\partial_y \phi)$ at $(i, k + 1/2)$ for each point in the computational domain, and the results are stored in intermediate arrays, according to the staggered grid shown in Fig. 11. We apply no-flux boundary conditions for the two fields storing the intermediate information about the partial derivatives.

In the second step, we approximate the missing spacial derivatives on the right hand side Eq. (63) by a backward finite difference formula. Therefore the discretized phase-field equation finally reads

$$\begin{aligned} \frac{1}{K} \frac{\phi_{i,k}^{m+1} - \phi_{i,k}^m}{\Delta t} &= \frac{1}{h} \left[\left(\frac{\partial f_{int}}{\partial(\partial_x \phi)} \right)_{i,k}^m - \left(\frac{\partial f_{int}}{\partial(\partial_x \phi)} \right)_{i-1,k}^m \right. \\ &\quad \left. + \left(\frac{\partial f_{int}}{\partial(\partial_y \phi)} \right)_{i,k}^m - \left(\frac{\partial f_{int}}{\partial(\partial_y \phi)} \right)_{i,k-1}^m \right] \\ &\quad - U g'(\phi_{i,k}^m) + \mu_0 h'(\phi_{i,k}^m), \end{aligned} \quad (76)$$

where m denotes the time index.

3.1.4 Volume preservation

To obtain equilibrium shapes, the proposed Allen-Cahn equation is not very well suited, since it involves non-conserved order parameter dynamics leading either to growth or shrinking of the particle. From a theoretical point of view, it is better to use the Cahn-Hilliard equation, as done e.g., in [16, 71], which additionally involves the continuity condition for the order parameter ϕ . On the other hand, using the Cahn-Hilliard equation leads to a fourth order differential equation, which dramatically influences the performance of the simulation. Therefore, for the present work we will stick to the Allen-Cahn dynamics, and circumvent the problem of a growing or shrinking particle by considering the diffusion potential difference μ_0 to be time dependent such that a volume change of the particles is prohibited. The physical idea behind this technique, is that we control the diffusion potential via, e.g. the external temperature, such that the particle is held always critical, meaning that it neither grows nor shrinks [40]. Thus, the time dependence has to be chosen such that the volume of the particles is conserved

$$0 = \frac{d}{dt} V(t) = \int_V \frac{\partial}{\partial t} (1 - \phi(\vec{x}, t)) dV \quad (77)$$

Now, depending on the considered formulation we use the respective phase-field equation, that is, either Eq. (63) for the VIW–model or Eq. (67) for the VIE–model, and obtain the time dependence of the diffusion potential difference

$$\mu_0(t) = \frac{R(t)}{H(t)} \quad (78)$$

where we introduce the following abbreviations:

$$R(t) = K \int_V \left(\partial_x \left(\frac{\partial f_{int}}{\partial (\partial_x \phi)} \right) + \partial_y \left(\frac{\partial f_{int}}{\partial (\partial_y \phi)} \right) - \frac{\partial f_{int}}{\partial \phi} \right) dV, \quad (79)$$

and

$$H(t) = \int_V h'(\phi) dV \quad (80)$$

As shown in [56], this method is also suited for the multi-phase application. In Fig 12 we compare the equilibrium shapes produced by the two different models and the theoretical prediction from the Wulff construction, as will be discussed in next section. In this figure one can clearly see, that if the $\phi = 1/2$ -contour is considered to indicate the interface shape both models reproduce the theoretic Wulff construction nicely.

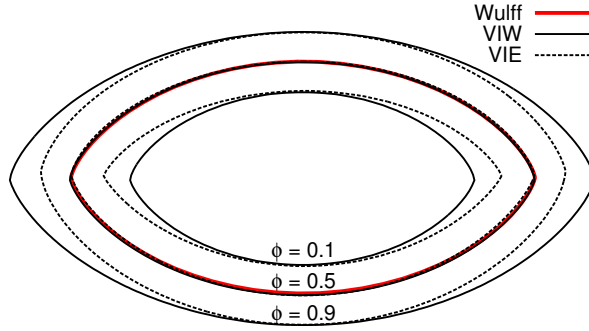


Figure 12: Equilibrium shapes obtained from the varying interface width formulation (VIW solid lines) and the varying interfacial energy formulation (VIE dashed lines). In either cases, the anisotropy function Eq. (81) with a two fold symmetry and an anisotropy strength of $\delta = 0.5$ has been used. The phase field is indicated by three different contours at $\phi = 0.1, 0.5, 0.9$. The red lines depict the corresponding parametric Wulff construction (85)–(86).

Also, in contrast to the results presented in [51], we do not observe a deviation of the VIW model from the Wulff construction. Rather, from a point of view of reproducing the correct equilibrium shapes, we can not give any clear preference towards one of the two different phase-field formulations.

3.1.5 Equilibrium shape of a particle in a matrix

Due to the underlying crystalline lattice the free energy of the interface between the

particle and matrix should depend on its orientation with respect to the basic lattice vectors. Therefore, we consider the interfacial energy to be anisotropic, $\gamma(\theta) = \gamma_0\alpha(\theta)$, where the anisotropy function $\alpha(\theta)$ reflects the functional dependence of the orientation with respect to some fixed crystalline axis.

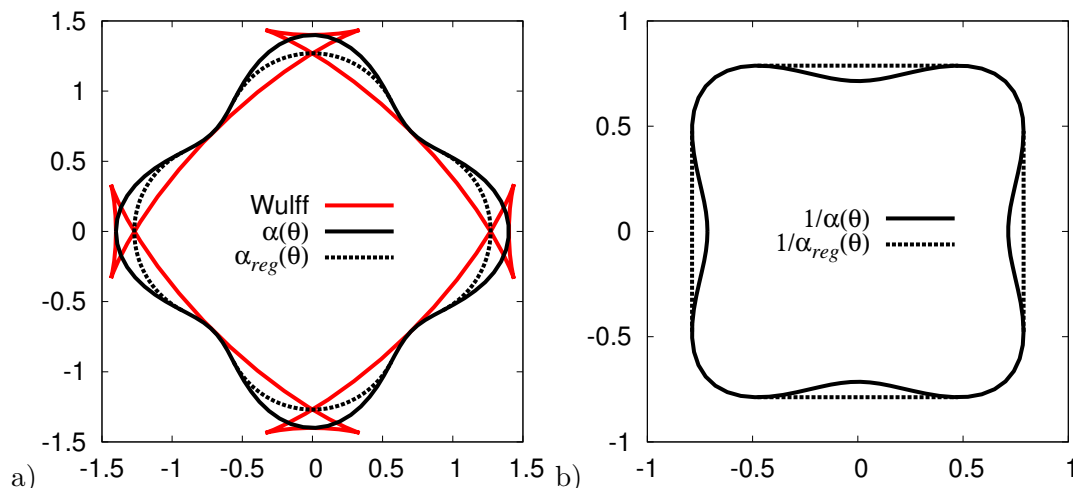


Figure 13: a): Parametric plot of the anisotropy function $\alpha(\theta)$, Eq. (84) (solid black line) and the related Wulff construction Eqs. (85)–(86) (solid red line). The equilibrium shape of the particle corresponds to the Wulff construction without the “ears”. The dotted line indicates the regularization of the anisotropy function $\alpha_{reg}(\theta)$, which leads to the same Wulff construction, but without the “ears”. b): To illustrate the convexification method, the parametric inverse anisotropy function, $1/\alpha(\theta)$, as well as the inverse regularization function $1/\alpha_{reg}(\theta)$ has been plotted.

So far we did not specify any anisotropy function $\alpha(\theta)$, which should exhibit a periodicity reflecting the crystalline symmetry. For the present work, we focus on the following anisotropy function:

$$\alpha(\theta) = 1 + \delta(1 + \cos(\nu\theta)), \quad (81)$$

$$\alpha'(\theta) = -\nu\delta \sin(\nu\theta), \quad (82)$$

$$\alpha''(\theta) = -\nu^2\delta \cos(\nu\theta), \quad (83)$$

where δ denotes the anisotropy strength, ν is an integer and defines the symmetry of the resulting equilibrium shape and $\alpha'(\theta), \alpha''(\theta)$ is the first and second derivative of the anisotropy function with respect to the interface orientation angle. Note, that the function is written such that it fixes the minimal interfacial energy, which in principle allows us to choose the anisotropy strength to be larger than 1. For the case of a four-fold symmetry and anisotropy strength $\delta = 0.2$, the function is plotted in parametric form in Fig. 13 as

$$x = \alpha(\theta) \cos(\theta), \quad y = \alpha(\theta) \sin(\theta). \quad (84)$$

Wulff's theorem demands that the equilibrium shape of the particle is surrounded by the multitude of tangents to the α -plot [10]. Thus we can calculate the equilibrium shape of a precipitate in parametric form as

$$x = \alpha(\theta) \cos(\theta) - \alpha'(\theta) \sin(\theta), \quad (85)$$

$$y = \alpha(\theta) \sin(\theta) + \alpha'(\theta) \cos(\theta). \quad (86)$$

This is the so-called ‘‘Wulff construction’’, which is shown in red (light solid line in black and white) in Fig. 13a. For sufficiently large δ , the particle equilibrium shape develops sharp corners, where certain high energy orientations are missing. The latter is accompanied by the appearance of the ‘‘ears’’, i.e. metastable and unstable branches, in the Wulff construction, as can be also seen in the figure. From a computational point of view, the occurrence of ‘‘ears’’ leads to an ill-posed phase-field evolution equation, which needs to be regularized [16, 70].

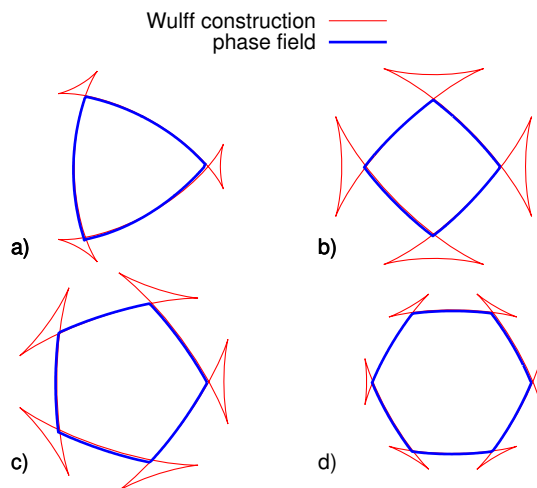


Figure 14: In this figure we compare the parametric Wulff construction (85)-(86) and the phase field contours at $\phi = 1/2$ after long simulation times: a) three fold symmetry, $\delta = 0.4$; b) four fold symmetry, $\delta = 0.2$; c) five fold symmetry, $\delta = 0.2$; d) six fold symmetry, $\delta = 0.1$. In all the cases the VIE-formulation (60) in combination with the anisotropy function (81) has been used.

To resolve this problem, we refer to the convexification method suggested by Eggleston et al. [16], as will also be reviewed briefly in the following. Missing orientations in the equilibrium shape occur when the reciprocal α -plot first becomes concave, which is the case when $\alpha + \alpha'' = 0$. Therefore, $\alpha + \alpha'' = 1 + \delta - (\nu^2 - 1)\delta \cos(\nu\theta) = 0$, meaning that $\delta > 1/(\nu^2 - 2)$. If now the anisotropy strength exceeds this threshold, we obtain the first missing orientations by the condition

$$0 = \frac{d}{d\theta} \left(\frac{\cos \theta}{\alpha(\theta)} \right) = \alpha(\theta_m) \sin \theta_m + \alpha'(\theta_m) \cos \theta_m \quad (87)$$

To find the first missing orientation θ_m , we suggest a standard Newton iteration (see e.g. [28]) as given by ,

$$\theta_m^{(n+1)} = \theta_m^{(n)} - \frac{\alpha(\theta_m) \sin \theta_m + \alpha'(\theta_m) \cos \theta_m}{(\alpha(\theta_m) + \alpha''(\theta_m)) \cos \theta_m} \quad (88)$$

where n indicates the iteration step. Now, using this angle θ_m and by proper rotation we can, identify all the regimes of orientations, where the reciprocal α -plot of Eq. (81) is concave. Therefore, in order to regularize the phase-field equation, we replace the anisotropy function $\alpha(\theta)$ by a new function $\tilde{\alpha}(\theta)$ such that it still produces the same equilibrium shape, but having a fully convex reciprocal $\tilde{\alpha}$ -plot. As also suggested in [16], we replace the anisotropy function in these regimes by appropriately chosen circular sections, i.e. straight lines in the reciprocal parametric plot, as illustrated in Fig. 13 for the case of four-fold crystalline symmetry.

However, since the direct numerical measure of the interface orientation angle, such as $\theta = \arctan \partial_y \phi / \partial_x \phi$, turned out to be erroneous, we use the components of the normal vector $n_x \equiv \cos \theta = \partial_x \phi / |\nabla \phi|$ and $n_y \equiv \sin \theta = \partial_y \phi / |\nabla \phi|$ instead, to rule out the discrepancy. In this respect, we write the regularized interfacial energy function as

$$\tilde{\alpha}(\theta) = \begin{cases} \alpha_{reg}(0) & \text{if } \hat{n}_x(0) > \cos(\theta_m) \\ \alpha_{reg}(1) & \text{if } \hat{n}_x(1) > \cos(\theta_m) \\ \vdots & \vdots \\ \alpha_{reg}(\nu - 1) & \text{if } \hat{n}_x(\nu - 1) > \cos(\theta_m) \\ \alpha(\theta) & \text{else} \end{cases} \quad (89)$$

where the regularization is given by $\alpha_{reg}(k) = \frac{\alpha(\theta_m)}{\cos(\theta_m)} \hat{n}_x(k)$, with the appropriately rotated normal interface vector $\hat{n}_x(k) = n_x \cos(\frac{2\pi}{\nu} k) + n_y \sin(\frac{2\pi}{\nu} k)$ (see also Eq. (91)). Finally, demonstrating that this method leads to the correct equilibrium shapes, we compared in Fig. 14 resulting phase field contours using the VIE model with their corresponding parametric Wulff constructions for a number of different crystalline symmetries.

The cases when the basic crystal lattice vectors do not correspond to the cartesian axis is also addressed. In this case the anisotropy function is shifted by the orientation angle θ_0 ,

$$\alpha(\theta) \equiv \alpha(\theta - \theta_0) \quad (90)$$

Then we construct the anisotropy function (74) and its derivative (75) using a normal

vector \vec{n}' which is rotated by the orientation angle θ_0 ,

$$\vec{n}' = \vec{R}(\theta_0)\vec{n} = \frac{1}{|\nabla\phi|} \begin{pmatrix} \cos \theta_0 & -\sin \theta_0 \\ \sin \theta_0 & \cos \theta_0 \end{pmatrix} \begin{pmatrix} n_x \\ n_y \end{pmatrix}, \quad (91)$$

where $\vec{R}(\theta_0)$ is the rotation matrix. Notice, that the rotated normal vector \vec{n}' should be used only for the construction of the anisotropy function and its derivative. All other expressions in Eqs. (64)–(65) need to be constructed out of the original normal vector \vec{n} . The reason why we operate here on the level of the normal interface vector instead of directly using a shifted angle $\theta - \theta_0$ is again related to the fact that the numerical measure of the normal vector turns out to be more accurate.

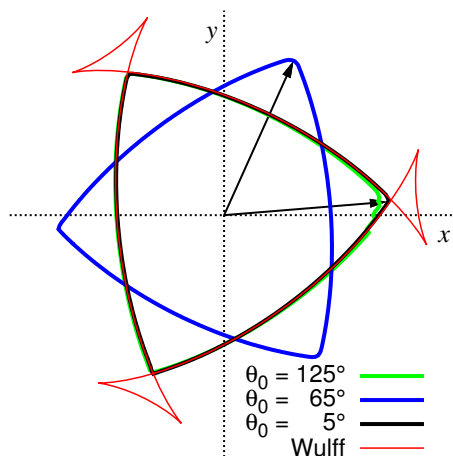


Figure 15: The rotated Wulff construction is compared with phase field contours, that were obtained after long simulation times using the anisotropy function (81) with $\delta = 0.4$ and a three fold symmetry being rotated, according to (90), by different orientation angles θ_0 . For the phase-field simulations, the VIW–formulation (59) has been used.

To demonstrate the accuracy of the rotations performed in our code, in Fig. 15, we plot the phase field contours of an anisotropic particle, where the anisotropy function is shifted by three different orientation angles $\theta_0 = 5^\circ, 65^\circ, 125^\circ$. The contours of $\theta_0 = 5^\circ$ and $\theta_0 = 125^\circ$ lie quite nicely upon each other, as well as on the rotated Wulff construction. Only the corner of the $\theta_0 = 125^\circ$ contour pointing to the right reveals some limitations of the accuracy. Note, that this corner corresponds to dynamics that are subjected to rotations beyond 2π , since for the selection of the corners in the convexification method, a similar rotation was used.

3.2 Modeling of strain-induced effects

The second phase γ' -precipitates in Ni-base superalloys are generated through solid to solid transformations from the parent γ -phase. While the continuous γ -matrix has a disordered *fcc* crystal structure, the precipitates are of the ordered *fcc(L1₂)* crystal structure. Due to the different partitioning behavior of solutes, the compositions of the two solid phases are often different. The difference in the composition and structural arrangements of the two phases is accompanied with a difference in the lattice parameters [60, 61, 73]. To maintain lattice continuity across the boundary local elastic deformations are required which generates coherency strain energy. The resulting coherency strain energy plays a critical role in determining the transformation path and microstructure evolution during solid-state transformations.

Phase-field methods have been used extensively to study microstructural evolution in elastically stressed solids. These models have been used to study non-directional coarsening [38, 76] and rafting in binary NiAl alloys [6, 33, 88, 89, 90]. Some models were formulated on a purely elasticity framework [33, 37, 48], some have been coupled with dislocation dynamics [88, 89, 90] while [30] has developed an elasto-viscoplastic model. Zhou et al. [89] identified that microstructures obtained using “elastic” models are qualitatively similar to those obtained by the “elastic-plastic” although the kinetics differ. In this work, misfit strain effects are incorporated by adding an elastic energy term to the validated model in chapter 2. We use the approach of [69] to model the dependence of the the total strain on the phase field which assumes equal elastic stresses in the two bulk phases at the diffuse interface. We assume the interfaces to be coherent, although this might not necessarily hold due to large deformations resulting from the larger misfit of the two phases. Dislocation motion can be incorporated in the phase field model but is expensive. It is more expensive than the incorporation of elastic heterogeneity as done in this work, which has been shown [33, 89] to be a good first approximation to the influence of the micro-mechanics on the coarsening kinetics in Ni-base superalloys. The influence of plasticity on phase transformations has been studied extensively numerically by Zhou et al. [88, 89, 90, 91] and Gaubert et al. [31]. Thus, this thesis focuses on the contributions of interdiffusion to solid-state transformations.

Neglecting the anti-phase domains, a single non-conserved field variable $\phi(\vec{x}, t)$ is introduced to describe the coherent γ/γ' two phase microstructure. To distinguish between the two distinct bulk phases, fixed values of the phase field variable ϕ are assigned to represent them, 1 for the γ -phase and 0 for the γ' -phase. Additionally, it is postulated that $\phi(\mathbf{x}, t)$ varies smoothly within an interface of a finite width. We neglect the appearance of anti-phase boundaries, which form between different translational variants of the ordered γ' -phase. The emphasis of the current model is to find a quantitative description of the coarsening kinetics of the γ' -phase. The current description is solely based on the assumption that the coarsening kinetics is limited by the complex interdiffusion kinetics of multiple components in the γ -phase. Strictly speaking, we develop a model for coarsening kinetics with low γ' -fraction. It is possible to include the influence from anti-phase boundaries by an extension of the description of the ordered γ' -phase

via multiple order parameters as has been demonstrated before [30, 79, 90]. However, a quantitative kinetic description of the γ' -coarsening behavior including the effect of anti-phase boundary migration requires reliable values for the anti-phase mobilities. They are certainly difficult to measure directly in the experiment. We define the grand-potential functional as the integral over the grand-potential density $\omega(\phi, \nabla\phi)$, which decomposes into interfacial, and thermodynamic and elastic contributions,

$$\Omega[\phi(\vec{x}, t)] = \int_V (\omega_{int} + \omega_{ch} + \omega_{el}) dV. \quad (92)$$

The interfacial contribution ω_{int} depends on both the phase field ϕ and its gradient $\nabla\phi$. The interfacial energy σ for this case is assumed to be isotropic, thus the interfacial contribution is explicitly written as

$$\omega_{int}(\phi, \nabla\phi) = \frac{3\sigma\xi}{2}(\nabla\phi)^2 + \frac{6\sigma}{\xi}g_{dw}(\phi), \quad (93)$$

where, $g(\phi) = \phi^2(1-\phi)^2$ is the double well potential, guaranteeing that the free energy density has two local minima at $\phi = 0$ and $\phi = 1$, that corresponds to the two distinct phases of the system and ξ is the interface width. The thermodynamic contribution ω_{ch} is postulated as a mixture of the bulk grand-potential densities

$$\omega_{ch}(\phi, \mu) = \omega_{ch}^\gamma(\mu)h(\phi) + \omega_{ch}^{\gamma'}(\mu)h(1-\phi), \quad (94)$$

where the interpolation function $h(\phi)$ has to be monotonic between $\phi = 0$ and $\phi = 1$, and has to satisfy the conditions $h(0) = 0$ and $h(1) = 1$. Furthermore, we demand $\partial_\phi h(\phi)|_{\phi=0,1} = 0$, since the minima of the total grand-potential energy density should remain at 0 and 1 also for sufficiently small but non-vanishing bulk grand-potential energy densities. The grand-potential density of the phase p can be obtained by a Legendre transform of the free energies

$$\omega^p(\mu) = f_{ch}^p(c, T) - \mu c^p, \quad (p = \gamma \text{ or } \gamma'), \quad (95)$$

where $f_{ch}^p(c, T)$ is the parabolic free energy of phase p

$$f_{ch}^p(c^p, T) = \sum_i \left(\frac{1}{2} \sum_j \chi_{ij}^p (c_i - A_i^p)^2 \right) + B^p, \quad (96)$$

where, i and j are the species in a multi-component system. The parameter χ_{ij}^p is related to the equilibrium thermodynamic factor matrix of phase p and the constants A_i^p and B^p are related to the equilibrium compositions and Gibbs energies of phase p , respectively.

3.2.1 Inclusion of mechanical effects

Mechanical effects are included in the model via the elastic energy term ω_{el} in Eq. (92). To write the expression of the elastic energy, we first define a displacement field \mathbf{u} . Elastic deformation is described via a vector field \mathbf{u} , which provides the displacement vector for a given point of the body with respect to its reference configuration. A material point x of the undeformed body will be found at $x + u(x)$ in the deformed material. Using linear elasticity theory, the strain tensor is introduced as the symmetric spatial derivative of the displacement field. The strain tensor is calculated from the displacement u_i by the kinematic equation

$$\varepsilon_{ij} = \frac{1}{2} \left(\frac{\partial u_i}{\partial x_j} + \frac{\partial u_j}{\partial x_i} \right), \quad (97)$$

where i, j denote the spatial coordinates. To complete the definition of the elastic energy density, the stress-free strain (eigenstrain) tensor $\varepsilon_{ik}^0(r)$ is required. Its physical definition is the value of which the strain tensor at \mathbf{x} would have in the case the material is unstressed. In linear elasticity, the elastic energy is a quadratic function of the strain tensor. Assuming that the elastic energy is zero at zero stress, the elastic energy can be written as [26]

$$\omega_{el} = \frac{1}{2} \int_V \sum_{iklm} C_{iklm} \left([\tilde{\varepsilon}_{ik}(\vec{r}) - \varepsilon_{ik}^0(\vec{r})] [\tilde{\varepsilon}_{lm}(\vec{r}) - \varepsilon_{lm}^0(\vec{r})] \right) dV. \quad (98)$$

Following Khachaturyan [41], the elastic strain field ε_{ij} can be written as the sum of homogeneous and heterogeneous strain strain $\tilde{\varepsilon}_{ik} = \bar{\varepsilon}_{ik} + \varepsilon_{ik}$. The homogeneous strain is assumed to take a constant value $\bar{\varepsilon}_{ik} = \varepsilon_{ik}^0 \langle h(\phi) \rangle$, where $\langle \dots \rangle$ symbolizes the averaging over the volume. The heterogeneous strain ε_{ik} should be calculated from the mechanical equilibrium conditions. With these values Eq. (98) can be written as

$$\omega_{el} = \frac{1}{2} \int_V \sum_{iklm} C_{iklm} \left([\bar{\varepsilon}_{ik} + \varepsilon_{ik}] - \varepsilon_{ik}^0 h(\phi) \right) \left([\bar{\varepsilon}_{lm} + \varepsilon_{lm}] - \varepsilon_{lm}^0 h(\phi) \right) dV. \quad (99)$$

After transformation of Eq. (99) using the property $\int_V \varepsilon_{lm} dV = 0$, we get

$$\begin{aligned} \omega_{el} &= \frac{1}{2} \int_V \sum_{iklm} C_{iklm} \varepsilon_{ik}^0 \varepsilon_{lm}^0 h^2(\phi) dV \\ &+ \frac{1}{2} \int_V \sum_{iklm} C_{iklm} \left(\varepsilon_{ik}^0 \varepsilon_{lm}^0 \langle h(\phi) \rangle^2 - 2\varepsilon_{ik}^0 \varepsilon_{lm}^0(\phi) \langle h(\phi) \rangle h(\phi) \right) dV \\ &+ \frac{1}{2} \int_V \sum_{iklm} C_{iklm} \left(\varepsilon_{ik} \varepsilon_{lm} - 2\varepsilon_{ik}^0 \varepsilon_{lm} h(\phi) \right) dV, \end{aligned} \quad (100)$$

here, the first term is the total elastic energy associated with the shape restoration of particles of the γ' -phase, the second term is the homogeneous relaxation and the last

term is the heterogeneous relaxation of the elastic energy.

3.2.2.1 Coupling of eigenstrain to phasefield

Misfit-strain effects are incorporated in the model by coupling through the dimensionless scalar field i.e, the phase field, which has no other physical meaning than to distinguish between the phases. By defining the γ -phase as the reference phase such that its eigenstrain vanishes, we get

$$\varepsilon_{ik}^0(\phi) = (1 - h(\phi)) \varepsilon_{ik}^0, \quad (101)$$

where ε_{ik}^0 are the tensor coefficients determined by the crystallography of the phases. We denote this coupling the **Eigenstrain-Phasefield (EP)**. In the γ - γ' system there are only diagonal terms of the eigenstrain

$$\varepsilon_{ik}^0(\phi) = 2 \left(\frac{a^{\gamma'} - a^\gamma}{a^{\gamma'} + a^\gamma} \right) \delta_{ik}, \quad (102)$$

where a^γ and $a^{\gamma'}$ are the lattice parameters of the matrix and precipitate, respectively and δ_{ij} is the Kronecker-delta function. Elastic anisotropy and inhomogeneity is introduced in the model by postulating the elastic constants to be constant in each phase but with different values

$$C_{ijkl}(\phi) = h(\phi)C_{ijkl}^\gamma + (1 - h(\phi))C_{ijkl}^{\gamma'}. \quad (103)$$

The stiffness tensor C_{ijkl} is symmetric under the interchange of i and j of k and l and of i, j and k, l and have symmetries reflecting the symmetries of the crystal lattice [26]. The following symmetry properties can be written

$$C_{ijkl} = C_{jikl} = C_{ijlk} = C_{klij}. \quad (104)$$

The first two symmetries arise from the symmetry of the stress and strain tensors. The last two arise from arguments based on the existence of the strain energy function. The elastic constants can be written as $C_{12} = \lambda$, $C_{11} = 2\mu + \lambda$, $C_{44} = \mu$, where λ and μ are Lamé coefficients. The elastic energy for the EP coupling is given as,

$$\omega_{el}(\phi, \vec{u}) = \frac{1}{2} \sum_{iklm} \left([\varepsilon_{ik} - \varepsilon_{ik}^0(\phi)] C_{iklm}(\phi) [\varepsilon_{lm} - \varepsilon_{lm}^0(\phi)] \right), \quad (105)$$

where the explicit expressions for $\varepsilon_{ik}^0(\phi)$ and $C_{iklm}(\phi)$ are given by Eqs. (101) and (103), respectively. Note that Eq. (105) inserted in Eq. (92) gives the elastic energy integrated over the whole volume.

Phase-field equation

The phase-field evolution shall obey the Allen-Cahn equation

$$\frac{\partial \phi}{\partial t} = -K \frac{\delta \Omega}{\delta \phi}, \quad (106)$$

where K is the kinetic coefficient and $\delta \Omega / \delta \phi$ denotes the functional derivative of the grand-potential functional with respect to the phase field order parameter. For the isothermal case, the variation of the grand-potential functional in Eq. (92) with respect to the order parameter ϕ and the diffusion field μ becomes

$$\begin{aligned} \delta \Omega = & \int dV \left\{ -3\sigma\xi \nabla^2 \phi + \frac{6\sigma}{\xi} g'(\phi) \right. \\ & + h'(\phi) \left(\frac{\partial \omega_{ch}(\mu)}{\partial h} \right) + h'(\phi) \left(\frac{\partial \omega_{el}}{\partial h} \right) \left. \right\} \delta \phi \\ & + \left\{ h(\phi) \frac{\partial \omega_{ch}^\gamma(\mu)}{\partial h} + [1 - h(\phi)] \frac{\partial \omega_{ch}^{\gamma'}(\mu)}{\partial h} \right\} \delta \mu, \end{aligned} \quad (107)$$

with the requirement that $\partial_\phi h(\phi)|_{\phi=0,1} = 0$ such that the driving force vanishes outside of the interfacial region. The partial derivative of the grand potential with respect to the phase field gives the driving force for phase transition

$$\begin{aligned} \delta \Omega = & \int dV \left\{ -3\sigma\xi \nabla^2 \phi + \frac{6\sigma}{\xi} g'(\phi) \right. \\ & + h'(\phi) \left(\frac{\partial \omega_{ch}(\mu)}{\partial h} \right) + h'(\phi) \left(\frac{\partial \omega_{el}}{\partial h} \right) \left. \right\} \delta \phi \end{aligned} \quad (108)$$

Inserting the Eq. (108) in Eq. (106) gives the explicit phase-field equation

$$\begin{aligned} \frac{\partial \phi}{\partial t} = & -\frac{K}{3\sigma\xi} \frac{\delta \Omega}{\delta \phi} \\ & K \left(\nabla^2 \phi - \frac{2}{\xi^2} g'_{dw}(\phi) \right. \\ & \left. - \frac{1}{3\sigma\xi} h'(\phi) \left[\frac{\partial \omega_{ch}(\phi, \mu)}{\partial h} + \frac{\partial \omega_{el}(\phi, \vec{u})}{\partial h} \right] \right). \end{aligned} \quad (109)$$

The first derivative of Eq. (94) gives the thermodynamic driving force

$$\begin{aligned} \frac{\partial \omega_{ch}(\phi, \mu)}{\partial h} = & \omega_{ch}^\gamma(\mu) - \omega_{ch}^{\gamma'}(\mu) \\ = & \sum_i \left(\frac{1}{2} \sum_j \Delta \chi_{ij} \mu_j - \Delta A_i \right) \mu_i + \Delta B, \end{aligned} \quad (110)$$

where $\Delta B = B^\gamma - B^{\gamma'}$, $\Delta A_i = A_i^\gamma - A_i^{\gamma'}$ and $\Delta \chi_{ij} = \chi_{ij}^\gamma - \chi_{ij}^{\gamma'}$. In a similar manner, the first derivative of Eq. (105) with respect to the interpolation function $h(\phi)$ gives the elastic driving force for phase transformation. Evaluating the derivatives of the phase dependent parameters in Eq. (105), gives the explicit elastic driving force

$$\begin{aligned}
\frac{\partial \omega_{el}(\phi, \vec{u})}{\partial h} &= \frac{\partial h(\phi)}{\partial \phi} \left(\frac{1}{2} \sum_{iklm} (\varepsilon_{ik} - \varepsilon_{ik}^0(\phi)) C_{iklm}(\phi)_{iklm} (\varepsilon_{lm} - \varepsilon_{lm}^0(\phi)) \right) \\
&= \sum_{iklm} \left(\Delta C_{iklm} (\varepsilon_{ik} - \varepsilon_{ik}^0(\phi)) (\varepsilon_{lm} - \varepsilon_{lm}^0(\phi)) \right) \\
&\quad - 2 \sum_{iklm} \left(\Delta \varepsilon_{ik}^0 C_{iklm}(\phi) (\varepsilon_{lm} - \varepsilon_{lm}^0(\phi)) \right), \\
&= \sum_{iklm} \left(\Delta C_{iklm} (\varepsilon_{ik} - [1 - h(\phi)] \varepsilon_{ik}^0) (\varepsilon_{lm} - [1 - h(\phi)] \varepsilon_{lm}^0) \right) \\
&\quad - 2 \sum_{iklm} \left(\Delta \varepsilon_{ik}^0 \left(h(\phi) C_{iklm}^\gamma + (1 - h(\phi)) C_{iklm}^{\gamma'} \right) (\varepsilon_{lm} - [1 - h(\phi)] \varepsilon_{lm}^0) \right),
\end{aligned} \tag{111}$$

where $\Delta C_{iklm} = C_{iklm}^\gamma - C_{iklm}^{\gamma'}$ and since the matrix is the reference phase $\Delta \varepsilon_{ik}^0 = \varepsilon_{ik}^0$.

Numerical solution for phase-field equation

Discretizing the time evolution of the phase-field equation using the finite difference method we get

$$\phi^{n+1}(i, j) = \phi^n(i, j) + \frac{\Delta \phi^n(i, j)}{\Delta t} \Delta t, \tag{112}$$

where n is the time index and $\Delta \phi^n(i, j)$ is the change ϕ between time step n and $n + 1$. Discretizing in space we get

$$\begin{aligned}
\frac{1}{K} \frac{\Delta \phi^n(i, j)}{\Delta t} &= \frac{1}{(\Delta x)^2} (\phi^n(i+1, j) + \phi^n(i-1, j)) \\
&\quad + \frac{1}{(\Delta x)^2} (\phi^n(i, j+1) + \phi^n(i, j-1)) \\
&\quad - \frac{1}{(\Delta x)^2} (4\phi^n(i, j)) - \frac{2}{\xi^2} g'_{dw}(\phi^n) \\
&\quad - \frac{1}{3\sigma\xi} h'(\phi^n) \left(\frac{\partial \omega_{ch}(\phi, \mu)}{\partial h} \right) + \frac{1}{3\sigma\xi} h'(\phi^n) \left(\frac{\partial \omega_{el}(\phi, \vec{u})}{\partial h} \right),
\end{aligned} \tag{113}$$

where i, j are spatial indices.

Diffusion equations

The multiple diffusion equations are formulated in the basis of the conservation con-

dition

$$\frac{\partial \bar{c}_i(\phi)}{\partial t} + \sum_j \vec{\nabla} \left(M_{ij}^p \vec{\nabla} \mu_j \right) = 0, \quad (114)$$

where $\bar{c}_i(\phi)$ is the local concentration and M_{ij}^p is the atomic mobility matrix. Further evaluation yields the equation of motion for a given species i equations for the evolution of the diffusion potential fields

$$\frac{\partial \mu_i}{\partial t} = \sum_j D_{ij} \left(\nabla^2 \mu_j \right) - \frac{\Delta A_i}{\chi_i} \frac{\partial h}{\partial \phi} \frac{\partial \phi}{\partial t}, \quad (115)$$

where the concentration difference $\Delta A_i = A_i^\gamma - A_i^{\gamma'}$ is independent from the phase field and the diffusion coefficient is defined as $D_{ij} = M_{ij}/\chi_i$. Here, the thermodynamic factors are given as $X_i = 1/\chi_i$. The concentration field for a solute i is calculated from the concentration field i as

$$c_i = \chi_i \mu_i + \left(A_i^\gamma h(\phi) + A_i^{\gamma'} (1 - h(\phi)) \right). \quad (116)$$

The constants A_i^γ and $A_i^{\gamma'}$ are related to the equilibrium compositions $c_i^{eq,\gamma}$ and $c_i^{eq,\gamma'}$ of the precipitate and matrix phase, respectively.

Numerical solution for diffusion equations

Discretizing the time evolution of the diffusion equation in Eq. (115) using the finite difference approach we get

$$\mu_k^{n+1}(i, j) = \mu_k^n(i, j) + \frac{\Delta \mu_k^n(i, j)}{\Delta t} \Delta t. \quad (117)$$

Discretizing in space as well we get

$$\begin{aligned} \frac{\Delta \mu_k^n(i, j)}{\Delta t} &= \sum_j \frac{D_{ij}}{(\Delta x)^2} (\mu_k^n(i+1, j) + \mu_k^n(i-1, j)) \\ &+ \sum_j \frac{D_{ij}}{(\Delta x)^2} (\mu_k^n(1, j+1) + \mu_k^n(i, j-1)) \\ &- \sum_j \frac{D_{ij}}{(\Delta x)^2} (4\mu_k^n(i, j)) - h'(\phi^n) \frac{\Delta A_i}{\chi_i} \frac{\Delta \phi^n(i, j)}{\Delta t}, \end{aligned} \quad (118)$$

where i and j are spatial indices and k is a species in an alloy.

Mechanical Equilibrium

To calculate the elastic driving force $\partial\omega_{el}/\partial h$ for phase transformation in Eq. (111), the displacement u_i at each point in space is required. In the case of solid-state phase transformations controlled by atomic diffusion, static elasticity (elastic equilibrium) is assumed since elastic energy as described by the displacement field u_i equilibrates much faster than the characteristic diffusion time. In other words, the time for the relaxation of the displacement field is much shorter than that of the solute diffusion field. Therefore, displacement rapidly reaches equilibrium on the timescale of solute diffusion. The condition determining the displacement fields u_i is that it should minimize the elastic energy. The equation for this minimization, is called the equation of the mechanical equilibrium. The solution of the elastic equilibrium is obtained by minimizing the grand potential functional with respect to the displacement together with the boundary conditions

$$\frac{\delta\Omega}{\delta u_k} = \sum_k \frac{\partial\sigma_{ik}(\phi)}{\partial x_k} = 0, \quad (119)$$

where the stress tensor is phase field dependent due to the dependence of the cubic elastic constants and eigenstrain on the phase field. The stress tensor in (119) is defined as the partial derivative of the elastic energy with respect to the strain tensor

$$\sigma_{ik}(\phi) = \frac{\partial\omega_{el}(\phi, \vec{u})}{\partial u_{i,k}}, \quad (120)$$

where $u_{i,k}$ is $\partial u_i/\partial x_k$. The stress tensor is related to the strain tensor by the Hooke's law

$$\sigma_{ik}(\phi) = \sum_{iklm} C_{iklm}(\phi)(\varepsilon_{lm} - \varepsilon_{lm}^0(\phi)), \quad (121)$$

where $\varepsilon_{lm}^0(\phi)$ and $C_{iklm}(\phi)$ are described in the Eqs. (101) and (103), respectively. A complete description of the equilibrium problem requires the assignment of necessary conditions on the elastic field variables at the interfaces and domain boundaries [26]. For a two phase coherent microstructure, conditions of the continuity of atomic displacement are set

$$[\mathbf{u}] = 0 \quad (122)$$

where $[\mathbf{u}]$ for the two phase $\gamma - \gamma'$ microstructure is $[\mathbf{u}]_{\gamma'}^{\gamma}$, which means $u^\gamma - u^{\gamma'}$, which is the difference in limiting values of \mathbf{u} at the γ' -precipitate and γ -matrix side of the interface. In addition to that, the values taken by the displacement fields \mathbf{u} at the interface in a deformed body should satisfy the energy minimizing condition. By assuming that the energy of the interface depends only on the position relative to the lattice, the surface energy is therefore not changed by changes in the displacement field at the interface and

the minimization of the elastic energy gives

$$\sum_k [\sigma_{ik}] n_k = 0, \quad (123)$$

where $[\sigma_{ik}]$ means $\sigma_{ik}^\gamma - \sigma_{ik}^{\gamma'}$ and \mathbf{n} is the vector normal to the interface. The meaning of (123) is that the forces exerted on the γ' -precipitate and the γ -matrix side of the interface are equal and opposite. The boundary conditions on the domain boundary depend on the physical conditions. For this work, periodic boundary conditions taking the domain Ψ to be rectangular or squared are used. The periodic boundary conditions require that strain and stress fields are periodic with unit cell Ψ .

The three dimensional elasticity problem can effectively be simplified to a two directional problem by using the plane strain geometry assumption where the displacement vector in one given direction equals zero and therefore vanishes. The displacement vector in the z -direction is chosen to be zero and the other components do not depend on the z -coordinate which gives the condition

$$u_x = u_x(x, y); \quad u_y = u_y(x, y); \quad u_z = 0. \quad (124)$$

Therefore, the strain components ε_{zz} , ε_{xz} and ε_{yz} are zero. We recall that C_{iklm} is symmetric under the interchange of i and j of m and n and of the pair i, j and m, n . As a result, there are three independent elastic constants in a cubic system, i.e., C_{11} , λ and μ and the stress-strain relation follows

$$\begin{pmatrix} \sigma_{xx} \\ \sigma_{yy} \\ \sigma_{zz} \\ \sigma_{yz} \\ \sigma_{xz} \\ \sigma_{xy} \end{pmatrix} = \begin{pmatrix} C_{11} & \lambda & \lambda & 0 & 0 & 0 \\ \lambda & C_{11} & \lambda & 0 & 0 & 0 \\ \lambda & \lambda & C_{11} & 0 & 0 & 0 \\ 0 & 0 & 0 & \mu & 0 & 0 \\ 0 & 0 & 0 & 0 & \mu & 0 \\ 0 & 0 & 0 & 0 & 0 & \mu \end{pmatrix} \begin{pmatrix} \varepsilon_{xx} \\ \varepsilon_{yy} \\ \varepsilon_{zz} \\ 2\varepsilon_{yz} \\ 2\varepsilon_{xz} \\ 2\varepsilon_{xy} \end{pmatrix}. \quad (125)$$

Since the strain components ε_{zz} , ε_{xz} and ε_{yz} are zero, consequently, the components σ_{xz} and σ_{yz} of the stress tensor also vanish. Taking into account the plane strain geometry assumption, the mechanical equilibrium in Eq. (119) for the two dimensional elasticity problem is written as

$$0 = \frac{\partial \sigma_{xx}(\phi)}{\partial x} + \frac{\partial \sigma_{xy}(\phi)}{\partial y}, \quad (126)$$

$$0 = \frac{\partial \sigma_{yy}(\phi)}{\partial y} + \frac{\partial \sigma_{xy}(\phi)}{\partial x}. \quad (127)$$

Using the relations (101) and (103) in (121), the diagonal terms of the phase dependent

stress tensors are given as

$$\begin{aligned}
\sigma_{xx}(\phi) &= C_{11}(\phi) [\varepsilon_{xx} - \varepsilon_{xx}^0(\phi)] + \lambda(\phi) [\varepsilon_{yy} - \varepsilon_{yy}^0(\phi)] - \lambda(\phi) [\varepsilon_{zz}^0(\phi)] \\
&= [h(\phi)C_{11}^\gamma + (1-h(\phi))C_{11}^{\gamma'}] [\varepsilon_{xx} - [1-h(\phi)]\varepsilon_{xx}^0] \\
&\quad + [h(\phi)\lambda^\gamma + (1-h(\phi))\lambda^{\gamma'}] [\varepsilon_{yy} - [1-h(\phi)]\varepsilon_{yy}^0] \\
&\quad - [h(\phi)\lambda^\gamma + (1-h(\phi))\lambda^{\gamma'}] [1-h(\phi)]\varepsilon_{zz}^0, \tag{128}
\end{aligned}$$

$$\begin{aligned}
\sigma_{yy}(\phi) &= \lambda(\phi) [\varepsilon_{xx} - \varepsilon_{xx}^0(\phi)] + C_{11}(\phi) [\varepsilon_{yy} - \varepsilon_{yy}^0(\phi)] - \lambda(\phi) [\varepsilon_{zz}^0(\phi)] \\
&= [h(\phi)\lambda^\gamma + (1-h(\phi))\lambda^{\gamma'}] [\varepsilon_{xx} - [1-h(\phi)]\varepsilon_{xx}^0] \\
&\quad + [h(\phi)C_{11}^\gamma + (1-h(\phi))C_{11}^{\gamma'}] [\varepsilon_{yy} - [1-h(\phi)]\varepsilon_{yy}^0] \\
&\quad - [h(\phi)\lambda^\gamma + (1-h(\phi))\lambda^{\gamma'}] [1-h(\phi)]\varepsilon_{zz}^0, \tag{129}
\end{aligned}$$

and the shear stress is given as

$$\begin{aligned}
\sigma_{xy}(\phi) &= 2\mu(\phi) [\varepsilon_{xy} - \varepsilon_{xy}^0(\phi)] \\
&= 2[h(\phi)\mu^\gamma + (1-h(\phi))\mu^{\gamma'}] [\varepsilon_{xy} - [1-h(\phi)]\varepsilon_{xy}^0]. \tag{130}
\end{aligned}$$

Inserting (128) and (130) into (126), we get the equation

$$\begin{aligned}
0 &= \frac{\partial}{\partial x} \left[(h(\phi)C_{11}^\gamma + (1-h(\phi))C_{11}^{\gamma'}) (\varepsilon_{xx} - [1-h(\phi)]\varepsilon_{xx}^0) \right. \\
&\quad + (h(\phi)\lambda^\gamma + (1-h(\phi))\lambda^{\gamma'}) (\varepsilon_{yy} - [1-h(\phi)]\varepsilon_{yy}^0) \\
&\quad \left. - (h(\phi)\lambda^\gamma + (1-h(\phi))\lambda^{\gamma'}) [1-h(\phi)]\varepsilon_{zz}^0 \right] \\
&\quad + 2\frac{\partial}{\partial y} \left[(h(\phi)\mu^\gamma + (1-h(\phi))\mu^{\gamma'}) (\varepsilon_{xy} - [1-h(\phi)]\varepsilon_{xy}^0) \right]. \tag{131}
\end{aligned}$$

Likewise, inserting (129) and (130) into (127) yields the equation

$$\begin{aligned}
0 &= \frac{\partial}{\partial y} \left[(h(\phi)\lambda^\gamma + (1-h(\phi))\lambda^{\gamma'}) (\varepsilon_{xx} - [1-h(\phi)]\varepsilon_{xx}^0) \right. \\
&\quad + (h(\phi)C_{11}^\gamma + (1-h(\phi))C_{11}^{\gamma'}) (\varepsilon_{yy} - [1-h(\phi)]\varepsilon_{yy}^0) \\
&\quad \left. - (h(\phi)\lambda^\gamma + (1-h(\phi))\lambda^{\gamma'}) [1-h(\phi)]\varepsilon_{zz}^0 \right] \\
&\quad + 2\frac{\partial}{\partial x} \left[(h(\phi)\mu^\gamma + (1-h(\phi))\mu^{\gamma'}) (\varepsilon_{xy} - [1-h(\phi)]\varepsilon_{xy}^0) \right]. \tag{132}
\end{aligned}$$

The equations (131) and (132) need to be solved numerically to obtain the u_x and u_y displacement fields necessary for the calculation of the elastic driving force $\partial\omega_{el}/\partial h$ (in

Eq. 111) required in (Eq. 109) to change the phase field order parameter.

Numerical solution for the mechanical equilibrium

To obtain the u_x and u_y displacement fields, Eqs. (131) and (132) are solved, respectively, using a Jacobi relaxation [8] based on the explicit finite difference with elastic variables on a staggered grid [19, 57]. Before describing the Jacobi relaxation scheme, we first look at the numerical discretization of Eqs. (131) and (132) using a staggered grid. The staggered grid used to solve the two equations is illustrated in Fig 16. The staggered grid has three different lattices which are shifted by $\Delta x/2$. In the staggered

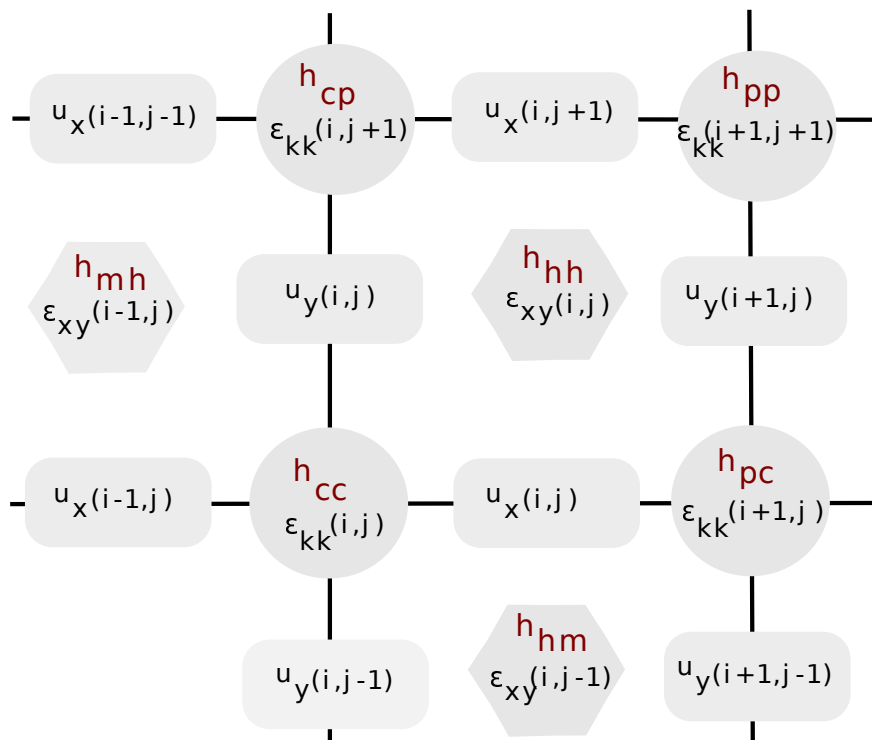


Figure 16: Staggered grid: The interpolation functions $h(\phi)$ are defined on the normal grid depicted by the circles and the displacement fields u_x and u_y are defined them shifted by $\Delta x/2$. The shear strains at the square centers represented by the hexagons also shifted by $\Delta x/2$. Values for the interpolation function $h(\phi)$ at the square centers are also required. The elasticity equations are only space dependent and can therefore be solved independently from the phase-field and concentration evolution equations.

grid, the diagonal terms of the strain tensor are located at the grid points (represented by the circles) and the shear strains at the square centers (represented by the hexagons). The displacements are located in between the grid points (represented by the rectangles)

shifted by $\Delta x/2$. The elastic constants $C_{iklm}(\phi)$ and eigenstrain $\varepsilon_{ik}^0(\phi)$ are phase field dependent through the coupling via the interpolation function $h(\phi)$. Thus, for the calculation of the elastic constants and eigenstrain at the grid points (circles), the following discretized interpolation functions at the circles are required

$$h_{cc} = h(\phi(i, j)), \quad (133)$$

$$h_{pc} = h(\phi(i + 1, j)), \quad (134)$$

$$h_{cp} = h(\phi(i, j + 1)), \quad (135)$$

$$h_{pp} = h(\phi(i + 1, j + 1)). \quad (136)$$

The discretized elastic constants and eigenstrain at the grid points (i, j) are

$$C_{11}(i, j) = h_{cc}C_{11}^\gamma + (1 - h_{cc})C_{11}^{\gamma'}, \quad (137)$$

$$\lambda(i, j) = h_{cc}\lambda^\gamma + (1 - h_{cc})\lambda^{\gamma'}, \quad (138)$$

$$\mu(i, j) = h_{cc}\mu^\gamma + (1 - h_{cc})\mu^{\gamma'}, \quad (139)$$

$$\varepsilon_{kl}^0(i, j) = \varepsilon_{kl}^0(1 - h_{cc}), \quad (140)$$

where the interpolation function at grid point (i, j) i.e., h_{cc} which is defined in (133). The discretized elastic constants and eigenstrain at the grid points $(i + 1, j)$ are

$$C_{11}(i + 1, j) = h_{pc}C_{11}^\gamma + (1 - h_{pc})C_{11}^{\gamma'}, \quad (141)$$

$$\lambda(i + 1, j) = h_{pc}\lambda^\gamma + (1 - h_{pc})\lambda^{\gamma'}, \quad (142)$$

$$\mu(i + 1, j) = h_{pc}\mu^\gamma + (1 - h_{pc})\mu^{\gamma'}, \quad (143)$$

$$\varepsilon_{kl}^0(i + 1, j) = \varepsilon_{kl}^0(1 - h_{pc}), \quad (144)$$

where interpolation function h_{pc} at the circle point $(i + 1, j)$ is defined in (134). For the calculation of elastic constants and eigenstrain at the square center (hexagons), discretized interpolation functions are also required at the hexagons

$$h_{hh}(i + 1/2, j + 1/2) = 0.25 [h(i, j) + h(i + 1, j) + h(i, j + 1) + h(i + 1, j + 1)], \quad (145)$$

$$h_{mh}(i - 1/2, j + 1/2) = 0.25 [h(i - 1, j) + h(i, j) + h(i - 1, j + 1) + h(i, j + 1)], \quad (146)$$

$$h_{hm}(i + 1/2, j - 1/2) = 0.25 [h(i, j - 1) + h(i + 1, j - 1) + h(i, j) + h(i + 1, j)].$$

At the hexagon $(i + 1/2, j + 1/2)$, the elastic constants and eigenstrain are calculated as

$$C_{11}(i + 1/2, j + 1/2) = h_{hh}C_{11}^{\gamma} + (1 - h_{hh})C_{11}^{\gamma'}, \quad (147)$$

$$\lambda(i + 1/2, j + 1/2) = h_{hh}\lambda^{\gamma} + (1 - h_{hh})\lambda^{\gamma'}, \quad (148)$$

$$\mu(i + 1/2, j + 1/2) = h_{hh}\mu^{\gamma} + (1 - h_{hh})\mu^{\gamma'}, \quad (149)$$

$$\varepsilon_{kl}^0(i + 1/2, j + 1/2) = \varepsilon_{kl}^0(1 - h_{hh}), \quad (150)$$

where interpolation function h_{hh} is defined in (145). Likewise, at the hexagon $(i - 1/2, j + 1/2)$, the elastic constants and eigenstrain are calculated as

$$C_{11}(i - 1/2, j + 1/2) = h_{mh}C_{11}^{\gamma} + (1 - h_{mh})C_{11}^{\gamma'}, \quad (151)$$

$$\lambda(i - 1/2, j + 1/2) = h_{mh}\lambda^{\gamma} + (1 - h_{mh})\lambda^{\gamma'}, \quad (152)$$

$$\mu(i - 1/2, j + 1/2) = h_{mh}\mu^{\gamma} + (1 - h_{mh})\mu^{\gamma'}, \quad (153)$$

$$\varepsilon_{kl}^0(i - 1/2, j + 1/2) = \varepsilon_{kl}^0(1 - h_{mh}), \quad (154)$$

where interpolation function h_{mh} is defined in (146). The three non-zero elements of the strain tensor are calculated as

$$\varepsilon_{xx}(i, j) = (u_x(i, j) - u_x(i - 1, j))/\Delta x, \quad (155)$$

$$\varepsilon_{yy}(i, j) = (u_y(i, j) - u_y(i, j - 1))/\Delta x, \quad (156)$$

$$\varepsilon_{xy}(i, j) = \frac{1}{2\Delta x} (u_x(i, j + 1) - u_x(i, j) + u_y(i + 1, j) - u_y(i, j)). \quad (157)$$

Using Eqs. (133)-(157), the spatial derivatives of the stresses in Eqs. (131) and (132) are now discretized as,

$$\begin{aligned} \frac{\partial \sigma_{xx}(\phi)}{\partial x} = & \left(C_{11}(i + 1, j)([u_x(i + 1, j) - u_x(i, j)] - \varepsilon_{xx}^0(i + 1, j)) \right. \\ & - C_{11}(i, j)([u_x(i, j) - u_x(i - 1, j)] - \varepsilon_{xx}^0(i, j)) \\ & + \lambda(i + 1, j)([u_y(i + 1, j) - u_y(i + 1, j - 1)] - \varepsilon_{yy}^0(i + 1, j)) \\ & - \lambda(i, j)([u_y(i, j) - u_y(i, j - 1)] - \varepsilon_{yy}^0(i, j)) \\ & \left. - \lambda(i + 1, j)\varepsilon_{zz}^0(i + 1, j) + \lambda(i, j)\varepsilon_{zz}^0(i, j) \right) / \Delta x^2, \end{aligned} \quad (158)$$

$$\begin{aligned} \frac{\partial \sigma_{xy}(\phi)}{\partial y} = & (2\mu(i + 1/2, j + 1/2)([u_x(i, j + 1) - u_x(i, j)] \\ & - \varepsilon_{xy}^0(i + 1/2, j + 1/2)) \\ & - 2\mu(i + 1/2, j - 1/2)([u_x(i, j) - u_x(i, j - 1)] \\ & - \varepsilon_{xy}^0(i + 1/2, j - 1/2))) / \Delta x^2, \end{aligned} \quad (159)$$

$$\begin{aligned}
\frac{\partial \sigma_{yy}(\phi)}{\partial y} &= \left(\lambda(i, j+1)([u_x(i, j+1) - u_x(i-1, j+1)] - \varepsilon_{xx}^0(i, j+1)) \right. \\
&\quad - \lambda(i, j)([u_x(i, j) - u_x(i-1, j)] - \varepsilon_{xx}^0(i, j)) \\
&\quad + C_{11}(i, j+1)([u_y(i, j+1) - u_y(i, j)] - \varepsilon_{yy}^0(i, j+1)) \\
&\quad - C_{11}(i, j)([u_y(i, j) - u_y(i, j-1)] - \varepsilon_{yy}^0(i, j)) \\
&\quad \left. - \lambda(i, j+1)\varepsilon_{zz}^0(i, j+1) + \lambda(i, j)\varepsilon_{zz}^0(i, j) \right) / \Delta x^2,
\end{aligned} \tag{160}$$

$$\begin{aligned}
\frac{\partial \sigma_{xy}(\phi)}{\partial x} &= \left(2\mu(i+1/2, j+1/2)([u_y(i+1, j) - u_y(i, j)] \right. \\
&\quad - \varepsilon_{xy}^0(i+1/2, j+1/2)) \\
&\quad - 2\mu(i-1/2, j+1/2)([u_x(i, j) - u_x(i-1, j)] \\
&\quad \left. - \varepsilon_{xy}^0(i-1/2, j+1/2)) \right) / \Delta x^2.
\end{aligned} \tag{161}$$

Inserting the discretized spatial stresses Eqs. (158) and (159) into (131) gives

$$\begin{aligned}
0 &= \left(C_{11}(i+1, j)([u_x(i+1, j) - u_x(i, j)] - \varepsilon_{xx}^0(i+1, j)) \right. \\
&\quad - C_{11}(i, j)([u_x(i, j) - u_x(i-1, j)] - \varepsilon_{xx}^0(i, j)) \\
&\quad + \lambda(i+1, j)([u_y(i+1, j) - u_y(i+1, j-1)] - \varepsilon_{yy}^0(i+1, j)) \\
&\quad - \lambda(i, j)([u_y(i, j) - u_y(i, j-1)] - \varepsilon_{yy}^0(i, j)) \\
&\quad - \lambda(i+1, j)\varepsilon_{zz}^0(i+1, j) + \lambda(i, j)\varepsilon_{zz}^0(i, j) \\
&\quad + 2\mu(i+1/2, j+1/2)([u_x(i, j+1) - u_x(i, j)] \\
&\quad - \varepsilon_{xy}^0(i+1/2, j+1/2)) - 2\mu(i+1/2, j-1/2)([u_x(i, j) - u_x(i, j-1)] \\
&\quad \left. - \varepsilon_{xy}^0(i+1/2, j-1/2)) \right) / \Delta x^2,
\end{aligned} \tag{162}$$

and inserting Eqs. (160) and (161) into (132) results in

$$\begin{aligned}
0 &= \left(\lambda(i, j+1)([u_x(i, j+1) - u_x(i-1, j+1)] - \varepsilon_{xx}^0(i, j+1)) \right. \\
&\quad - \lambda(i, j)([u_x(i, j) - u_x(i-1, j)] - \varepsilon_{xx}^0(i, j)) \\
&\quad + C_{11}(i, j+1)([u_y(i, j+1) - u_y(i, j)] - \varepsilon_{yy}^0(i, j+1)) \\
&\quad - C_{11}(i, j)([u_y(i, j) - u_y(i, j-1)] - \varepsilon_{yy}^0(i, j)) \\
&\quad - \lambda(i, j+1)\varepsilon_{zz}^0(i, j+1) + \lambda(i, j)\varepsilon_{zz}^0(i, j) \\
&\quad + (2\mu(i+1/2, j+1/2)([u_y(i+1, j) - u_y(i, j)] \\
&\quad - \varepsilon_{xy}^0(i+1/2, j+1/2)) - 2\mu(i-1/2, j+1/2)([u_x(i, j) - u_x(i-1, j)] \\
&\quad \left. - \varepsilon_{xy}^0(i-1/2, j+1/2)) \right) / \Delta x^2.
\end{aligned} \tag{163}$$

The equations of the mechanical equilibrium (162) and (163) are solved iteratively in each time step n by means of a Jacobi relaxation scheme [8, 21] to yield the u_x and u_y

displacement fields,

$$\begin{aligned}
\frac{\partial u_x}{\partial t^*} = & \left(C_{11}(i+1, j)([u_x(i+1, j) - u_x(i, j)] - \varepsilon_{xx}^0(i+1, j)) \right. \\
& - C_{11}(i, j)([u_x(i, j) - u_x(i-1, j)] - \varepsilon_{xx}^0(i, j)) \\
& + \lambda(i+1, j)([u_y(i+1, j) - u_y(i+1, j-1)] - \varepsilon_{yy}^0(i+1, j)) \\
& - \lambda(i, j)([u_y(i, j) - u_y(i, j-1)] - \varepsilon_{yy}^0(i, j)) \\
& - \lambda(i+1, j)\varepsilon_{zz}^0(i+1, j) + \lambda(i, j)\varepsilon_{zz}^0(i, j) \\
& + 2\mu(i+1/2, j+1/2)([u_x(i, j+1) - u_x(i, j)] \\
& - \varepsilon_{xy}^0(i+1/2, j+1/2)) - 2\mu(i+1/2, j-1/2)([u_x(i, j) - u_x(i, j-1)] \\
& \left. - \varepsilon_{xy}^0(i+1/2, j-1/2)) \right) / \Delta x^2, \tag{164}
\end{aligned}$$

$$\begin{aligned}
\frac{\partial u_y}{\partial t^*} = & \left(\lambda(i, j+1)([u_x(i, j+1) - u_x(i-1, j+1)] - \varepsilon_{xx}^0(i, j+1)) \right. \\
& - \lambda(i, j)([u_x(i, j) - u_x(i-1, j)] - \varepsilon_{xx}^0(i, j)) \\
& + C_{11}(i, j+1)([u_y(i, j+1) - u_y(i, j)] - \varepsilon_{yy}^0(i, j+1)) \\
& - C_{11}(i, j)([u_y(i, j) - u_y(i, j-1)] - \varepsilon_{yy}^0(i, j)) \\
& - \lambda(i, j+1)\varepsilon_{zz}^0(i, j+1) + \lambda(i, j)\varepsilon_{zz}^0(i, j) \\
& + (2\mu(i+1/2, j+1/2)([u_y(i+1, j) - u_y(i, j)] \\
& - \varepsilon_{xy}^0(i+1/2, j+1/2)) - 2\mu(i-1/2, j+1/2)([u_x(i, j) - u_x(i-1, j)] \\
& \left. - \varepsilon_{xy}^0(i-1/2, j+1/2)) \right) / \Delta x^2. \tag{165}
\end{aligned}$$

where t^* is the pseudo time with the property that $t^* \rightarrow \infty$, which satisfies the condition of the mechanical equilibrium. The elasticity equations are only space dependent and can therefore be solved independently from the phase-field and diffusion equations. While the elastic fields are relaxed to fulfill the mechanical equilibrium conditions, the phase fields are fixed. Once the displacement fields u_x and u_y are found, the corresponding elements of the strain tensor ε_{xx} , ε_{yy} and ε_{xz} are calculated using (155), (156) and (157), respectively. The elements of the strain tensor ε_{xx} , ε_{yy} and ε_{xz} are then used to calculate the elastic driving force for phase transformation $\partial\omega_{el}/\partial h$ in Eq. (111). The $\partial\omega_{el}/\partial h$ obtained at time step n is then used in Eqs. (109) and (115) to calculate the phase field and diffusion potential fields, respectively, at the next time step $n+1$. The algorithm based on the Jacobi relaxation scheme is described in detail in the Appendix.

3.2.2 Equilibrium morphology of a coherent γ' -precipitate

The morphology of coherent γ' -precipitates in Ni-base superalloys affect the resulting internal strains which in turn influences the resulting thermo-mechanical properties. In this subsection, we investigate the morphological evolution of γ' -precipitates during precipitation treatment (PT) of an elastically inhomogeneous and anisotropic single crystal superalloy with a negative misfit. Of particular interest is the equilibrium morphologies of the coherent γ' -precipitates. We start the simulations from a uniform γ -matrix which mimics the microstructure after the solution treatment (ST). The composition of the CMSX4 superalloy used in the simulation is given in Table 3. The simulation of precipitation treatment is done at a constant temperature of 1273.15 K. To allow for a continuous domain, periodic boundary conditions are applied in all directions. The simulation is performed on a system of size $451 \times 451 \Delta x$ with a grid spacing of $\Delta x = 8.6$ nm in both directions. At first morphological evolution is studied for the case of a single precipitate and then for the case of multiple precipitates.

3.2.3.1 Growth of a single γ' -precipitate

The simulation is initiated by placing a small spherical precipitate with radius $15\Delta x$ at the center of the simulation domain. The initial precipitate size is chosen such that it grows. The γ and γ' phases have a uniform initial concentration but with different diffusion potentials. It is observed that the precipitate grows until an equilibrium volume fraction of 50%. The precipitate changed its morphology from a sphere (circle in 2D) to a cube (square in 2D) as shown in Fig 17.

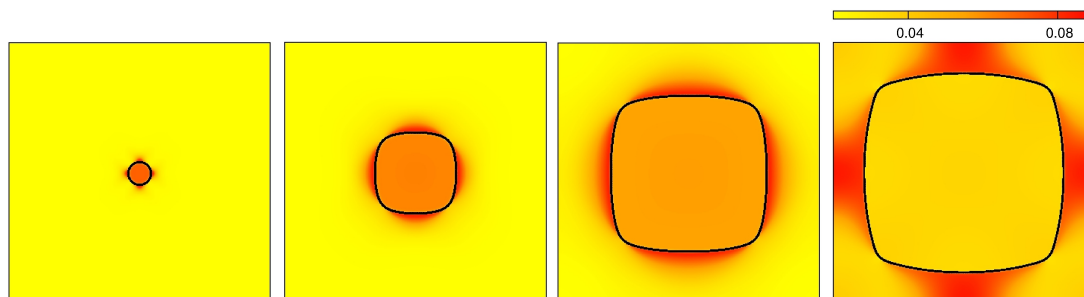


Figure 17: Sphere→cube transition in an elastically inhomogeneous and negatively misfitting Ni-base superalloy. The elastic energy density distribution during sphere to cube transition. The edges of the growing cuboidal precipitate lie along the elastically soft $\langle 100 \rangle$ -crystallographic directions.

The morphological change is a result of the crystallographic anisotropy in the growth rate of the precipitate due to varying elastic driving forces in different orientations. Small γ' -precipitates are generally in the shape of spheres. Generally, a sphere has 1.24 less surface area than a cube, therefore the precipitate tends to be spherical in shape to minimize the surface energy. However, when the precipitates are coherently embedded

in a matrix, the precipitates align along the elastically soft $\langle 100 \rangle$ crystallographic orientations as shown in Fig 17. Other factors like the long-elastic interactions and the diffusion fields around the precipitate also affect the precipitate morphology. In the following sections, we look at the influence of long-range elastic interactions of precipitate morphology. The influence of the diffusion fields on the morphology shall be studied in the following chapters.

3.2.3.2 Growth and coarsening of multiple γ' -precipitates

We now study the growth and coarsening of multiple precipitates. Data on the nucleation rate in the superalloy under study is readily not available in the literature. To mimic the different nucleation rates and sites, the simulation is started from a microstructure consisting of randomly distributed quasi-spherical precipitates of different sizes embedded within the matrix. The phase-field simulation of microstructural evolution during the precipitation of the γ' -phase at 1273.15 K is shown in Fig 18. The γ and γ' phases have a uniform initial concentration but with different diffusion potentials.

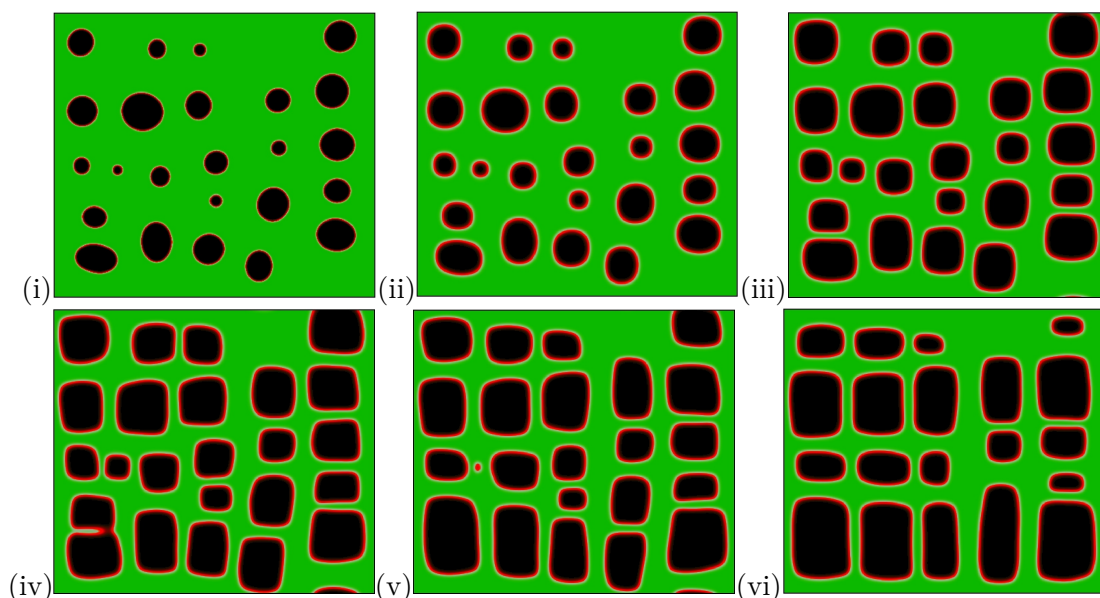


Figure 18: Phase-field simulation of microstructural evolution during precipitation of the γ' -phase in Ni-base superalloys at 1273.15 K. The evolution involves two stages; growth and coarsening. Growth occurs to satisfy local mass balance at the $\gamma - \gamma'$ interface while coarsening minimizes the total energy of the system.

The simulated evolution of multiple precipitates in Fig 18 reveals two regimes - growth and coarsening. Precipitate growth occurs to satisfy local mass balance in the vicinity of each $\gamma - \gamma'$ interface [38]. In the coarsening regime, larger precipitates with low curvature grow at the expense of the smaller ones with high curvature which results in the

minimization of the total energy of the system. The precipitates grow diffusively until an equilibrium volume fraction of around 50% is reached after which coarsening through the ripening mechanism regime occurs. During the transformation, the precipitates transform their shape from the initial quasi-sphere to quasi-cubes with a $(100)_{\gamma} \parallel (100)_{\gamma'}$ orientation relationship. The morphological change of the precipitates is a result of the interplay between the isotropic interfacial energy and cubic elasticity. Since the interfacial energy is assumed isotropic, the resulting cuboidal morphology is attributable entirely to the contribution from cubic elasticity.

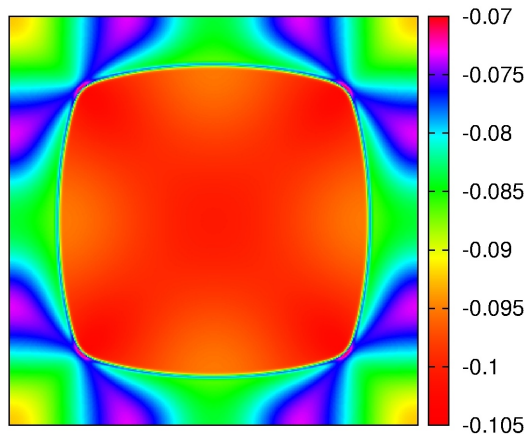


Figure 19: In this figure, we show the non-dimensional elastic driving force for phase transformation $\delta f_{el}/\delta h$. The elastic driving force is larger along the $\langle 111 \rangle$ -crystallographic directions than along the $\langle 100 \rangle$ -crystallographic directions. The anisotropic elastic driving forces results in faster growth rates along the $\langle 111 \rangle$ -crystallographic directions than along the $\langle 100 \rangle$ -crystallographic directions which gradually transforms the morphology of the γ' -precipitates from the initial spheres to cubes.

To highlight the influence of the isotropic interfacial and anisotropic elastic energies on precipitate shape, we consider a simple sphere of radius R ; the interfacial energy for a sphere is $f_{int} = 4\pi\sigma R$, where σ is the surface energy and the elastic energy of the same sphere is $f_{el} = (4\pi R^3/3)/C\varepsilon^2$, where C is the shear modulus and ε is the stress-free transformation strain. The interfacial and elastic energies are equal when $R \sim R_0 = 6\sigma/C\varepsilon^2$. When $R < R_0$, the interfacial energy has a dominant effect on the morphology of the precipitate. When $R > R_0$, the influences of anisotropic elastic energy on the morphology becomes dominant. Therefore, when the size is relatively small, the precipitates are generally spheres changing to cubes as the size increases [26]. The sphere to cube transition is attributed to the anisotropic elastic driving force $\delta f_{el}/\delta h$ shown for a single precipitate in Fig 19. The elastic driving force is considerably larger than along the $\langle 111 \rangle$ -crystallographic directions than along the $\langle 100 \rangle$ -crystallographic directions. This results in a faster interface motion along the $\langle 111 \rangle$ -crystallographic directions than along the $\langle 100 \rangle$ -crystallographic directions which gradually transforms the

morphology of the γ' -precipitates from the initial spheres to cubes. The cuboidal morphology and $(100)_{\gamma} \parallel (100)_{\gamma'}$ orientation relationship allows the crystallographic planes of the two phases to remain continuous at the interface which minimizes the interfacial energy [41, 48]. To maintain lattice continuity, the misfit between the two phases is accommodated by elastic displacement of atoms from their equilibrium positions in the vicinity of the interfaces. The distortion of the lattices generates elastic strain energy which influences the nature of microstructure evolution.

3.2.3 Effect of elastic inhomogeneity on morphological evolution

In this subsection, we investigate the influence of elastic inhomogeneity on morphological evolution during long term aging. For the sake of comparison, the initial configurations of our simulations are the same. The initial configurations correspond to the phase field in Fig 20 generated from an SEM photograph. In the following, we describe the method we use to generate the initial microstructure, this is then followed immediately by the results of the phase-field simulations of coarsening in the presence of different strengths of elastic inhomogeneity.

3.2.5.1 Generation of initial microstructure from SEM picture

Before long-term aging, the sample of the CMSX4 superalloy was vacuum heat treated with a standardized three-step cycle, which included solution treatment (ST) for the dissolution of residual eutectic and solutioning of γ' -particles. The sample was then given two precipitation treatments (PT1 & PT2) at high and low temperature, to form the typical cuboidal shape, size and distribution of the γ' -precipitates. The heat treatment procedure is described in Table 2.

Sample	Heat treatment conditions
CMSX4	AR: as received, no heat treatment ST: 1090°C/1h+ 1305°C/6h vacuum atmosphere then fast cooling $> 150^{\circ}\text{C min}^{-1}$ PT1: 1140°C/4h inert gas atmosphere \rightarrow air cooling PT2: 870°C/16h inert gas atmosphere \rightarrow air cooling

Table 2: Standard heat treatment of the CMSX4 sample.

The initial microstructure for the multiple particle simulations is obtained from the SEM photograph of an as-heat treated sample of CMSX4 shown in Fig 20 (a). Using the standard unix/linux program ImageMagick, we can convert standard pixel-graphics into an ASCII-file containing a list of all the RGB-values for each pixel. Since, we operate on a square-grid, similar to standard pixel graphic formats, we can directly read in these RGB-values for each pixel, and can calculate a phase field value out of the given colour values. Consequently, using a one to one correspondence between a pixel-graphic of size 409×357 , we obtain a phase field simulation domain of the same size. The grid spacing

of $\Delta x = 8.6$ nm is then estimated from the given SEM resolution. However, the resulting phase field does not yet exhibit the desired smooth tanh-type interface profiles with a constant interface width given by ξ . Moreover, it is not compatible with the employed periodic boundary conditions that are used in the simulations as some particles are cut by the boundary of the simulation box. In order to overcome such inconsistencies in the determined phase field, we perform a small and limited number of relaxation steps.

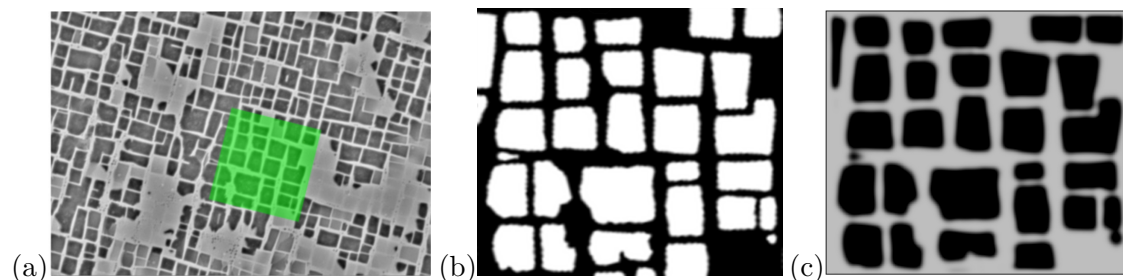


Figure 20: The initial microstructure used in the simulations (a) SEM photograph of CMSX4 [44]; the area marked in green represents the sampled area (b) Phase field of size $3.5\mu\text{m} \times 3.0\mu\text{m}$ obtained directly from SEM photographs; some particles are cut by the boundary of the simulation box (c) Initial microstructure used in the simulations; the interfaces are smooth with typical hyperbolic tangent-like profiles.

Such initial phase field relaxation is done using the same phase-field model including the presence of cubic elasticity to preserve the shapes of the precipitates but without the application of external loads. After the phase field relaxation, the interfaces, as shown in Fig 20 (c), are smooth with the desired tanh-like profiles of constant width $\xi = 2.5\Delta x$. During the relaxation, the volume fraction decreased from nearly the thermodynamic equilibrium phase fraction of 56% to about 54%.

3.2.5.2 Morphological pattern dependence on degree of elastic inhomogeneity

We first focus on morphological evolution of an elastically anisotropic and homogeneous system. Fig 21 shows morphological evolution of a system where both the matrix and precipitate phases have equal elastic constants ($C_{ij}^{\gamma'} = C_{ij}^{\gamma}$). The red area represents the γ' -phase and the blue area is the γ -matrix. During long-term aging of the homogeneous system, the matrix phase aligns itself and reshapes the γ' -precipitates to reduce the elastic energy. The precipitates form a mesh-like structure aligned along the soft directions. The system has a negative anisotropy factor, i.e. $\xi_A = C_{11} - C_{12} - 2C_{44} < 0$, the elastically soft directions correspond to the [100] and [010]-crystallographic directions.

We now investigate morphological evolution of an elastically anisotropic and inhomogeneous system. Fig. 22 shows the morphological evolution of a system with where matrix and precipitate phases have different elastic constants. The elastic constants of the γ' -precipitates are larger than those of the γ -matrix ($C_{ij}^{\gamma'} = 0.75C_{ij}^{\gamma}$). The parameter

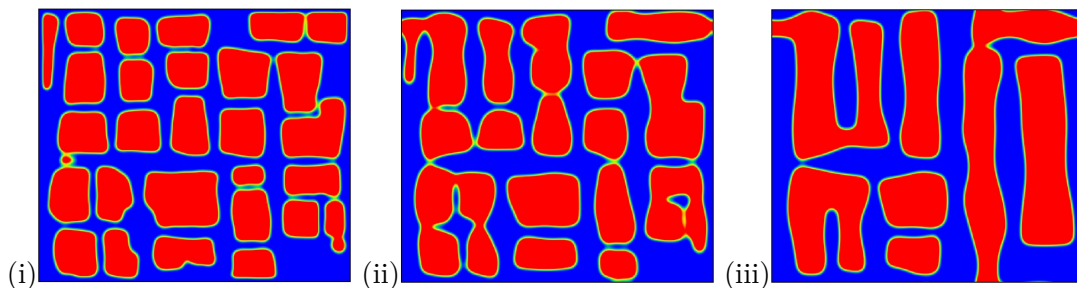


Figure 21: Morphological evolution during coarsening in an elastically anisotropic and homogeneous system ($C_{ij}^{\gamma'} = C_{ij}^{\gamma}$). (i) $t = 0$ h; (ii) $t = 24$ h; (iii) $t = 48$ h.

$\psi = (C_{ij}^{\gamma'} - C_{ij}^{\gamma}) / C_{44}^{\gamma'}$ defines the elastic inhomogeneity in an anisotropic system. The system in Fig. 22 has elastic inhomogeneity of 25%. Under high thermal exposure, the precipitates evolve from the initial cuboidal configuration to miniature raft-like structures aligned along the [100] and [010]-crystallographic directions. In case of a positive anisotropy factor, the elastically soft directions correspond to the [111], $[1\bar{1}\bar{1}]$ crystallographic directions etc [26].

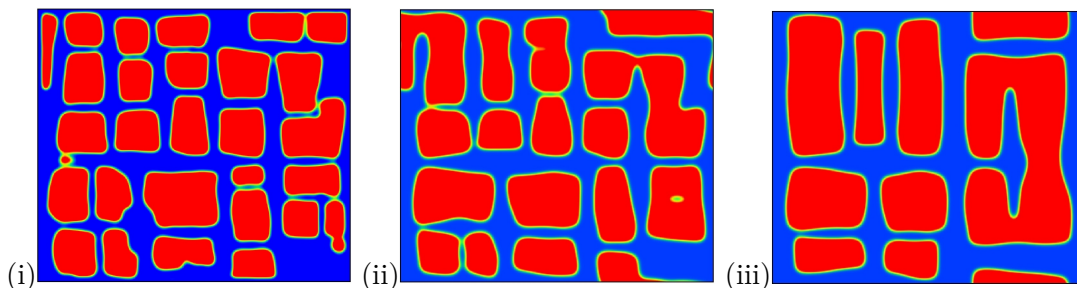


Figure 22: Morphological evolution in an elastically anisotropic and inhomogeneous system ($C_{ij}^{\gamma'} = 0.75C_{ij}^{\gamma}$). (i) $t = 0$ h; (ii) $t = 24$ h; (iii) $t = 48$ h.

The morphological evolution of a system with larger elastic inhomogeneity $\psi=50\%$ is shown in Fig. 23. In comparison to the system with a relatively smaller inhomogeneity ($\psi=25\%$) in Fig. 22, the larger inhomogeneity results in cuboidal precipitates with quite straight edges. The precipitates after 48 h exhibit interfaces perpendicular to the [100] and [010] directions and are strongly aligned along those directions. While the mechanics determine the alignment of the precipitates, the evolution of the morphology in Fig 21, 22 and 23 is achieved by two mechanisms: coalescence and ripening. In the early stages, the coarsening process is achieved by both coalescence and ripening. Coalescence of the γ' -precipitates occurs due to two reasons; the irregular shape of the precipitates and small inter-precipitate distance. Since the precipitates are irregular due to long-range elastic interactions, the diffusion fields are also irregular in shape. At a moment in the time, the diffusion fields are bound to impinge and eventually overlap which results in two neighboring γ' -precipitates merging to form one larger precipitate. In the late

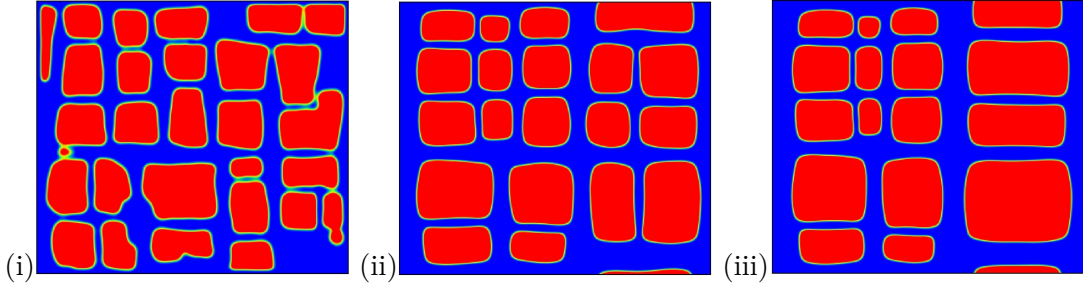


Figure 23: Morphological evolution in an elastically anisotropic and inhomogeneous system ($C'_{ij} = 0.5C_{ij}$). (i) $t = 0$ h; (ii) $t = 24$ h; (iii) $t = 48$ h.

stage as the inter-particle spacing increases, coarsening is achieved mainly by ripening. During ripening, the large precipitates with low curvature grow while the smaller ones with high curvature shrink and eventually vanish. A drop in the volume fraction between the initial and the final configurations is observed in Fig 21, 22 and 23. The reduction in the volume fraction is an influence of the strain energy density of the system. The strain energy density in the system is a function of the misfit strain. Due to changes in the morphology, the strain energy density decreases to its minimum state. Such a drop in the actually observed volume fraction as compared to the thermodynamically calculated phase fraction is theoretically expected, and relates to the elastic hysteresis effect [20, 23]. If the experimental phase fraction can be measured with sufficient accuracy to resolve this drop, this would offer an alternative way to measure the elastic energy density of a given microstructure. A significant reduction in the strain energy density occurs in the early stages at time $0 < t < 5$ h because of rapid coalescence of precipitates with their nearest neighbors due to the large precipitate density. This reduction in the strain energy density is accompanied by a rapid reduction of the precipitate volume fraction. At time $5 < t < 48$ h, reduction in the strain energy begins to slow down. The volume fraction reaches its steady-state value when the strain energy density reaches minimum state.

3.3 Conclusion

Phase-field modeling in the presence of highly anisotropic interfacial energies is addressed. In particular, we discussed two different ways of how to incorporate an orientation dependence of the interfacial energy in phase-field framework: In the first and quite common anisotropic formulation, the interface width is considered to vary with the orientation, while in the second rather new model only the interfacial energy is chosen to be anisotropic, leading to a constant interface width. Studying the quasi-one-dimensional case, where the interface is planar with a fixed orientation, we demonstrated, that both approaches can be used for quantitative modeling. However, in this respect, the vary-

ing interface formulation requires extra care due to the intrinsic kinetic anisotropy. To be able to study equilibrium shapes, efficient volume conserving Allen-Cahn dynamics were used, where through a properly chosen time dependence of a spatially constant diffusion potential growth or shrinking of the particle is prohibited. To remove the ill-posedness of the phase-field equations for high-energy orientations, which do not belong to the equilibrium shape, we employed the convexification method of Eggleston et al [16]. For both anisotropic phase-field formulations, the computed equilibrium particle shapes, both with and without sharp corners, are in excellent agreement with the analytic Wulff construction. The numerical implementation of the presented two phase-field models was developed and implemented. To achieve the necessary numerical accuracy and stability, a new and efficient explicit finite difference algorithm was developed by combining the two-step differentiation of Debierre et al. [15] with a staggered grid formulation, due to the appearance of mixed spatial derivatives in the governing equations. Furthermore, we demonstrated that this scheme provides sufficient accuracy to be able to simulate even and odd symmetries as well as high angle rotations of the underlying crystalline orientation.

We also discussed a formulation to incorporate the dependence of the total strain on the phase field. Elastic anisotropy and inhomogeneity were also introduced by postulating the cubic elastic constants to be dependent on the dimensionless phase field order parameter. The formulation was similar to Steinbach et al. [69] which assumes equal elastic stresses in the two bulk phases at the diffuse interface. The formulation resulted in an Allen-Cahn type second order equation coupled to a set of second order multi-component diffusion equations. The phase field equation and multi-component diffusion equations were solved on uniform square grids using explicit finite-difference methods. The phase field model also incorporated an Jacobi iterative algorithm for numerically solving the mechanical equilibrium of an elastically inhomogeneous system. For numerical stability, particular attention was paid to the numerical implementation of the mechanical equilibrium for the calculation of the displacement fields required to calculate the elastic driving force. The Jacobi relaxation scheme was based on the explicit finite difference with elastic variables on a staggered grid. The computed equilibrium cuboidal morphologies and $(100)_\gamma || (100)_{\gamma'}$ orientation relationship was consistent with the typical “as-heat treated” microstructures of Ni-base superalloys. The sphere to cube transition was attributed to the anisotropic growth rates of the interface along the $\langle 111 \rangle$ and $\langle 100 \rangle$ -crystallographic directions.

The simulations showed that a high interfacial energy anisotropy and elastic anisotropy can both lead to the formation of precipitates with four-fold symmetry. However, challenges can arise when both anisotropies are incorporated in a model. Including both the anisotropy of the interfacial energy in a phase field model with elastic effects requires the precise knowledge of the relative weighting of the contributions from interfacial energy and elastic anisotropies. At the moment, this is tough to quantify due to the lack of experimental data of the anisotropy of the interfacial energies in Ni-base superalloys.

4 Effect of Re on directional γ' -coarsening in commercial single crystal Ni-base superalloys: A phase-field study

Modern turbine blades which are used in the hot regions of gas turbines for the aerospace or stationary power plant application are usually manufactured as casted single crystalline parts. However, even though grain boundaries are excluded, the degradation behavior of respectively developed single crystal nickel-base superalloys is still quite complex involving a number of very different microscopic effects. One of these is the diffusion mediated coarsening of the γ' -precipitates. During creep loading along the $\langle 100 \rangle$ crystallographic orientation, the precipitates coarsen anisotropically and form plate-like structures, which are also called rafts. In the end, the rafted microstructure contains quite large and dispersed plate-like precipitates aligned either parallel (*P*-type rafts) or perpendicular (*N*-type rafts) to the loading direction [13, 39]. This is detrimental for the properties of these materials since their superior properties emanate from the size, morphology, distribution and volume fraction of the γ' -precipitates.

Generally, the modeling of coarsening of coherent phases in elastically anisotropic and inhomogeneous situations has been reviewed by Fratzl et al. [26]. For two precipitates as shown in Fig. 24 to raft along the [010]-direction, elements that are barely soluble in the γ' -precipitate (Co, Cr, Mo, Re etc) should diffuse away from the growth path while γ' -formers (Al, Ta and Ti) should diffuse into the precipitates.

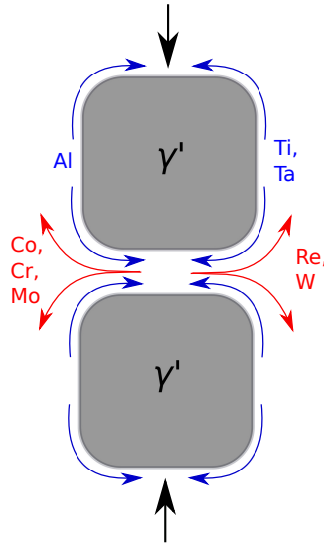


Figure 24: Schematic illustration of solute flux during interdiffusion limited coarsening under a compressive load applied along the [010]-direction in a Ni-base superalloy with a negative misfit. This illustration is based on experimental observations [32, 63].

For various reasons, technically used single crystal superalloys contain significant ad-

ditions of a whole number of different refractory elements such as Mo, W, Ta and Re. Experimental studies [32, 63, 86] have revealed that Re which is added mainly as a solid-solution strengthener significantly reduces the kinetics of coarsening as well. Rüsing et al. [63] observed the formation of Re clusters in the γ -matrix during coarsening in the Ni-Al-Ta-Re superalloy. This segregation behavior of Re plays a major role in determining the kinetics of rafting. An experimental study by Giamei et al. [32] of model alloys based on the MAR-M200 alloy concluded that for coarsening to occur, Re solutes should diffuse away from the paths of moving $\gamma - \gamma'$ interfaces. Furthermore, simulations by [72] identified that the $\gamma - \gamma'$ interface migration is controlled by atomic diffusion of Re.

So far, already a number of phase-field approaches have been used to study directional coarsening of rafting in Ni-base superalloys. For example, the rafting phenomenon has been studied using phase-field models formulated on a purely elasticity framework [33, 48]. Phase-field models with contributions from plastic strains [6, 90] have recently been developed to study rafting. Furthermore, [30] has used an elasto-viscoplastic model to study microstructure evolution under creep loading in Ni-base superalloys. All the models formulated using these various frameworks converge in identifying the lattice misfit, elastic inhomogeneity and applied load as the driving force for the directional coarsening of γ' -precipitates. The resulting microstructures obtained using the different approaches are also qualitatively similar although quantitative comparisons [89] have revealed that the kinetics differ. While it is acknowledged that mechanics play a significant role in determining the orientation of rafts, the influence of diffusion on coarsening is crucial for the understanding of the kinetics of the process [87]. Most phase-field studies, however, focus on the technically less interesting case of binary Ni-Al systems. However, a ternary phase-field model that is linked directly to commercial CALPHAD software to provide quantitative thermodynamic driving forces has been developed [82]. Our previous work [44] on non-directional coarsening in CMSX4 and CMSX6 during long-term aging revealed that slow diffusing elements play an important role in determining the nature and kinetics of coarsening.

The objective of this chapter is to study coarsening in the commercial CMSX4 and CMSX6 Ni-base superalloys in the presence of applied loading along the [010] direction. In that regard, we study the contributions from solute segregation to coarsening. Of particular interest is to understand the mechanisms by which solutes with low diffusivities e.g., Re, affect coarsening in elastically stressed Ni-based superalloys.

The phase field methodology has matured over the past two decades to address coupled multi-physics problems in material science. The basis of the investigation is a multi-component phase-field model formulated based on [44, 58]. The extended multi-component phase-field model uses inputs from CALPHAD and kinetic databases for the relative driving forces. The uniqueness of the extended multi-component model lies in that it takes into account the cross interaction of all the solutes in Ni-base superalloys, even the slowest diffusing ones. The thermodynamic formulation in the phase-field model is validated against DICTRA sharp-interface simulations as well as ThermoCalc equilibrium calculations. Additionally, to account for the misfit between two types of lattices, elastic inhomogeneity and applied loading, the model is coupled to an elastic

term based on previous works [22, 23, 44]. Furthermore, a technique to quantify the kinetics of rafting is integrated in the model. The occurrence of Ostwald ripening and coalescence during the rafting process results in vastly irregular shaped precipitates. As a result, it is quite difficult to find a global measure that quantifies the evolution of such a microstructure. The approach presented in this work uses the aspect ratio calculated on the basis of interface orientations as a quantitative measure. A unique feature of this technique is that it quantifies the coarsening of anisotropic and coalesced precipitates.

In the following section, we provide the formulation of our extended multi-component phase-field model. Studies of γ' -rafting morphological evolution and kinetics are then presented in Section 4.2. In Section 4.3, simulation results of the contribution of solute diffusivity to γ' -rafting are provided before concluding in the last section.

Parts of this chapter are published in [Acta Mater., 60:3758, 2012] and [Acta Mater., 93:60, 2015].

4.1 Model description

In this section, we present a multi-component phase-field model coupled to an elastic term that accounts for the contributions from the misfit and elastic inhomogeneity. We neglect the contributions from plastic strains. The incorporation of plastic effect is in principle possible but is extremely complicated. At least, more complicated than the incorporation of elastic heterogeneity, which has been shown to be a good approximation to the influence of the micro-mechanics on the coarsening kinetics in Ni-base superalloys [33, 48, 89].

Neglecting the anti-phase domains, a single non-conserved field variable $\phi(\vec{x}, t)$ is introduced to describe the coherent γ/γ' -two phase microstructure. To distinguish between the two distinct bulk phases, fixed values are assigned to represent them, 1 for the γ -phase and 0 for the γ' -phase. Additionally, it is postulated that $\phi(\vec{x}, t)$ varies smoothly within an interface of a finite width. We neglect the appearance of anti-phase boundaries, which form between different translational variants of the ordered γ' -phase. The emphasis of the current model is to find a quantitative description of the coarsening kinetics of the γ' -phase. The main assumption of the model is that the kinetics of coarsening is limited by the complex interdiffusion kinetics of multiple components in the γ -phase. Strictly speaking, this model is for the analysis of coarsening kinetics in superalloys with low γ' -fractions. The full set of equations solved for the studies in the following have been derived and validated in Chapters 2 and 3. The main model equations are Eq. (106)-(165). In the following, we specify the full set of thermophysical and elastic parameters for the numerical studies in Sections 4.2 and 4.3.

4.1.1 Determination and rescaling of input parameters

In this section, the input data that is used for the calibration of the model is used. We perform simulations on the CMSX4 and CMSX6 commercial superalloys with a

compositions presented in Table. 3.

	Al	Co	Cr	Mo	Re	Ta	Ti	W	Ni
CMSX4	5.6	9.6	6.4	0.6	3.0	6.5	1.0	6.4	base
CMSX6	4.8	5.0	9.8	3.0	-	2.0	4.7	-	base

Table 3: The composition of the superalloys under study.

The input parameters used in the simulations can be divided into three groups. First, there are thermodynamic parameters, which depend on the alloy system: the equilibrium phase compositions $c_i^{p,eq}$, equilibrium free energies $f_{ch}^{p,eq}$ and the equilibrium diffusion potential μ_i^{eq} . The equilibrium data are calculated using the ThermoCalc software. The kinetic data includes the interdiffusion matrix D_{ij}^p and the thermodynamic factors X_{ij}^p . The diffusion matrix terms are calculated by a subroutine of the DICTRA software. The last set of parameters are the the elastic parameters, these include the elastic constants C_{ijkl}^p and the lattice misfit ε^{00} .

For the construction of the parabolic free energies

$$f_{ch}^p = \frac{1}{2} \sum_i X_i^p (c_i^p - A_i^p)^2 + B^p, \quad (166)$$

the phase dependent parameters X_i^p , A_i^p and B_i^p are required. The first derivative of of the free energy, Eq. (166) with respect to the concentration of species i yields the diffusion potential

$$\mu_i = \frac{\partial f_{ch}^p(c_i, \phi)}{\partial c_i} = X_{ii}^p (c_i^{p,eq} - A_i^p), \quad (167)$$

in the phase p . When two interconnected phases are in chemical equilibrium with each other, the diffusion potentials need to be continuous at the common interface, that is

$$\mu_i = \left. \frac{\partial f^\gamma}{\partial c_i} \right|_{eq} = \left. \frac{\partial f^{\gamma'}}{\partial c_i} \right|_{eq}. \quad (168)$$

The equilibrium $c_i^{p,eq}$ and $f_{ch}^{p,eq}(c_i^{p,eq})$ are found by the common tangent construction. The equilibrium values are extracted from ThermoCalc/TTNi8 database for a specific alloy composition at a specific temperature.

To determine the values of A_i^p and B^p from the equilibrium concentrations $c_i^{p,eq}$, the equilibrium free energy densities $f_{ch}^{p,eq}(c_i^{p,eq})$, Eq. (166) is used. This expression is inverted to yields the values of the free energies

$$B^p = f^{p,eq} - \frac{1}{2} \frac{(\mu_i^{eq})^2}{X_{ii}^p}. \quad (169)$$

This expression is inverted to obtain the concentrations

$$A_i^p = c_i^{p,eq} + \frac{\mu_i^{eq}}{X_{ii}^p}. \quad (170)$$

The obtained parameters are then fitted into thermodynamic grand-potential functional (94) to complete the description of the thermodynamic driving force for phase transformation.

	Al	Co	Cr	Mo	Re	Ta	Ti	W
X_i	18.9	11.0	16.6	17.6	35.3	16.7	10.6	16.8
μ_i^{eq}	-0.18	-0.08	-0.07	-0.1	-0.09	-1.07	-0.19	-0.074
$c_i^{\gamma,eq}$	0.0306	0.1412	0.1214	0.0108	0.0619	0.0168	0.0033	0.0856
$c_i^{\gamma',eq}$	0.0757	0.0613	0.0196	0.0023	0.0044	0.1022	0.0152	0.0473
$f^{\gamma,eq}$	-0.070909							
$f^{\gamma',eq}$	-0.071758							

Table 4: Thermodynamic factors X_i/X_0 for CMSX4 (Scaling factor $X_0 = 10^6$ J/mol-at), equilibrium diffusion potentials μ_i^{eq}/μ_0 (Scaling factor $\mu_0 = 10^6$ J/mol), equilibrium Gibbs free energies $f_{ch}^{p,eq}/f_0$ (Scaling factor $f_0 = 10^6$ J/mol) at 1273.15 K and equilibrium phase concentrations $c_i^{p,eq}$ (in wt.%).

	Al	Co	Cr	Mo	Ta	Ti
X_i	22.0	21.1	10.8	35.4	53.4	22.9
μ_i^{eq}	-0.19	-0.089	-0.06	-0.08	-0.18	-0.16
$c_i^{\gamma,eq}$	0.0253	0.0706	0.1895	0.0603	0.0077	0.0014
$c_i^{\gamma',eq}$	0.0653	0.0342	0.028	0.0068	0.0294	0.0723
$f^{\gamma,eq}$	-0.080767					
$f^{\gamma',eq}$	-0.098317					

Table 5: Thermodynamic factors X_i/X_0 for CMSX6 (Scaling factor $X_0 = 10^6$ J/mol-at), equilibrium diffusion potentials μ_i^{eq}/μ_0 (Scaling factor $\mu_0 = 10^6$ J/mol), equilibrium Gibbs free energies $f_{ch}^{p,eq}/f_0$ (Scaling factor $f_0 = 10^6$ J/mol) at 1273.15 K and equilibrium phase concentrations $c_i^{p,eq}$ (in wt.%).

The interdiffusion coefficients used in our work are calculated from the diffusion mobility database MobNi1 using the DICTRA software. The interdiffusion matrices for

CMSX4 and CMSX6 at 1273.15 K are presented in Table. 6 and 7, respectively. Data for diffusion in the ordered γ' -precipitate phase is not readily available. However, it is generally known that diffusion in the γ' -precipitate is several orders of magnitude slower than in the γ -matrix. In our simulations, for simplicity, we adopt a symmetric model with equal diffusion matrices for both phases $D_{ij}^\gamma = D_{ij}^{\gamma'}$.

	Al	Co	Cr	Mo	Re	Ta	Ti	W
Al	5.98	-1.03	0.155	-0.132	-0.132	0.0222	0.0777	-0.165
Co	0.78	0.575	-0.255	-0.0262	-0.0026	0.0289	0.0323	-0.0363
Cr	0.18	-0.066	1.01	-0.0122	-0.0556	0.0477	0.100	-0.0642
Mo	1.72	-0.046	-0.054	0.657	-0.049	0.0305	0.0098	-0.0593
Re	1.30	-0.035	-0.011	-0.0381	-0.0056	0.0305	0.0716	-0.0218
Ta	2.40	-0.280	1.16	-0.0009	-0.0882	0.716	0.0131	-0.106
Ti	2.31	-0.810	1.03	0.0148	-0.101	0.0536	1.8	0.119
W	2.62	-0.776	0.560	-0.0089	-0.0575	0.0394	0.112	0.0004

Table 6: The scaled diffusion matrix D_{ij}^γ for CMSX4 at 1273.15 K obtained from DIC-TRA using MobNi1 database (Scaling factor $D_s = 10^{-14}\text{m}^2\text{s}^{-1}$).

	Al	Co	Cr	Mo	Ta	Ti
Al	0.396	-0.0320	0.0644	0.00188	0.00165	0.0367
Co	-0.0320	0.0989	-0.0296	-0.00249	0.00149	0.0155
Cr	0.0644	-0.0291	0.12	-0.00245	0.00240	0.0436
Mo	0.00188	-0.0186	0.00732	0.0744	0.00162	0.0422
Ta	0.00165	0.00762	0.194	0.000698,	0.0710	0.0583
Ti	0.0367	-0.0294	0.160	0.00138	0.00270	0.247

Table 7: The scaled diffusion matrix $D_{ij}^{\gamma'}$ for CMSX6 at 1273.15 K obtained from DIC-TRA using MobNi1 database (Scaling factor $D_s = 10^{-14}\text{m}^2\text{s}^{-1}$).

Another important quantity is the mobility matrix M_{ij} . This can be deduced from the diffusion matrix through the following relation,

$$\mathbf{D} = \mathbf{M}\mathbf{X}, \quad (171)$$

where \mathbf{X} is the thermodynamic factor matrix. Furthermore, for the construction of the parabolic free energies of the two phases Eq. (166) The parameters X_{ii}^{ph} , A_i^{ph} and B_i^{ph} are required. The thermodynamic factors are evaluated deduced directly from DICTRA as

$$X_{ij}^{ph} = \left(\frac{\partial^2 f^{ph}}{\partial c_i \partial c_j} \right)_{T,p,c_k} = \partial \mu_i / \partial c_j. \quad (172)$$

The thermodynamic factors are evaluated as $\mu_i(c_1, c_2, c_3, \dots, c_n)$ with n being the number

of species in the multi-component system. Although a thermodynamic factor matrix is obtained, the major terms X_{ii} for the superalloy under study are several orders of magnitude larger than the cross terms X_{ij} . For simplicity, we therefore adopt only the major terms and assume that they are equal $X_{ii}^\gamma = X_{ii}^{\gamma'} = X_i$. The values of X_i for CMSX4 and CMSX6 alloys are presented in Table. 4 and 5, respectively.

The experimental values of the misfit ε^{00} and the elastic constants for both phases are required. The cubic elastic constants used in the simulation are shown in Table 8. A value of -0.14% is adopted from Pyczak et al. [61] as the misfit for both alloys. The degree of elastic anisotropy, $\xi_A = 2C_{44}/C_{11} - C_{12} = 2.92$, is positive, which shall result in P -type rafting for a compressive external strain, i.e. the elongated γ' -precipitates are preferentially aligned parallel to loading direction [33].

	C_{11}	C_{12}	C_{44}
γ	$215.5/\eta$	$162/\eta$	$77.6/\eta$
γ'	$222.7/\eta$	$164.2/\eta$	$85.6/\eta$

Table 8: Elastic constants (in GPa) used in the simulations [65]. The rescaling parameter $\eta = 85.6$ GPa.

In the simulations, the interfacial energy is assumed isotropic, with a value of 80mJ/m^2 for CMSX4 and 120mJ/m^2 for CMSX6. The surface energy is estimated by the classic nearest-neighbor broken-bond concept known as the sharp interface approximation [66]. The kinetic coefficient K is related to the interdiffusion coefficients obtained from DICTRA. Since we study interdiffusion-limited phase transformations, the kinetic coefficient is chosen to be larger than any term in the diffusion matrix. The kinetic coefficient is chosen to be $1.2 \times 10^{-14}\text{m}^2\text{s}^{-1}$ for CMSX4 and $0.8 \times 10^{-14}\text{m}^2\text{s}^{-1}$ for CMSX6.

4.2 Multiple γ' -precipitate rafting

We now employ the validated model extension to study microstructure evolution beyond the capability of ThermoCalc and DICTRA. To that end, we investigate interdiffusion-limited γ' -rafting in elastically inhomogeneous superalloys. We perform simulations on two quite different multi-component alloys indicating that the model allows to vary the alloying composition without further restrictions.

In this section, we study the characteristics of coarsening in negatively misfitting CMSX4 and CMSX6 superalloys with contributions from elastic heterogeneity and applied loading. A technique to quantify the kinetics of coarsening in microstructures with anisotropic precipitates is then introduced.

4.2.1 Characteristics of γ' -rafting in elastically inhomogeneous superalloys

Using the presented multi-component model, morphological evolution at 1273.15 K in negatively misfitting CMSX4 and CMSX6 is now investigated. A compressive strain

($\varepsilon_a = -0.2\%$) is applied along the y -direction [010] for 28 h. It is observed that the γ' -precipitates evolve from the quasi-cuboids in Fig. 20 (c) to plate-like structures, which are elongated in the y -direction, as shown in Fig. 25. As expected, for the case of a compressive strain applied to a negatively misfitting alloy, the γ' -rafts are oriented parallel to the loading direction i.e. P -type rafting is observed, which is consistent with previous predictions on the rafting orientation [33, 55, 64]. Rafting is then achieved by the mechanism of interdiffusion-limited coarsening or Ostwald ripening. Fig. 25 shows the as-rafterd CMSX6 and CMSX4 microstructures obtained after 28 h of exposure at 1273.15 K under a compressive strain $\varepsilon_a = -0.2\%$. It is observed that in the early stages of the coarsening simulations, when many small precipitates exist, coalesce with the neighboring precipitates the [010] direction is a frequent event. In the later stages of the inter-precipitate spacing becomes larger, and particle coalescence events become much more rare. At this stage, the larger precipitates grow and elongate at the expense of the smaller or shorter precipitates, respectively, whereas the rate of mutual growth and shrinkage is limited by diffusional transport in the γ -channels. We confirmed that the total amount of solute of all elements is conserved in full numerical precision during the whole coarsening simulation.

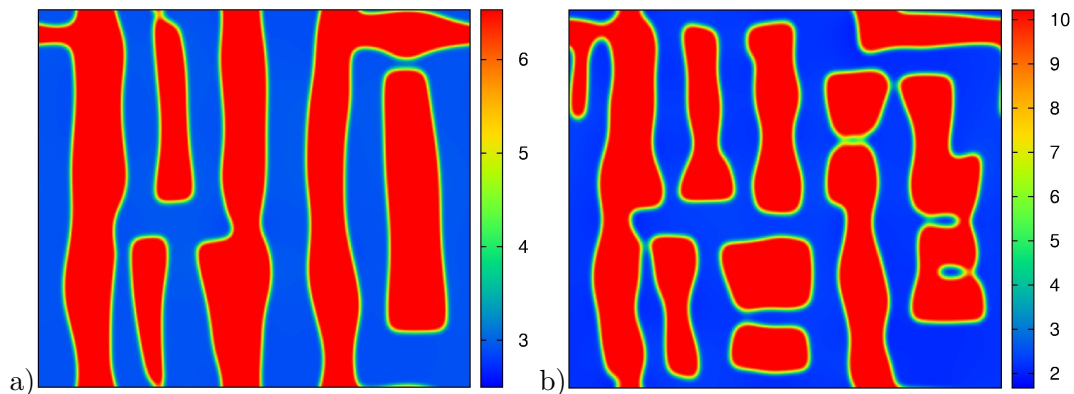


Figure 25: Concentration field (wt.%) of Ta in (a) CMSX6; (b) CMSX4 after 28 h of aging under a compressive strain ($\varepsilon_a = -0.2\%$) along the [010] direction. In the Re-free CMSX6, most particles are elongated up to a mean length that exceeds the simulation domain while in the Re-containing CMSX4, the particles are generally shorter and some are even cuboidal. The domain size is $3.5\mu\text{m} \times 3.0\mu\text{m}$.

Also our simulations confirm the general picture that slow diffusing elements, particularly Re, play a major role in determining the kinetics of anisotropic γ' -coarsening. Fig. 25 shows that after the simulation of 28 h of heat exposure at 1273.15 K, the whole coarsening process in the Re-containing CMSX4-alloy is much less developed as compared to the coarsening process in the Re-free CMSX6-alloy: particles in the CMSX4 simulation are generally shorter or even still cuboidal, while in the simulation of coarsening in the Re-free CMSX6-alloy the majority of particles has been elongated up to

a mean length that exceeds already the simulation domain. Moreover, the simulated microstructure of CMSX4 in Fig. 25 (b) reveals the formation of quite large Re accumulation zones in the γ -matrix. This observation is in agreement with the experimental findings by Rüsing et al. [63], who observed the presence of Re accumulation zones during heat treatment of the Ni-Al-Ta-Re superalloy. The presence of the Re in the γ -matrix inhibits the elongation of a precipitate. Furthermore, we observe in our simulations that for the γ' -precipitate to grow along a certain orientation, Re should diffuse away from the path of the advancing $\gamma - \gamma'$ interface.

The evolution of the γ' -precipitate volume fraction during high temperature exposure of CMSX4 and CMSX6 in the absence and presence of external strains is shown in Fig. 28 (a). A drop in the volume fraction between the initial and the coarsened configurations is observed. The reduction in the volume fraction is an influence of the strain energy density of the system. The strain energy density in the system is a function of the misfit strain and applied strain. Since we use the same initial microstructure, the total strain energy at $t = 0$ is the same for the two alloys. However, due to different changes in the morphology at $t > 0$ h, the strain energy density decreases to different minimum states. Such a drop in the actually observed volume fraction as compared to the thermodynamically calculated phase fraction is theoretically expected, and relates to the elastic hysteresis effect [23, 20]. If the experimental phase fraction can be measured with

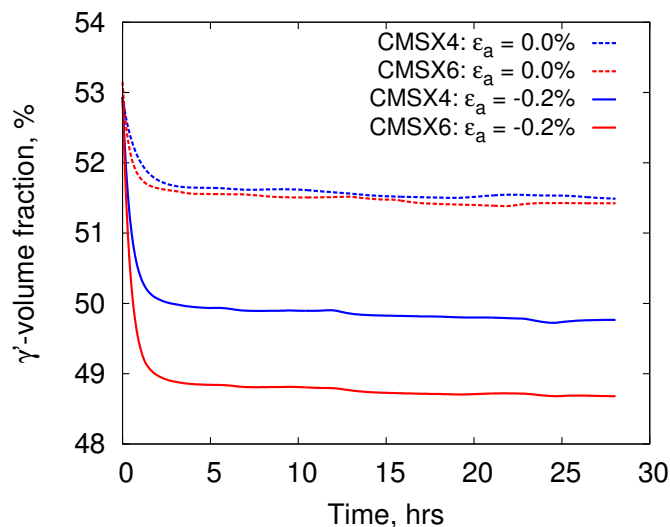


Figure 26: Time evolution of the γ' -volume fraction during coarsening under no applied strain ($\epsilon_a = 0.0\%$) and under compressive strain ($\epsilon_a = -0.2\%$). The volume fraction reaches its steady-state value when the strain energy density reaches its minimum state.

sufficient accuracy to resolve this drop, this would offer an alternative way to measure the elastic energy density of a given microstructure. It can be seen that the decrease of the γ' -precipitate volume fraction is slower in CMSX4 than in CMSX6. The steady-state volume fraction of CMSX4 of around 50% and CMSX6 is around 49%. In both alloys,

a significant reduction in the strain energy density occurs in the initial stages $t < 5$ h due to rapid coalescence of precipitates with their nearest neighbors along the energy minimizing [010] direction. This reduction in the strain energy density is accompanied by a rapid reduction of the precipitate volume fraction. At time $5 < t < 20$ h, reduction in the strain energy begins to slow down. At this stage, the translation of the precipitates along the [010] direction occurs. The volume fraction reaches its steady-state value when the strain energy density reaches its minimum state. However, rafting continues in order to satisfy mass balance in the system. In the steady-state regime of the rafting process, the constant volume fraction means that the lengthening of precipitates in the [010] direction occurs simultaneously with the shrinkage of precipitates along the [100] direction. Although a drop in the volume fraction during evolution under the applied compressive strain is expected, the degree of change is perhaps overestimated due to the relatively large applied strain used in the simulation. To further elucidate the influence of strain energy density on the γ' -precipitate volume fraction, we compare the rafting simulations with our previous work on non-directional coarsening [54], when the reduction of the strain energy density is much lower due to shape preservation. It is observed that the γ' -precipitate volume fraction changes from 54.2% to 51.7% in CMSX4 to around 51.6% in CMSX6.

4.2.2 Quantification of anisotropic γ' -coarsening kinetics

Typically, the kinetics of coarsening is quantitatively characterized by some measure that is based on the mean particle radius. Such a one-sidedness is not surprising, since the majority of theoretical discussions as well as respective model developments start from spherically shaped particles [26] and is therefore naturally centered around the case of isotropic coarsening. However, while the mean particle radius is certainly a meaningful quantity for the characterization of coarsening kinetics in the isotropic or near isotropic case (i.e. basically spherical particles), we argue that this is not the case of strongly anisotropic coarsening. Therefore, for the further characterization of the morphological evolution during coarsening in Ni-base superalloys, we would like to propose here a numerical measure to quantify the kinetics of anisotropic coarsening of γ/γ' -microstructures. The measure is based on the diffuse interface description as it results from the phase-field method. To quantitatively characterize the anisotropic development during rafting in a microstructure with multiple precipitates, we define a non-dimensionless aspect ratio

$$AR = \frac{L_{[010]}}{L_{[100]}}, \quad (173)$$

where $L_{[010]}$ denotes that fraction of the total length of the γ/γ' -phase boundary, which is oriented predominately parallel to the [010]-crystallographic plane. The information about the *a priori* unknown interface orientation is related to the gradient of the phase

field and here we use the unit normal vector as defined [24]

$$\vec{n} \equiv \frac{\vec{\nabla}\phi}{|\vec{\nabla}\phi|}. \quad (174)$$

The phase-boundary length L_o of interfaces having an orientation which corresponds to the crystallographic unit vector \vec{o} , is calculated as follows

$$L_o = \frac{1}{2\xi} \int \{h(\phi)h(1-\phi)\Theta(\vec{n} \cdot \vec{o} - \cos(\vartheta))\} dV, \quad (175)$$

where ξ is the interface width and $\Theta(x)$ is a step-function which has the value 1 if $x \leq 0$ and 0 if $x > 0$, Finally, ϑ quantifies the uncertainty angle in the determination of the interface orientation. A value of $\vartheta = \pi/4$ is used in the simulations. The angle is chosen such that as many as possible interfaces corresponding to the crystallographic unit vector \vec{o} are included in the calculation. Note that the application of the interpolation function $h(\phi) = \phi^2(3-2\phi)$ in Eq. (175) provides a focus on the inner parts of the diffuse interface.

Using the presented measure, we can now quantify the kinetics of anisotropic coarsening of multiple precipitate. As a proof-of-accuracy of the quantitative measure of the aspect ratio, we compare respective results to the time evolution of the aspect ratio of a single precipitate, located in the center of the simulation domain (the precise configuration is shown in Fig. 29).

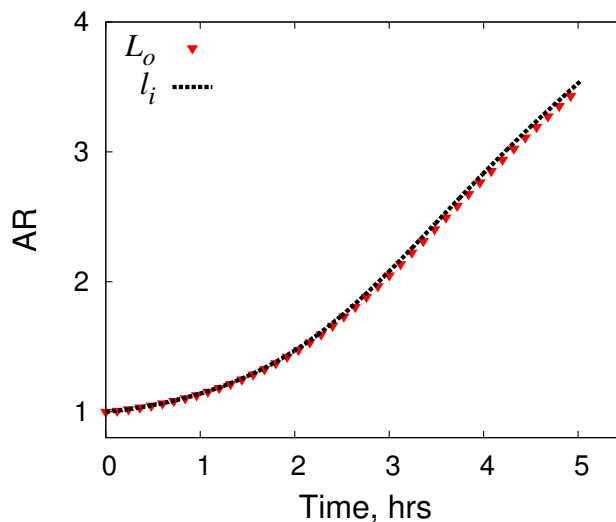


Figure 27: Comparison of the aspect ratio AR (in blue) calculated using Eq. (175) against the reference aspect ratio (in red) calculated using line integrals over the phase field (See Eq. (176)).

In the simple case of elongation of a single particle, the aspect ratio is naturally given by the ratio $R_c = l_x/l_y$, where the lengths l_i of the particle in the i -th direction ($i = x, y$)

is calculated in a straight forward way by means of a respective line integral over the phase field in the middle of the simulation domain, i.e.,

$$l_i = \int_0^{L_i} (1 - \phi(\mathbf{x}, t))|_{x_j=L_j/2} dx_i, \quad (176)$$

with $i \neq j$. The plot in Fig. 27 shows the comparison of the calculation of the single particle aspect ratio using Eq. (175) and the reference aspect ratio as it results from the line integrals using Eq. (176). The small deviation may result from the fact that, upon the choice of an uncertainty angle ϑ to be significantly smaller than $\pi/4$, finite fractions of the interface are excluded from the consideration in Eq. (176).

Using the presented quantitative measure, we can now quantify the kinetics of anisotropic coarsening of a microstructure with multiple precipitates as in Fig. 25. The plot in Fig. 28 shows the evolution of the aspect ratio during multiple particle rafting at 1273.15 K. The precipitates in CMSX6 elongate much faster than in CMSX4. The aspect ratio of γ' -precipitates in CMSX6 after 28 h is 8.5 and 7.2 in CMSX4. The unsteady nature of these two curves is attributed to the events of precipitate coalescence.

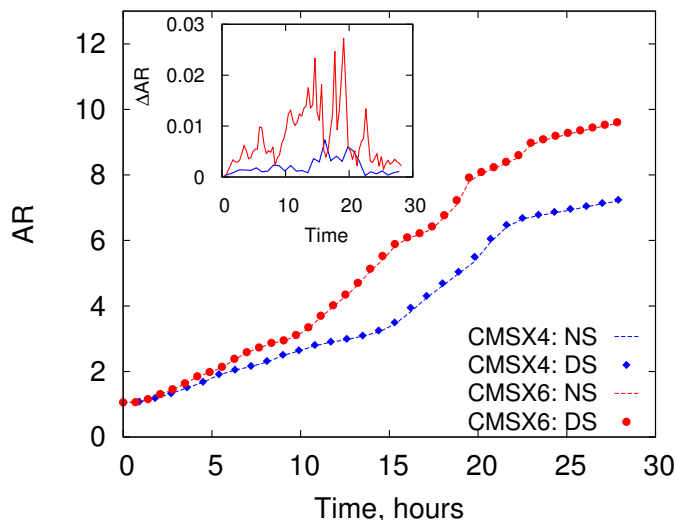


Figure 28: Time evolution of the aspect ratio AR for two different systems: NS of size $409 \times 357 \Delta x$ with interface width $\xi = 5 \Delta x$ and DS of double size $818 \times 714 \Delta x$ with interface width $\xi = 2.5 \Delta x$. The precipitates in CMSX6 elongate much faster than in CMSX4. The unsteady nature of these two curves is attributed to the presence of precipitate coalescence. Insert: The plot of $\Delta AR = (AR_{DS} - AR_{NS}) / R_{NS}$ shows that the calculation of AR is not greatly influenced by changes of the interface width used in the phase-field model.

In order to quantitatively identify the impact of the artificially chosen large interface width in the phase-field model, we perform comparable simulations, which differs only in the choice of phase field widths. The first system, denoted by NS, is the previously

defined one of size $409 \times 357 \Delta x$ with interface width $\xi = 5 \Delta x$. The second system denoted by DS is of double size $818 \times 714 \Delta x$ with interface width $\xi = 2.5 \Delta x$. The simulations with the different system configurations reveal that the precipitate aspect ratio does not change by much with a change in the interface width used in the phase-field model.

4.3 Isolated γ' -precipitate rafting

To further elucidate the rate-limiting influence of Re on γ' -rafting, we study the evolution of a single γ' -precipitate in an elastically inhomogeneous γ -matrix at 1273.15 K. For the single precipitate simulations, a square domain of size $351 \times 351 \Delta x$ is used. To obtain the initial quasi-cuboidal shape, a spherical γ' -precipitate is placed in the γ -matrix at the center of the simulation domain and then prerelaxed without external loading until the quasi-cuboidal shape with a volume fraction of 56% is obtained. The sphere-to-cube shape change is a result of the dominant effect of coherency strain energy on the precipitate morphology [41].

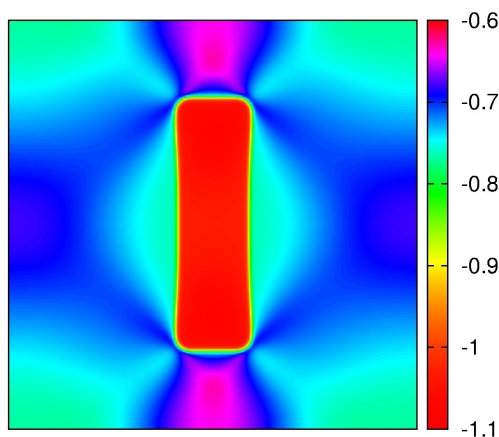


Figure 29: Dimensionless elastic driving force field $\partial\omega_{el}/\partial h$; the applied strain changes the four-fold symmetry of the precipitate to two-fold symmetry. Due to the compressive strain, the elastic driving force is highest along the $[010]$ direction which results in the elongation of the precipitate along this direction.

To trigger the rafting process, a compressive strain is applied to the cuboidal precipitate. Fig. 29 shows the morphology of an isolated γ' -precipitate formed under a compressive strain ($\varepsilon_a = -0.2\%$) applied along the $[010]$ direction. The applied strain changes the four-fold symmetry of the precipitate to two-fold symmetry with the precipitate elongating along the $[010]$ direction. Fig. 29 shows the dimensionless elastic driving force field for the precipitate under the compressive strain. The elastic driving force is highest along the $[010]$ direction and this favors the elongation of the precipitate along

this direction.

In the next subsection, we analyze the contributions from solute diffusivity to rafting in CMSX4 and CMSX6 superalloys. In subsection 4.3.2, we then identify the mechanism by which the refractory element Re affects rafting.

4.3.1 γ' -rafting kinetics with contributions from solute diffusivity

In this subsection, we present a sensitivity study to show the phase-field model's capacity to determine the relative contribution of each solute to the morphological evolution and kinetics. This study can be understood as a sensitivity analysis to quantify the impact of uncertainties in the diffusion coefficients. The sensitivity study is also meant as a first step to show the capacity of the multi-component phase-field model to handle changed diffusivities as well as in the second step changed compositions. The second step would then result in true simulation based alloy design and optimization.

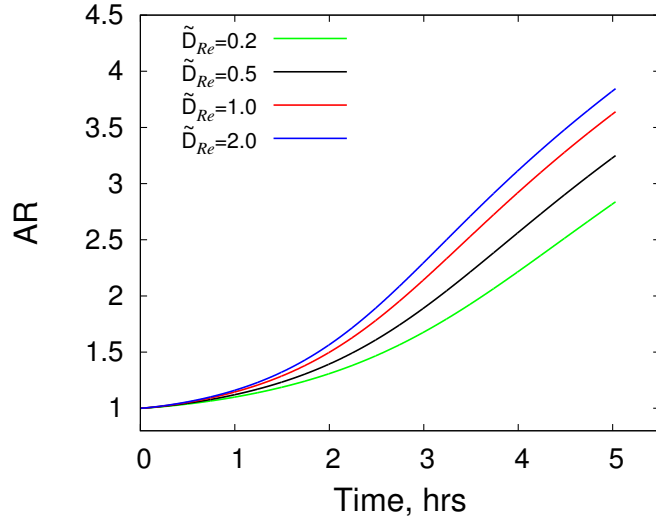


Figure 30: Time evolution of the aspect ratio AR of an isolated γ' -precipitate for different choices of Re diffusivity \tilde{D}_{Re} during P -type rafting under an applied compressive strain ($\varepsilon_a = -0.2\%$) along the $[010]$ direction. The control diffusivity is $\tilde{D}_{Re} = 1.0$ which corresponds to the diffusion matrix given in Table 6. A reduction in the diffusivity of Re results in a slower elongation.

To analyze the contribution of solute diffusivity to rafting, a study of the time evolution of the aspect ratio AR of a single γ' -precipitate for different strengths of diffusivity of a solute i is done. For this study, the control diffusivity is $\tilde{D}_i = 1.0$, which corresponds to the diffusion matrix given in Tables 6 and 7. For a species i , three other simulations are done with diffusivity scaling $\tilde{D}_i = 0.2$, $\tilde{D}_i = 0.5$ and $\tilde{D}_i = 2.0$. This is done by including

a diffusivity scaling term \tilde{D}_i to the diffusion equation Eq. (115) which becomes

$$\frac{\partial \mu_i}{\partial t} = \tilde{D}_i \sum_j (D_{ij} \nabla^2 \mu_j) - \frac{\Delta A_i}{\chi_i} \frac{\partial h}{\partial \phi} \frac{\partial \phi}{\partial t}. \quad (177)$$

This allows for the scaling of the major and cross terms for species i in the diffusion matrices in Table 6 and 7 while holding the rest of the interdiffusion coefficients constant.

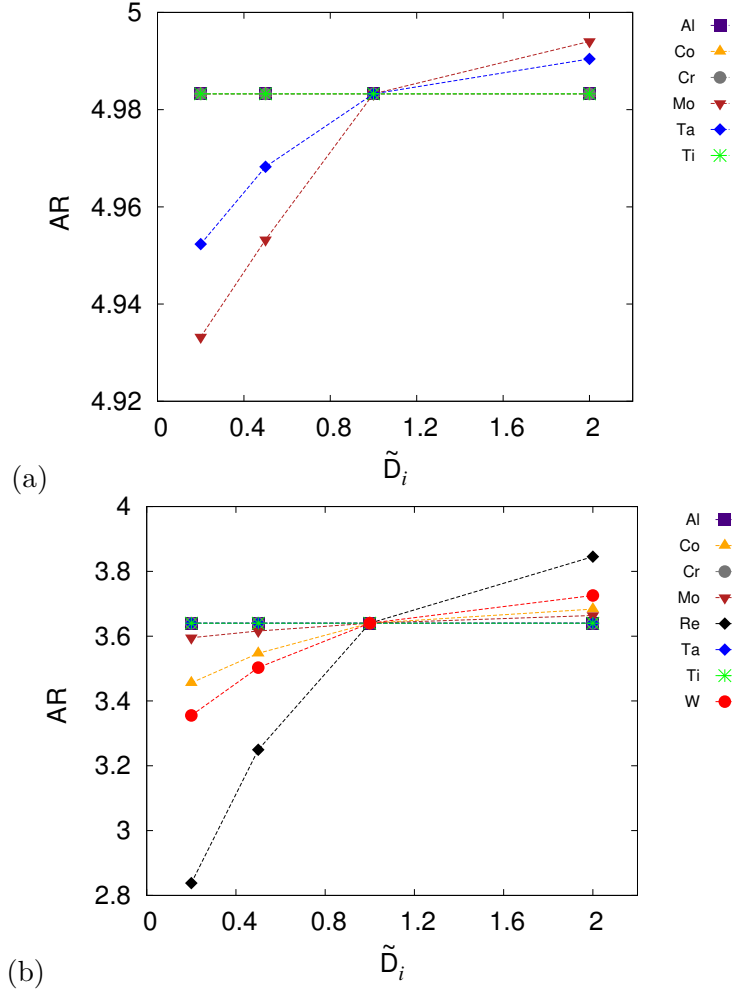


Figure 31: Aspect ratios AR of an isolated γ' -precipitate after 5 h of exposure at a temperature of 1273.15 K under compression ($\varepsilon_a = -0.2\%$) as a function of the diffusivity \tilde{D}_i of a species (a) CMSX6; only Ta and Mo has some very small effect on rafting, (b) CMSX4; Re greatly affects the kinetics of rafting in CMSX4 while Co, Mo and W contribute to a smaller extent.

For instance, the diffusivity scaling of $\tilde{D}_{Al} = 0.2$ rescales the first row (major and cross terms for Al) in Table 6. The evolution of AR with time as a function of the diffusivity

of solute i is compared with the control aspect ratio (diffusivity strength of $\tilde{D}_i = 1.0$). The stronger (weaker) the deviation of the aspect ratio from the control aspect ratio, the stronger (weaker) the influence of solute i on rafting. The influence of Re diffusivity on rafting is shown in Fig. 30. Here, the evolution of the aspect ratio AR of an isolated γ' -precipitate under a compressive strain is plotted as a function of exposure time for different Re diffusivity \tilde{D}_{Re} . Such a study is done for each element in the two alloys.

The aspect ratios after 5 h are plotted in Fig. 31 as a function of the diffusivity \tilde{D}_i for the two superalloys. For CMSX6, Fig. 31 (a), the diffusivity of Ta and Mo has some effect on the elongation of the precipitate although the effect is very much negligible. The control aspect ratio in CMSX6 is about 4.98. A reduction of the diffusivity of Ta by scaling with $\tilde{D}_{Ta} = 0.2$ results in an aspect ratio of about 4.93. For CMSX4, Fig. 31 (b), the influence of alloying elements on the nature of rafting is much more prominent.

While Co, Mo and W to a smaller extent affect rafting, it is the presence of Re that greatly affect the nature and kinetics of the morphological evolution in CMSX4. The control aspect ratio in CMSX4 is 4.65. Reducing the diffusivity of Re greatly reduces the aspect ratio of the precipitate. For example, reducing the diffusivity of Re by scaling with $\tilde{D}_{Re} = 0.2$ results in an aspect ratio of about 2.8, which is a massive reduction indeed. From these plots, it is clear that Re influences rafting to a greater extent.

4.3.2 Rate-limiting effect of Re

In this subsection, we now elucidate the mechanism by which Re limits rafting in Ni-base superalloys. Just before the application of an external strain to the initial cuboidal precipitate, the diffusion potential of Re in both the horizontal (parallel to the (100) plane) and vertical γ -channels (parallel to the (010) plane) are equal. Such an equilibrium state implies that no transport of Re solutes takes place. Application of a compressive strain along the [010] direction to the initial quasi-cuboidal microstructure distorts the diffusion potential of Re in the γ -channels. Consequently, a region of high Re diffusion potential is formed in the horizontal channels in the vicinity of the γ - γ' interfaces and a region of low diffusion potential of Re is formed in the vertical γ -matrix. The resulting diffusion potential gradient drives the flux of Re solute atoms within the γ -matrix. As the precipitate elongates along the [010] direction, Re solutes are rejected by the advancing γ - γ' interfaces. The rejection occurs because Re solutes are barely soluble in the γ' -precipitate. The rejected Re solutes diffuse in the γ -matrix from the path of advancing γ - γ' interfaces to the vestige of the shrinking of precipitate. The formation of Re accumulation zones in front of advancing γ - γ' interfaces is also observed. Fig. 32 (a) shows the distribution of Re in a rafted microstructure. The Re accumulation zones are also observed during non-directionally coarsened microstructures (Fig. 32 (b)), which results in the precipitates almost keeping their cuboidal morphology. The formation of Re accumulation zones can be attributed to its low diffusivity. Various reasons have been given in literature for the low diffusivity of Re; the work [32, 63, 73] attribute the low diffusivity to its heavy atom while [27] attribute the low diffusivity of Re to the strong electronic Ni-Re bonding. As the accumulation of Re solutes in front of advancing $\gamma - \gamma'$

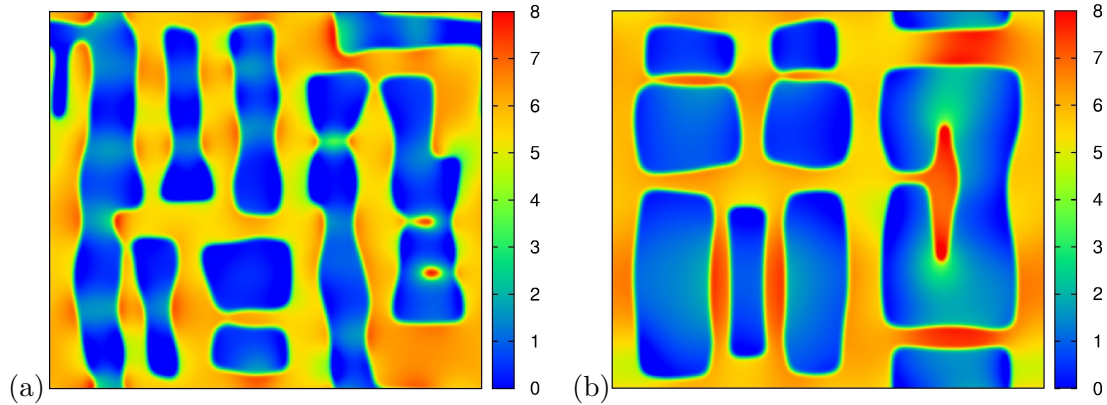


Figure 32: Concentration field of Re (in wt.%) during (a) rafting under an applied load, (b) non-directional coarsened coarsening. Re solutes which are not readily soluble within the γ' -precipitate are transported away from the elongation path. Owing to its low diffusivity, Re accumulation zones are formed and increase with time in front of advancing γ - γ' -interfaces. This effect slows down the elongation of the precipitate.

interfaces increases, elongation kinetics of the γ' -precipitate along the $[010]$ direction is significantly reduced. For the precipitate to elongate further, Re solutes should diffuse away from the elongation path. The rate-limiting influence of Re on the migration of $\gamma - \gamma'$ interface can be attributed a number of factors;

- Re is barely soluble in the γ' -precipitate and segregates to the γ -matrix. During the coarsening simulations, expulsion of the minute amount of Re present in the γ' -precipitate is observed. One can say that during coarsening in elastically stressed alloys, the interface composition does not obey the local equilibrium assumption.
- its low diffusivity results in the formation of Re accumulation zones in the path of migrating interface. Different reasons have been given in literature for the low diffusivity of Re. Some authors [32, 63, 73] attribute the low diffusivity to its heavy atom. Fu et al. [27] attribute the low diffusivity of Re to the strong electronic Ni-Re bonding.

For W and Mo, we also observed the formation of minor accumulation zones in front of advancing $\gamma - \gamma'$ interfaces. This behavior is not seen for the rest of the solutes since their diffusivities and solubilities in the γ' -precipitate are relatively high. These two effects result in the formation of accumulation zones just in front of the growing interface. Additionally, the formation of accumulation zones in front of the interface implies that the heavy Re atoms should simultaneously diffuse from the path of the the moving interface in the direction shown by the arrows in Fig. 29 and this costs energy which further reduces the driving force for interface migration. An opposite mechanical

force exerted by the Re solute atoms in addition to the natural friction of interface migration causes a reduction in the driving force for interface migration. Owing to a lower driving force, it becomes difficult for the interface to migrate further. The pile-up of Re solutes in front of the interface increases with time. As a result, the elongation of the γ' precipitate along the y -direction is significantly reduced.

4.4 Conclusion

A quantitative multi-component phase-field model was applied for the simulation of γ' -coarsening during the aging of Ni-based superalloys. With a view to realistically capturing the complex nature of interdiffusion, all input values for the phase-field simulations were calculated by CALPHAD based tools, which are able to predict these properties within their database definition limits. The model was applied to study the morphological evolution in the two commercially available CMSX4 and CMSX6 superalloys. Furthermore, a numerical method to quantify the kinetics of γ' -coarsening were developed. This method can be used to quantify rafting in a microstructure with anisotropic precipitates of random distribution. The method was used to quantify coarsening during microstructural evolution in the presence of a uniaxial strain applied along a cubic $\langle 100 \rangle$ direction. Phase-field simulation results of non-directional coarsening were compared with experimental predictions. The phase field simulations were qualitatively in agreement with experimental observations.

The simulations revealed that the coarsening process is considerably slower in CMSX4 than in CMSX6. The simulations provided an insight at the rate-limiting influence of some alloying elements. It was revealed that the rate-limiting influence of certain elements increases depending on their diffusion dynamics in relation to the interfacial kinetics. It was observed that Re, plays a major role in reducing the rate of coarsening. The simulations deduce that Re additions in CMSX4 reduce coarsening by keeping the γ' -precipitates in their interfacial energy minimizing quasi-cuboidal configuration. Re also reduces the growth and elongation of γ' -precipitate by reducing the driving force for interface migration. This is caused by the accumulation of Re in the path of the growing front. As the precipitate elongates with time, the amount of Re in growth path increases - due to low diffusivity and its low solubility in the precipitate. An opposite mechanical force exerted by the Re solute atoms in addition to the natural friction of interface migration leads to a reduction in the driving force for interface motion and a subsequent reduction of the coarsening process. This supports the experimental studies of [32, 63, 86] who observed a dominant influence of Re on coarsening in single crystal superalloys. In CMSX6, the situation is different; there a combined influence of a number of elements on the kinetics - with Ta and Mo being the rather influential elements. However, the influence of Ta and Mo is considerably less as compared to that of Re. This study showed that elements e.g., Re, W, Mo and Ta have a rate-limiting influence on coarsening and thus can be used for the fine-tuning of alloy microstructures.

5 Phase-field study of anisotropic γ' -coarsening kinetics in Ni-base superalloys with varying Re *and* Ru contents

The typical microstructure of single crystalline Ni-base cast alloys consists of cuboidal γ' -precipitates coherently embedded in a continuous γ -matrix (Ni). The extraordinary thermo-mechanical properties of these Ni-base superalloys largely depends on the morphology, distribution, size and volume fraction of the γ' precipitates. Under long-time exposure to a high external temperature, the γ' -precipitates coarsen in order to reduce the total amount of γ - γ' interfaces. The respective driving force is called the Gibbs-Thompson effect or capillarity. However, any change of the γ - γ' microstructure involves first order phase transformation processes between the two phases and leads to a release or a capture of material. The release or capture of material results in finite chemical deviations from the two phase γ - γ' equilibrium state, which need to be transported diffusively away from the interface through the system. The two main opposing driving forces determine the coarsening-evolution: the Gibbs-Thompson effect on the one hand and a local non-equilibrium diffusion potential resulting from a local non-equilibrium chemical composition on the other hand. Consequently, as the whole process evolves, larger precipitates grow at the expense of smaller ones, leading to an increase of the mean particle size and a complimentary decrease of the total interfacial area. Since the diffusive transport of material away from or towards to the interface is rather slow but still a necessary requirement for the overall process to evolve, the kinetics of coarsening is said to be diffusion-limited.

The kinetics of multi-particle coarsening is quantitatively described by the well known LSW-theory of Ostwald ripening which was originally developed by Lifshitz and Slyosov [49] as well as Wagner [75]. Even though the theory was based on the relatively strict assumption of spherically shaped particles with an infinitesimally small volume fraction, it turned out to be surprisingly successful, especially with regard to the application to γ' -coarsening in Ni-based superalloys [2, 3, 74]. However, it is known that the elastic interactions arising from a difference of lattice spacing between two coherently connected phases can have a strong influence on the coarsening behavior of alloys. In the present case of γ' -precipitates embedded into the γ -matrix, both phases are of face-centered-cubic (*fcc*) crystallographic structure but with different lattice parameters which depend on the overall alloying composition in a highly non-trivial way. There have been a lot of attempts to extend the LSW-theory to also account for the elastic effects from the coherency strains, which have been reviewed by Fratzl et al. [26]. In the discussion on the LSW-theory, we shall focus on the so-called coarsening exponent which characterizes the principle functional dependence of the mean particle radius R and the coarsening time t . The classical LSW-theory of diffusion-controlled coarsening in binary alloys predicts that the mean particle radius grows linearly in time, i.e. $R^3 \propto t$. The classical coarsening exponent of three has been confirmed experimentally as well as in simulation work, when the elastic effects are comparably small (see for instance the studies on ternary Ni-Al-Mo alloys [77, 18]). On the other hand, there is a number of experimental and simulation

studies which suggest that the coarsening exponent changes when the elastic effects become more important [26].

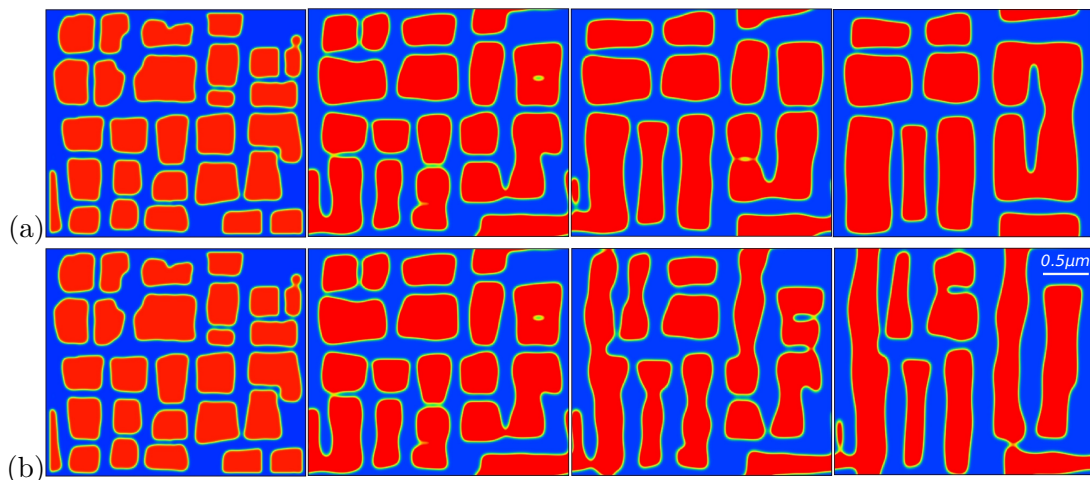
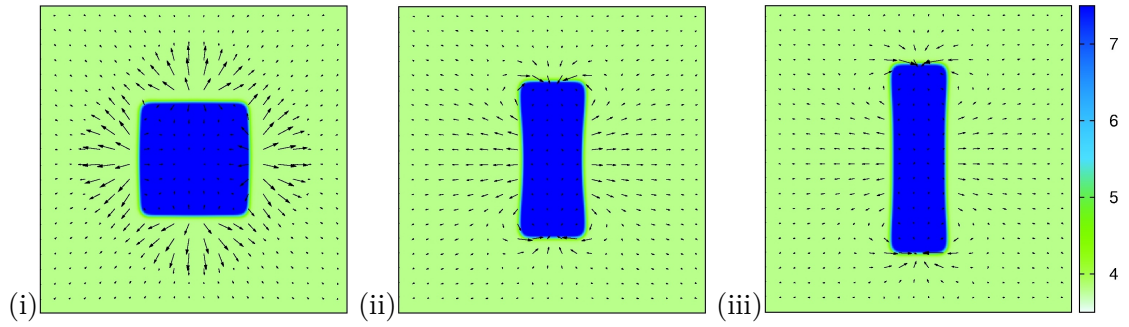
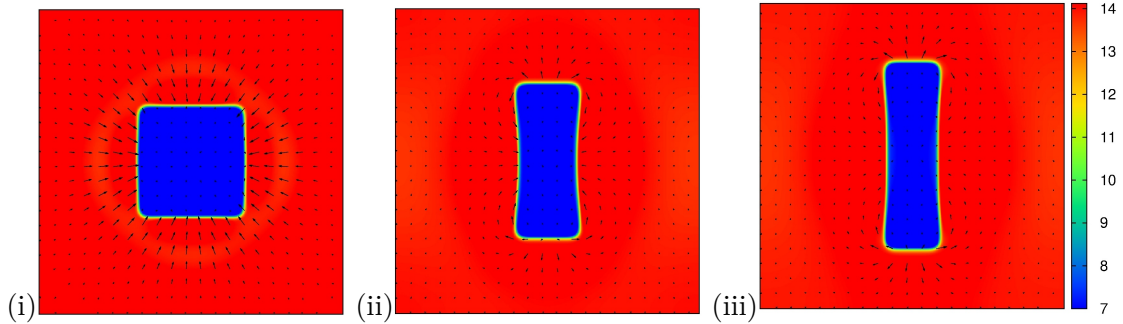


Figure 33: Coarsening at 1273.15 K in CMSX4 with a misfit of -0.14% at $t = 0, 14, 28, 42$ h. The size of the simulation domain is $3.5 \times 3.0 \mu\text{m}^2$. (a) Non-directional coarsening with contributions from misfit and elastic inhomogeneity, (b) Rafting with contributions from misfit, elastic inhomogeneity, and compressive strain $\varepsilon_a = -0.2\%$ applied parallel the (010)-crystallographic direction.

In this work, we employ phase field simulations to study the temporal evolution of γ' -coarsening in Ni-base superalloys. The phase field method is an ideal tool for the simulation of microstructure evolution in complex binary and multi-component alloys. Various aspects relevant in materials science ranging from the initial solidification to late-stage solid-state transformations have been successfully addressed, so far, using phase-field modeling techniques [1, 17, 80]. The major advantage of the method is given by its great flexibility of modeling, which allows to address even complex systems involving several different physical mechanisms at the same time. In the present case, where anisotropic γ' -coarsening in technologically relevant Ni-based superalloys is considered, we have to account for (at least) elastic contributions from the misfit between the two phases and as well as for the complex thermodynamics and kinetics of the phase-separating multi-component alloy. A respective realization of such a phase-field model then provides the physically based microstructure evolution starting from a basically arbitrary initial system state, as demonstrated in Fig 33 (a) for the case without mechanical loads and in Fig 33 (b) for the case with an externally applied strain. Another example is simulated temporal evolution of a single particle of cubic shape to a plate-like precipitate under the influence of the externally applied stress, as shown in Fig 34. In both cases, the simulated kinetics of coarsening turn out to be limited by the diffusional transport of the nine different explicitly considered chemical components, namely: Ni, Al, Ta, Ti, Co, Cr, W, Ru and Re.



(a) Al diffuses to the advancing γ - γ' interfaces which allows the γ' -precipitate to elongate further along the [010]-direction. The precipitate shrinks along the [100]-direction to free a supplement of Al.



(b) Co diffuses from the path of the advancing γ - γ' interfaces to the vestige of the shrinking precipitate in the vertical γ -channels.

Figure 34: Cube \rightarrow plate-like transformation of an isolated γ -precipitate during coarsening in CMSX4 under a compressive strain ($\varepsilon_a = -0.2\%$) applied parallel the (010)-crystallographic plane. The applied strain distorts the diffusion potentials in the vertical and horizontal γ -channels creating diffusion potential gradients which drive solute flux. The colour scheme represents the concentration in wt.%. The arrows represent the flux of solutes.

The reason why such a large amount of alloying elements is explicitly resolved is related to the fact that we aim to develop our phase-field model to serve as a useful tool for future alloy design. In order to demonstrate the idea, we also perform a virtual experiment using phase-field simulation studies to determine the influence of a varying alloy composition on the cubic \rightarrow plate-like transition as a simplified configuration of rafting. More specifically, we perform here a simulation study considering 12 different virtual superalloys, where the rhenium (Re) *and* ruthenium (Ru) contents are systematically varied. The decision to jointly vary the Re and Ru additions, is motivated by the discussion in materials science of whether Ru can act as a possible Re replacement-candidate, as suggested by Caron [12] as well as Heckl et al. [36, 35], who focused on various aspects concerning the solidification behavior as well as the influence on the formation of topologically close packed phases. Here, the phase-field based simulation studies are used as a cheap and fast tool for the development of alloys with regard to the γ' -coarsening behavior.

The present work aims to demonstrate the principle feasibility as well as the value of our recently developed phase-field model [54] with the particular focus on two different materials science aspects with regard to the γ' -coarsening behavior in Ni-based superalloys:

- The identification of the coarsening exponent with and without elastic effects in binary as well as multi-component alloys.
- The identification of the influence of variations of Re and Ru contents on the kinetics of anisotropic γ' -coarsening.

The main model equations are already given in Eq. (106)-(165). In Section 5.2.2, we present an analytic derivation of the LSW-theory for multi-component alloys without elastic effects. In Section 5.2.3, we use phase-field simulations to validate the theoretical extension of the LSW-theory and to determine the temporal law for multi-component Ni-base superalloys with elastic effects. Results of a virtual experiment to determine the influence of Re+Ru additions on γ' -morphology during coarsening are then presented in Section 5.3 after which concluding remarks are given.

This chapter is published in [Adv. Eng. Mater., DOI: 10.1002/adem.201500168, 2015].

5.1 Simulation parameters

We investigate the coarsening kinetics in 12 model Ni-base superalloys adopted from Heckl et al. [36]. The model Ni-base superalloys are derived from CMSX4 with a chemistry of 12.58Al, 9.26Co, 7.58Cr, 0.38Mo, 0.98Re, 2.18Ta, 1.98W and bal. Ni in at.%. The compositions of the alloys are systematically varied by stepwise additions of 0 to 2 at.% Re and 0 to 4 at.%Ru at the expense of the base element Ni. The compositions of the 12 alloy and their designation is given in Table 9.

	AL	CO	CR	MO	RE	RU	TI	W	Ni
Alloy00	13.50	9.00	6.00	0.60	-	-	2.20	2.00	base
Alloy01	13.50	9.00	6.00	0.60	-	1.00	2.20	2.00	base
Alloy02	13.50	9.00	6.00	0.60	-	2.00	2.20	2.00	base
Alloy10	13.50	9.00	6.00	0.60	1.00	-	2.20	2.00	base
Alloy11	13.50	9.00	6.00	0.60	1.00	1.00	2.20	2.00	base
Alloy12	13.50	9.00	6.00	0.60	1.00	2.00	2.20	2.00	base
Alloy13	13.50	9.00	6.00	0.60	1.00	3.00	2.20	2.00	base
Alloy14	13.50	9.00	6.00	0.60	1.00	4.00	2.20	2.00	base
Alloy20	13.50	9.00	6.00	0.60	2.00	-	2.20	2.00	base
Alloy21	13.50	9.00	6.00	0.60	2.00	1.00	2.20	2.00	base
Alloy22	13.50	9.00	6.00	0.60	2.00	2.00	2.20	2.00	base
Alloy23	13.50	9.00	6.00	0.60	2.00	3.00	2.20	2.00	base
CMSX4	12.58	9.26	7.58	0.38	0.98	-	2.18	1.98	base

Table 9: Composition of model Ni-base superalloys in wt.%. The first digit in the model superalloy designation is the Re content whilst the second is Ru content [36].

The input parameters used in the simulations are divided into three groups.

First, there are thermodynamic parameters, these include the equilibrium phase compositions $c_i^{p,eq}$, equilibrium free energies $f_{ch}^{p,eq}$ and the equilibrium diffusion potential μ_i^{eq} . The second group is the kinetic data includes the interdiffusion matrix D_{ij}^p and the thermodynamic factors X_{ij}^p . The last set of parameters are the material parameters which include the interface energy σ and the elastic constants C_{ijkl}^p and the lattice misfit ε^{00} .

5.1.1 Thermodynamic parameters

The thermodynamic parameters depend on the alloy compositions. The equilibrium parameters are calculated for the given composition at a temperature of 1273.15 K using the ThermoCalc/TTNi8 database. In Tables 10-12, we list the unscaled the equilibrium phase compositions, the equilibrium diffusion potentials and the equilibrium free energies, respectively. How to retrieve the simulation parameters from from these listed parameters as well as their rescaling is described in detail in subsection 4.1.1.

(gamma)	AL	CO	CR	MO	TI	W	RE	RU
Alloy00	1.34428E-01	9.60631E-02	1.33088E-01	1.79535E-02	1.81888E-02	1.57569E-02	-	-
Alloy01	1.33963E-01	9.51599E-02	1.33472E-01	1.80613E-02	1.82733E-02	1.55628E-02	-	1.60785E-02
Alloy02	1.33543E-01	9.42882E-02	1.33810E-01	1.81560E-02	1.83794E-02	1.53869E-02	-	3.16937E-02
Alloy10	1.25231E-01	9.52798E-02	1.33304E-01	2.04780E-02	1.58464E-02	1.59205E-02	6.26199E-02	-
Alloy11	1.24850E-01	9.45174E-02	1.33956E-01	2.05322E-02	1.59512E-02	1.57390E-02	6.13976E-02	1.59790E-02
Alloy12	1.24513E-01	9.37787E-02	1.34560E-01	2.05708E-02	1.60765E-02	1.55749E-02	6.01811E-02	3.15410E-02
Alloy13	1.24221E-01	9.30601E-02	1.35110E-01	2.05928E-02	1.62223E-02	1.54269E-02	5.89684E-02	4.66923E-02
Alloy14	1.35000E-01	9.00000E-02	6.00000E-02	6.00000E-03	2.20000E-02	2.00000E-02	1.00000E-02	4.00000E-02
Alloy20	1.14243E-01	9.53922E-02	1.35392E-01	2.38552E-02	1.30895E-02	1.62603E-02	1.30207E-01	-
Alloy21	1.14182E-01	9.47058E-02	1.36091E-01	2.36799E-02	1.32835E-02	1.60925E-02	1.26751E-01	1.60367E-02
Alloy22	1.17519E-01	9.29280E-02	1.32131E-01	2.18718E-02	1.45541E-02	1.59349E-02	1.11970E-01	3.08834E-02
Alloy23	1.20569E-01	9.12626E-02	1.27932E-01	2.02333E-02	1.57897E-02	1.58183E-02	9.91654E-02	4.46168E-02
(gamma_prime)	AL	CO	CR	MO	TI	W	RE	RU
Alloy00	1.35000E-01	9.00000E-02	6.00000E-02	6.00000E-03	2.20000E-02	2.00000E-02	-	-
Alloy01	1.35000E-01	9.00000E-02	6.00000E-02	6.00000E-03	2.20000E-02	2.00000E-02	-	1.00000E-02
Alloy02	1.35000E-01	9.00000E-02	6.00000E-02	6.00000E-03	2.20000E-02	2.00000E-02	7.56797E-12	2.00000E-02
Alloy10	1.35000E-01	9.00000E-02	6.00000E-02	6.00000E-03	2.20000E-02	2.00000E-02	1.00000E-02	-
Alloy11	1.35000E-01	9.00000E-02	6.00000E-02	6.00000E-03	2.20000E-02	2.00000E-02	1.00000E-02	1.00000E-02
Alloy12	1.35000E-01	9.00000E-02	6.00000E-02	6.00000E-03	2.20000E-02	2.00000E-02	1.00000E-02	2.00000E-02
Alloy13	1.35000E-01	9.00000E-02	6.00000E-02	6.00000E-03	2.20000E-02	2.00000E-02	1.00000E-02	3.00000E-02
Alloy14	1.35000E-01	9.00000E-02	6.00000E-02	6.00000E-03	2.20000E-02	2.00000E-02	1.00000E-02	4.00000E-02
Alloy20	1.35000E-01	9.00000E-02	6.00000E-02	6.00000E-03	2.20000E-02	2.00000E-02	2.00000E-02	-
Alloy21	1.35025E-01	8.99943E-02	5.99083E-02	5.97869E-03	2.20105E-02	2.00047E-02	1.98713E-02	9.99272E-03
Alloy22	1.35303E-01	8.99493E-02	5.87515E-02	5.72528E-03	2.21289E-02	2.00704E-02	1.84081E-02	1.98116E-02
Alloy23	1.35535E-01	8.99532E-02	5.74828E-02	5.47260E-03	2.22301E-02	2.01549E-02	1.70666E-02	2.94584E-02

Table 10: The equilibrium phase compositions (in J/mol) at 1273.15 K.

(mu)	AL	CO	CR	MO	TI	W	RE	RU
Alloy00	-1.38146E+05	-9.06974E+04	-5.58409E+04	-8.14222E+04	-1.54119E+05	-7.52800E+04	-	-
Alloy01	-1.37443E+05	-9.09188E+04	-5.59596E+04	-8.13615E+04	-1.53690E+05	-7.49898E+04	-3.06791E+05	-1.02881E+05
Alloy02	-1.36743E+05	-9.11404E+04	-5.60807E+04	-8.13126E+04	-1.53267E+05	-7.47064E+04	-3.07133E+05	-9.59069E+04
Alloy10	-1.37102E+05	-9.09696E+04	-5.59291E+04	-8.13460E+04	-1.53142E+05	-7.49756E+04	-8.33505E+04	-3.25809E+05
Alloy11	-1.36401E+05	-9.11927E+04	-5.60523E+04	-8.13010E+04	-1.52720E+05	-7.46956E+04	-8.37160E+04	-1.03301E+05
Alloy12	-1.35702E+05	-9.14159E+04	-5.61778E+04	-8.12677E+04	-1.52304E+05	-7.44226E+04	-8.40836E+04	-9.63305E+04
Alloy13	-1.35006E+05	-9.16389E+04	-5.63055E+04	-8.12463E+04	-1.51895E+05	-7.41565E+04	-8.44534E+04	-9.24061E+04
Alloy14	-1.34314E+05	-9.18619E+04	-5.64352E+04	-8.12366E+04	-1.51492E+05	-7.38973E+04	-8.48252E+04	-8.97298E+04
Alloy20	-1.36059E+05	-9.12448E+04	-5.60236E+04	-8.12901E+04	-1.52172E+05	-7.46859E+04	-7.63696E+04	-3.23358E+05
Alloy21	-1.35364E+05	-9.14651E+04	-5.61617E+04	-8.12930E+04	-1.51763E+05	-7.44113E+04	-7.68005E+04	-1.03730E+05
Alloy22	-1.34741E+05	-9.16278E+04	-5.64278E+04	-8.16701E+04	-1.51425E+05	-7.40923E+04	-7.78914E+04	-9.67896E+04
Alloy23	-1.34159E+05	-9.17728E+04	-5.67156E+04	-8.20793E+04	-1.51134E+05	-7.37853E+04	-7.89660E+04	-9.28802E+04

Table 11: The equilibrium diffusion potentials (in J/mol) at 1273.15 K.

(f)	gamma	gamma_prime
Alloy00	-9.87924E+04	-1.02068E+05
Alloy01	-9.87924E+04	-1.02068E+05
Alloy02	-9.35611E+04	-7.55325E+04
Alloy10	-9.35611E+04	-7.55325E+04
Alloy11	-9.35611E+04	-7.55325E+04
Alloy12	-9.35611E+04	-7.55325E+04
Alloy13	-9.35611E+04	-7.55325E+04
Alloy14	-9.35611E+04	-7.55325E+04
Alloy20	-9.35611E+04	-7.55325E+04
Alloy21	-9.35611E+04	-7.55325E+04
Alloy22	-9.35611E+04	-7.55325E+04
Alloy23	-9.35611E+04	-7.55325E+04

Table 12: The equilibrium Gibbs free energies (in J/mol) at 1273.15 K.

5.1.2 Kinetic parameters

The kinetic parameters are also composition. The diffusion matrix terms and thermodynamic factor matrices are calculated at 1273.15 K by a subroutine of the DICTRA software using the MobNi1 database. Below, we give the unscaled elastic constants used in the simulations. The rescaling of the kinetic parameters for phase field simulations is described in detail in subsection 4.1.1.

```

.....Alloy00.....
Dkj (reduced n=NI)
k / j AL      CO      CR      MO      TI      W
AL +6.32852E-13 +1.02164E-13 +2.40336E-13 +2.09433E-13 +3.54375E-13 +3.55691E-13
CO -7.33257E-15 +7.79785E-14 -9.18017E-15 -6.00499E-15 +7.43582E-15 -6.26626E-15
CR +4.8421E-15 +2.93332E-16 +1.06998E-13 +1.28738E-15 +9.21418E-15 +6.0417E-15
MO +1.10753E-14 +1.1033E-15 +2.88717E-15 +9.67198E-14 +2.54059E-14 +8.73745E-15
TI +4.56747E-14 +1.88958E-14 +4.91424E-14 +4.49985E-14 +2.30165E-13 +5.86673E-14
W -4.25895E-26 +3.78092E-26 +6.48909E-26 +3.5495E-26 +1.18831E-25 +1.11649E-14

.....Alloy01.....
Dkj (reduced n=NI)
k / j AL      CO      CR      MO      RU      TI      W
AL +6.52561E-13 +1.14248E-13 +2.62537E-13 +2.21964E-13 -1.11234E-13 +3.68891E-13 +3.53555E-13
CO -5.6076E-15 +8.28981E-14 +9.95081E-16 -1.35041E-15 -1.21941E-13 +1.10518E-14 -1.168E-14
CR +5.08068E-15 +7.84997E-16 +1.09118E-13 +1.78625E-15 -1.28432E-14 +9.67983E-15 +5.49433E-15
MO +5.202E-15 +1.32035E-15 +3.01658E-15 +9.36192E-14 -1.93807E-14 +1.20159E-14 +2.96958E-15
RU -2.80508E-14 -7.06013E-14 -1.51115E-13 -6.63145E-14 +1.73972E-12 -5.74778E-14 +7.70499E-14
TI +4.67208E-14 +2.05431E-14 +5.2932E-14 +4.69001E-14 -3.18122E-14 +2.33922E-13 +5.70576E-14
W -2.88174E-26 +1.06353E-25 +2.04972E-25 +9.83239E-26 -1.61951E-24 +1.63379E-25 +1.11649E-14

.....Alloy02.....
Dkj (reduced n=NI)
k / j AL      CO      CR      MO      RU      TI      W
AL +6.62501E-13 +1.1565E-13 +2.64599E-13 +2.23099E-13 -1.10219E-13 +3.69049E-13 +3.55553E-13
CO -6.78429E-15 +8.2527E-14 +2.29549E-16 -2.06348E-15 -1.22238E-13 +1.0051E-14 -1.23739E-14
CR +4.99179E-15 +7.39499E-16 +1.1016E-13 +1.72686E-15 -1.28799E-14 +9.63166E-15 +5.41845E-15
MO +1.00039E-14 +2.42405E-15 +5.76265E-15 +9.72466E-14 -3.89357E-14 +2.37736E-14 +5.57289E-15
RU -3.45025E-14 -7.27119E-14 -1.5396E-13 -7.10869E-14 +1.73794E-12 -6.98458E-14 +6.89378E-14
TI +4.63819E-14 +2.03283E-14 +5.2903E-14 +4.67795E-14 -3.21334E-14 +2.35383E-13 +5.69013E-14
W -3.85298E-26 +1.02963E-25 +1.97386E-25 +9.38463E-26 -1.62258E-24 +1.64616E-25 +1.11649E-14

```

Table 13: Diffusion coefficients (m^2s^{-1}) at 1273.15 K of 12 model Ni-base superalloys.

.....Alloy10.....								
Dkj (reduced n=NI)								
k / j	AL	CO	CR	MO	RE	TI	W	
AL	+6.36616E-13	+1.00833E-13	+2.35708E-13	+2.11358E-13	+1.53401E-13	+3.45619E-13	+3.50326E-13	
CO	-1.68017E-14	+7.3548E-14	-1.61495E-14	-1.19962E-14	-7.52519E-15	-2.61995E-15	-1.44598E-14	
CR	+3.92298E-15	-1.7247E-16	+1.07307E-13	+7.54713E-16	+1.02674E-15	+8.24999E-15	+5.19731E-15	
MO	+3.51063E-15	-5.18705E-17	+3.29496E-16	+9.20638E-14	-6.77427E-15	+9.8934E-15	+2.69494E-15	
RE	-9.03298E-15	-1.06081E-15	-3.78807E-15	-4.05445E-15	+2.80537E-15	-5.44177E-15	-3.2397E-15	
TI	+4.2845E-14	+1.74029E-14	+4.70338E-14	+4.3766E-14	+3.34418E-14	+2.28669E-13	+5.61375E-14	
W	-1.83819E-25	-2.73527E-26	-3.41531E-26	-7.35493E-26	+3.80678E-26	-1.88806E-26	+1.11649E-14	
.....Alloy11.....								
Dkj (reduced n=NI)								
k / j	AL	CO	CR	MO	RE	RU	TI	W
AL	+6.59187E-13	+1.14227E-13	+2.61469E-13	+2.2241E-13	+1.72004E-13	-1.11053E-13	+3.64992E-13	+3.5197E-13
CO	-1.09421E-14	+8.05382E-14	-2.68172E-15	-5.19355E-15	+2.1619E-15	-1.23871E-13	+5.89682E-15	-1.59635E-14
CR	+4.57557E-15	+5.34266E-16	+1.09822E-13	+1.4395E-15	+1.98458E-15	-1.30544E-14	+9.21164E-15	+5.05044E-15
MO	+4.33562E-15	+9.86225E-16	+2.48064E-15	+9.30414E-14	-5.19346E-15	-1.96347E-14	+1.11882E-14	+2.26104E-15
RE	-3.17773E-15	+6.84364E-16	+4.64927E-16	-5.26767E-16	+4.33649E-15	-1.96817E-14	-1.09306E-15	-1.64599E-15
RU	-3.23833E-14	-7.24464E-14	-1.54774E-13	-6.35549E-14	-1.08136E-13	+1.73866E-12	-6.86849E-14	+6.92748E-14
TI	+4.51181E-14	+1.96982E-14	+5.19277E-14	+4.60329E-14	+3.67373E-14	-3.26392E-14	+2.34034E-13	+5.57604E-14
W	-1.03737E-25	+7.2826E-26	+1.54424E-25	+3.59107E-26	+1.76644E-25	-1.64776E-24	+1.0085E-25	+1.11649E-14
.....Alloy12.....								
Dkj (reduced n=NI)								
k / j	AL	CO	CR	MO	RE	RU	TI	W
AL	+6.66737E-13	+1.14724E-13	+2.61119E-13	+2.23801E-13	+1.73163E-13	-1.10442E-13	+3.61972E-13	+3.51297E-13
CO	-1.57185E-14	+7.84982E-14	-5.88435E-15	-8.4451E-15	-2.36752E-16	-1.25534E-13	+1.3574E-15	-1.96575E-14
CR	+4.12481E-15	+3.15499E-16	+1.10583E-13	+1.15286E-15	+1.76389E-15	-1.32393E-14	+8.8029E-15	+4.66387E-15
MO	+3.56175E-15	+7.05755E-16	+2.02338E-15	+9.25618E-14	-5.441E-15	-1.98443E-14	+1.04633E-14	+1.65102E-15
RE	-7.84549E-15	+7.11992E-16	-3.29466E-17	-2.30329E-15	+5.2283E-15	-3.9906E-14	-3.33726E-15	-4.37411E-15
RU	-3.66516E-14	-7.41313E-14	-1.58245E-13	-6.06953E-14	-1.09642E-13	+1.73773E-12	-7.95846E-14	+6.18329E-14
TI	+4.36901E-14	+1.89557E-14	+5.10755E-14	+4.53641E-14	+3.60982E-14	-3.33834E-14	+2.34354E-13	+5.46536E-14
W	-1.70413E-25	+4.38687E-26	+1.10655E-25	-1.78161E-26	+1.4212E-25	-1.67223E-24	+4.70773E-26	+1.11649E-14
.....Alloy13.....								
Dkj (reduced n=NI)								
k / j	AL	CO	CR	MO	RE	RU	TI	W
AL	+6.75087E-13	+1.15659E-13	+2.61374E-13	+2.25968E-13	+1.74842E-13	-1.09467E-13	+3.59703E-13	+3.514E-13
CO	-2.00174E-14	+7.67261E-14	-8.68806E-15	-1.12149E-13	-2.32765E-15	-1.26974E-13	-2.6519E-15	-2.28535E-14
CR	+3.72029E-15	+1.23481E-16	+1.11394E-13	+9.1531E-16	+1.57411E-15	-1.34024E-14	+8.44598E-15	+4.32552E-15
MO	+2.86699E-15	+4.70233E-16	+1.6323E-15	+9.2162E-14	-5.63723E-15	-2.00167E-14	+9.82709E-15	+1.12431E-15
RE	-1.37583E-14	+2.15177E-16	-1.29656E-15	-5.07886E-15	+5.48545E-15	-6.05637E-14	-6.476E-15	-7.94353E-15
RU	-4.08816E-14	-7.56756E-14	-1.61554E-13	-5.77761E-14	-1.10996E-13	+1.73691E-12	-9.02074E-14	+5.46909E-14
TI	+4.24094E-14	+1.82981E-14	+5.03503E-14	+4.48569E-14	+3.55598E-14	-3.40596E-14	+2.34852E-13	+5.37066E-14
W	-2.30013E-25	+1.87282E-26	+7.25827E-26	-6.44403E-26	+1.11969E-25	-1.69355E-24	+8.26204E-28	+1.11649E-14
.....Alloy14.....								
Dkj (reduced n=NI)								
k / j	AL	CO	CR	MO	RE	RU	TI	W
AL	+6.84132E-13	+1.16968E-13	+2.62138E-13	+2.28776E-13	+1.76966E-13	-1.08184E-13	+3.58073E-13	+3.52165E-13
CO	-2.39071E-14	+7.51785E-14	-1.11554E-14	-1.35917E-14	-4.16143E-15	-1.28229E-13	-6.20417E-15	-2.56279E-14
CR	+3.3551E-15	-4.61149E-17	+1.12247E-13	+7.17963E-16	+1.41022E-15	-1.35471E-14	+8.13088E-15	+4.02778E-15
MO	+2.23994E-15	+2.7244E-16	+1.29699E-15	+9.18272E-14	-5.79056E-15	-2.01582E-14	+9.26726E-15	+6.68164E-16
RE	-2.07174E-14	-7.02519E-16	-3.17047E-15	-8.6617E-15	+5.22508E-15	-8.15694E-14	-1.03016E-14	-1.21643E-14
RU	-4.50947E-14	-7.70953E-14	-1.64725E-13	-5.48294E-14	-1.12218E-13	+1.7362E-12	-1.00579E-13	+4.78208E-14
TI	+4.12529E-14	+1.77109E-14	+4.97312E-14	+4.44813E-14	+3.51052E-14	-3.46802E-14	+2.35503E-13	+5.28942E-14
W	-2.83526E-25	-3.21931E-27	+3.93051E-26	-1.05239E-25	+8.54603E-26	-1.71224E-24	-3.89577E-26	+1.11649E-14
.....Alloy20.....								
Dkj (reduced n=NI)								
k / j	AL	CO	CR	MO	RE	RU	TI	W
AL	+6.85031E-13	+1.17193E-13	+2.63536E-13	+2.27263E-13	+1.79862E-13	-1.08358E-13	+3.59503E-13	+3.53569E-13
CO	-2.12391E-14	+7.64747E-14	-9.31501E-15	-1.17894E-14	-2.52117E-15	-1.2716E-13	-3.68188E-15	-2.33815E-14
CR	+3.62076E-15	+8.85924E-17	+1.12479E-13	+8.68966E-16	+1.58731E-15	-1.343E-14	+8.38612E-15	+4.26029E-15
MO	+5.31408E-15	+7.6684E-16	+3.03884E-15	+9.43846E-14	-1.13391E-14	-4.01683E-14	+1.93785E-14	+1.9343E-15
RE	-1.39958E-14	+2.04748E-16	-1.40703E-15	-5.05549E-15	+5.16085E-15	-6.055E-14	-6.31938E-15	-7.88917E-15
RU	-4.78126E-14	-7.78232E-14	-1.64476E-13	-6.27424E-14	-1.07231E-13	+1.73507E-12	-1.02493E-13	+4.68106E-14
TI	+4.2009E-14	+1.81E-14	+5.03429E-14	+4.4767E-14	+3.57533E-14	-3.43726E-14	+2.36298E-13	+5.35768E-14
W	-2.39715E-25	+1.72299E-26	+6.70873E-26	-6.65863E-26	+1.02637E-25	-1.69489E-24	+1.51084E-27	+1.11649E-14

Table 14: Diffusion coefficients (m^2s^{-1}) at 1273.15 K of 12 model Ni-base superalloys (continued).

.....Alloy21.....								
Dkj (reduced n=NI)	AL	CO	CR	MO	RE	RU	TI	W
k / j	AL	CO	CR	MO	RE	RU	TI	W
AL	+6.69131E-13	+1.1569E-13	+2.63583E-13	+2.23626E-13	+1.76736E-13	-1.09991E-13	+3.65025E-13	+3.54041E-13
CO	-1.21346E-14	+8.0217E-14	-3.39013E-15	-5.84417E-15	+1.80126E-15	-1.24121E-13	+4.88136E-15	-1.6592E-14
CR	+4.48313E-15	+4.93332E-16	+1.1088E-13	+1.38612E-15	+1.9808E-15	-1.30871E-14	+9.15939E-15	+4.9791E-15
MO	+8.26431E-15	+1.7735E-15	+4.70926E-15	+9.61141E-14	-1.05107E-14	-3.94275E-14	+2.21107E-14	+4.1764E-15
RE	-3.25711E-15	+6.67561E-16	+4.13615E-16	-5.35859E-16	+4.19586E-15	-1.96894E-14	-1.03576E-15	-1.642E-15
RU	-3.89987E-14	-7.45654E-14	-1.57641E-13	-6.83861E-14	-1.04199E-13	+1.73686E-12	-8.10283E-14	+6.12435E-14
TI	+4.47589E-14	+1.94925E-14	+5.19097E-14	+4.59283E-14	+3.68834E-14	-3.29543E-14	+2.35489E-13	+5.56164E-14
W	-1.13453E-25	+7.02116E-26	+1.47691E-25	+3.24441E-26	+1.64583E-25	-1.65012E-24	+1.01833E-25	+1.11649E-14
.....Alloy22.....								
Dkj (reduced n=NI)	AL	CO	CR	MO	RE	RU	TI	W
k / j	AL	CO	CR	MO	RE	RU	TI	W
AL	+6.76682E-13	+1.1623E-13	+2.63265E-13	+2.25068E-13	+1.78055E-13	-1.09349E-13	+3.61887E-13	+3.53424E-13
CO	-1.69261E-14	+7.82163E-14	-6.54736E-15	-9.05089E-15	-5.03674E-16	-1.25748E-13	+3.32572E-16	-2.02314E-14
CR	+4.02882E-15	+2.7803E-16	+1.11655E-13	+1.10369E-15	+1.76963E-15	-1.32691E-14	+8.74709E-15	+4.59601E-15
MO	+6.70996E-15	+1.22665E-15	+3.80941E-15	+9.51718E-14	-1.09729E-14	-3.98336E-14	+2.06553E-14	+2.97347E-15
RE	-8.00408E-15	+6.93145E-16	-1.1954E-16	-2.30234E-15	+4.98284E-15	-3.99079E-14	-3.22846E-15	-4.35057E-15
RU	-4.34268E-14	-7.62629E-14	-1.61138E-13	-6.55917E-14	-1.05787E-13	+1.73591E-12	-9.19006E-14	+5.38787E-14
TI	+4.33103E-14	+1.87553E-14	+5.10644E-14	+4.52693E-14	+3.62715E-14	-3.3696E-14	+2.35804E-13	+5.45181E-14
W	-1.80126E-25	+4.18745E-26	+1.04608E-25	-2.05254E-26	+1.3157E-25	-1.67402E-24	+4.7881E-26	+1.11649E-14
.....Alloy23.....								
Dkj (reduced n=NI)	AL	CO	CR	MO	RE	RU	TI	W
k / j	AL	CO	CR	MO	RE	RU	TI	W
AL	+6.85031E-13	+1.17193E-13	+2.63536E-13	+2.27263E-13	+1.79862E-13	-1.08358E-13	+3.59503E-13	+3.53569E-13
CO	-2.12391E-14	+7.64747E-14	-9.31501E-15	-1.17894E-14	-2.52117E-15	-1.2716E-13	-3.68188E-15	-2.33815E-14
CR	+3.62076E-15	+8.85924E-17	+1.12479E-13	+8.68966E-16	+1.58731E-15	-1.343E-14	+8.38612E-15	+4.26029E-15
MO	+5.31408E-15	+7.6684E-16	+3.03884E-15	+9.43846E-14	-1.13391E-14	-4.01683E-14	+1.93785E-14	+1.9343E-15
RE	-1.39958E-14	+2.04748E-16	-1.40703E-15	-5.05549E-15	+5.16085E-15	-6.055E-14	-6.31938E-15	-7.88917E-15
RU	-4.78126E-14	-7.78232E-14	-1.64476E-13	-6.27424E-14	-1.07231E-13	+1.73507E-12	-1.02493E-13	+4.68106E-14
TI	+4.2009E-14	+1.81E-14	+5.03429E-14	+4.4767E-14	+3.57533E-14	-3.43726E-14	+2.36298E-13	+5.35768E-14
W	-2.39715E-25	+1.72299E-26	+6.70873E-26	-6.65863E-26	+1.02637E-25	-1.69489E-24	+1.51084E-27	+1.11649E-14

Table 15: Diffusion coefficients (m^2s^{-1}) at 1273.15 K of 12 model Ni-base superalloys (continued).

(X _{ii})	AL	CO	CR	MO	RE	RU	TI	W
Alloy00	+3.22964E+05	+1.71517E+05	+1.81212E+06	+5.11566E+05	-	-	+8.58816E+05	+1.05856E+16
Alloy01	+3.27094E+05	+1.71783E+05	+1.81235E+06	+1.08943E+06	-	+4.63045E+05	+8.58972E+05	+1.05856E+16
Alloy02	+3.27643E+05	+1.71347E+05	+1.81152E+06	+5.58397E+05	-	+4.62648E+05	+8.54447E+05	+1.05856E+16
Alloy10	+3.27281E+05	+1.71606E+05	+1.80983E+06	+1.0945E+06	+4.56567E+05	-	+8.55229E+05	+1.05856E+16
Alloy11	+3.29296E+05	+1.71584E+05	+1.81086E+06	+1.09097E+06	+1.03396E+06	+4.6296E+05	+8.54875E+05	+1.05856E+16
Alloy12	+3.314E+05	+1.71392E+05	+1.80937E+06	+1.09248E+06	+5.04492E+05	+4.62884E+05	+8.50782E+05	+1.05856E+16
Alloy13	+3.33407E+05	+1.71208E+05	+1.80787E+06	+1.09396E+06	+3.27891E+05	+4.62817E+05	+8.46694E+05	+1.05856E+16
Alloy14	+3.35316E+05	+1.71031E+05	+1.80638E+06	+1.09542E+06	+2.39511E+05	+4.62757E+05	+8.42612E+05	+1.05856E+16
Alloy20	+3.27643E+05	+1.71347E+05	+1.81152E+06	+5.58397E+05	+1.05856E+06	-	+8.54447E+05	+1.05856E+16
Alloy21	+3.29743E+05	+1.7114E+05	+1.81002E+06	+5.59917E+05	+1.03588E+06	+4.62556E+05	+8.50342E+05	+1.05856E+16
Alloy22	+3.31746E+05	+1.70939E+05	+1.80851E+06	+5.6141E+05	+5.06393E+05	+4.62472E+05	+8.46242E+05	+1.05856E+16
Alloy23	+3.33651E+05	+1.70746E+05	+1.807E+06	+5.62876E+05	+3.29763E+05	+4.62397E+05	+8.42147E+05	+1.05856E+16

Table 16: Thermodynamic factors X_{ii} (J/mol-at) at 1273.15 K.

Here, we restrict to major terms, X_{ii} since the off-diagonal elements of the thermodynamic factor matrix obtained from DICTRA are several orders of magnitude smaller than the major terms.

5.1.3 Material parameters

The cubic elastic constants for the 12 model model superalloys are $C_{11}^{\gamma} = 215.5$ GPa, $C_{12}^{\gamma} = 162$ GPa, $C_{44}^{\gamma} = 77.6$ GPa for the matrix and $C_{11}^{\gamma'} = 222.7$ GPa, $C_{12}^{\gamma'} = 164.2$ GPa,

$C_{44}^{\gamma'} = 85.6$ GPa for the precipitate. A value of -0.14% is adopted from Pyczak et al. [61] as the misfit for all the alloys. In the simulations, the interfacial energy is assumed isotropic, with a value of 80mJ/m² for all the alloys. The kinetic coefficient a K is related to the interdiffusion coefficients obtained from DICTRA. The kinetic coefficient K for each alloy is chosen to be larger than any term in the diffusion matrix.

5.2 Coarsening law during non-directional γ' -coarsening

The discussion of Ostwald ripening and the LSW-theory has a long history with respect to the application to the description of γ' -coarsening in Ni-base superalloys [2, 3]. Nevertheless, there are still a number of open questions concerning the many aspects that come along with the application of the LSW-theory to γ' -coarsening in Ni-base superalloys, such as the prediction of coarsening rate constant, the prediction of the particle size distribution as well as the determination of the coarsening exponent. However, within the present article, we focus on the discussion of the last point, namely: the coarsening exponent. This aspect is discussed with regard to theoretical extensions to multi-component diffusion and subsequent phase-field simulations of coarsening with the mean particle radius of γ' -precipitates as the quantitative measure.

5.2.1 Stress-free binary alloys

First-order phase transformations typically results in a two phase mixture of second phase precipitates embedded in a matrix. However, the microstructure is thermodynamically unstable due to the larger amount of surface area present [74]. The desire of the overall system to reduce its total amount of interface area results in the coarsening of precipitates. The related driving force is the Gibbs-Thompson effect of capillarity. Coarsening typically results in the increase of the mean precipitate size. Assuming a spherical precipitate shape and that only a single length-scale, namely R exists, the driving force for the ripening process according to is the curvature dependence of the diffusion potential [53],

$$\delta\mu = \gamma\kappa a^3, \quad (178)$$

where $\kappa = 2/R$ and a^3 is the atomic volume and γ is the isotropic surface energy. The change in precipitate radius in time follows

$$\frac{dR}{dt} = -\vec{j} \quad (179)$$

where \vec{j} is the flux of solutes.

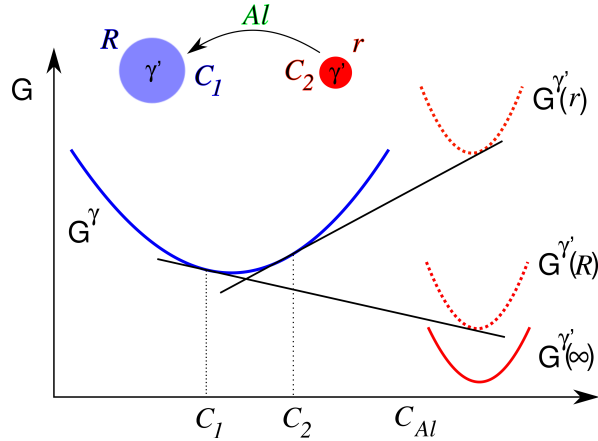


Figure 35: Origin of coarsening in a binary Ni-Al alloy (figure following [59]). The Al diffusion potential around the smaller precipitate with a radius of curvature (r) is higher than that around the larger precipitate with radius of curvature (R), as a result concentration of Al is highest in the vicinity of the smaller γ' -precipitate.

Since only a single length scale R exists and the concentration field around a particle is determined by the radius of the curvature. The diffusion potential gradient can then be described as the ratio of the driving force for the ripening process and the radius of the curvature

$$\nabla\mu \approx \frac{\delta\mu}{R} \quad (180)$$

This results in the dissolution and eventual disappearance of energetically unfavorable surfaces with high curvatures as shown in Fig. 35. Further expansion of Eq. (179) yields

$$\frac{dR}{dt} = M \frac{\delta\mu}{R}. \quad (181)$$

Inserting Eq. (178) into Eq. (181) and further integration yields

$$R^3(t) - R^3(0) = kt, \quad (182)$$

where k is the coarsening rate constant and R_0 is the initial radius. This solution corresponds to the theory for binary system by Lifshitz and Slyozov [49] and Wagner [75]. The theory was developed under the assumptions of coarsening of stress-free systems with an almost vanishing volume fraction. This theory is also applicable to alloys with a high volume fraction [26, 77].

5.2.2 Stress-free multi-component alloys

In the following, we extend the classical LSW-theory for binary alloys to multi-component diffusion by employing a scaling argument similar to the one established in Müller-Krumbhaar [53]. For spherically shaped precipitate, this driving force is proportional to the inverse of the radius R of the particle

$$\delta f_\sigma = \sigma \kappa = \frac{2\sigma}{R}, \quad (183)$$

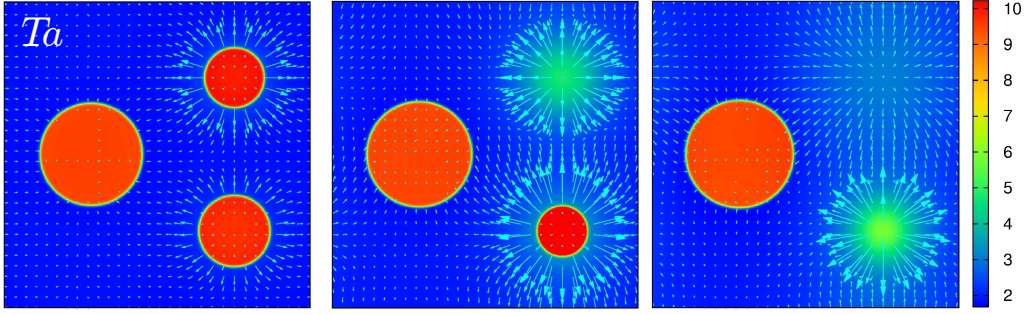
where $\kappa = 2/R$ is the sum of the principle curvatures and δf_σ denotes the free energy density release due to the change of the total interface area. However, any morphological change in the microstructure is related to phase transformations between the γ - and γ' -phase which involves material transport of the alloying constituents. In particular, a $\gamma \rightarrow \gamma'$ transformation is accompanied by a release of the elements that partition to the γ -matrix and a capture of the elements that partition to the γ' -phase as shown in Fig 36.

The resulting local accumulation or depletion zones are transported diffusively through the γ -matrix. At the γ/γ' -interface, the conditions of material-conservation for each of the alloying constituents is given by [14, 47]

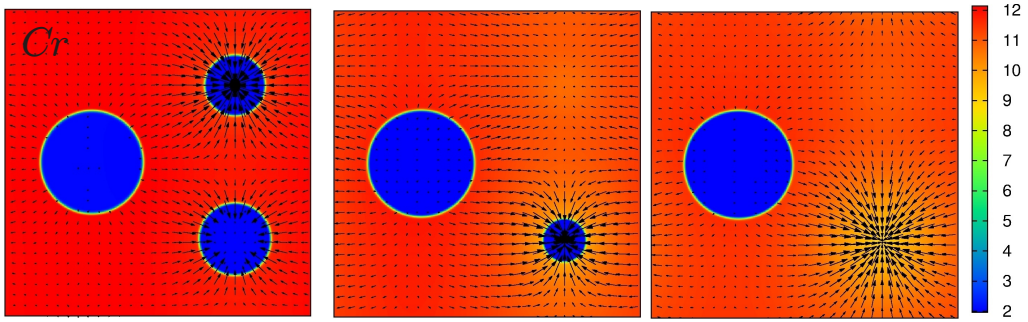
$$v_R \Delta c_i = \frac{dR}{dt} \Delta c_i = \sum_j \left(M_{ij}^{\gamma} \nabla \mu_j|_{\gamma} - M_{ij}^{\gamma'} \nabla \mu_j|_{\gamma'} \right), \quad (184)$$

where v_R is the radial velocity of the γ/γ' -interface, Δc_i is the miscibility-gap of species i , M_{ij}^p is the mobility-matrix of phase p , and μ_i denotes the diffusion potential of species i . In the quasi-steady state growth of the spherical γ' -particle in the supersaturated γ -matrix, the concentration profile becomes flat on the γ' -side [14], which implies that we can concentrate on the diffusion in the γ -matrix only.

The core of the classical LSW-law is a dynamic equilibrium between the thermodynamic driving forces that arise from the Gibbs-Thompson effect on the one hand and on the other hand from the chemical deviations from two-phase equilibrium due to the diffusive transport. For a single diffusion component, such as in binary alloys, the central scaling argument is that the size of the diffusion field around the spherical γ' -particle is given by the particle radius R at any time of the process [49, 53]. We point out that the scaling with the radius R stems from the nature of the quasi-static solution to the problem of one-component diffusion limited growth of a spherical particle [14]. Here, we argue that this scaling should also hold for multi-component diffusion, because the multi-component influence does not change the principle nature of the governing equations.



(a) The diffusion potential of Ta increases in the γ -matrix around a precipitate as the radius of curvature decreases. Resulting diffusion potential gradients lead to the flux of Ta solutes from smaller to larger precipitates. This allows the larger γ' -precipitates to grow in size while the smaller ones shrink and vanish.



(b) The diffusion potential of Cr increases in the γ -matrix in the vicinity of a precipitate as the radius of curvature increases. The diffusion potential gradients drive the flux of Cr solutes from γ -matrix around the larger precipitates to the vestige of the shrinking smaller γ' -precipitates.

Figure 36: Ostwald ripening of spherical precipitates in a multi-component alloy. The driving force for coarsening of the stress-free coherent microstructure is a combination of thermodynamic driving forces that arise from the Gibbs-Thompson effect and the chemical deviations from two phase γ - γ' equilibrium due to diffusive transport. The color scheme represents the concentration in wt.%. and the flux represents the flux of solutes.

Knowing the scaling of the size of the multi-component diffusion field, we can estimate the driving force from diffusion δf_d that acts on the γ/γ' -interface. Similar to Müller-Krumbhaar [53], we assume here $\delta f_d = \sum_j \delta \mu_j \approx R \sum_j \nabla \mu_j$. Now, employing the dynamic equilibrium of driving forces, $\delta f_\sigma = \delta f_d$, and Eqs. (183) and (184), we finally obtain an ordinary differential equation for the particle radius as function of the time,

$$R^2 dR = k \cdot dt, \quad (185)$$

where $k \approx 2\sigma / \left(\sum_{jk} (M_{jk}^\gamma)^{-1} \Delta c_k \right)$ is the resulting coarsening rate constant, which is related to the interface energy and an effective mobility of the multi-component system. Here, $(M_{jk}^\gamma)^{-1}$ is the inverse mobility matrix. Finally, an integration of Eq. (185) yields

the classical LSW-law

$$R^n(t) - R_0^n = kt, \quad (186)$$

where the coarsening exponent n turns out to be 3 and R_0 is the initial particle radius at time $t = 0$. It can be seen that the extension of LSW theory to multiple component diffusion does not alter the coarsening exponent. The picture changes completely when elastic effects are included, as we shall show in the following via simulations. Notice, that the coarsening rate constant calculated here is only a rough estimate. A precise determination of the rate constant in the presence of the multi-component diffusion would of course require a more detailed evaluation of the driving force equilibrium employed above, and this is beyond the scope of the present article. Alternative derivations of the coarsening law for multi-component alloys are done in Refs. [44, 45, 62].

5.2.3 Elastically stressed Ni-base superalloys with different Re contents

As seen in the preceding discussion, the classical LSW-theory as well as the multi-component extension does not include elastic interactions between coherent precipitates. We point out that there has been a number of attempts to include effects from elastic interactions. Some studies suggest that coarsening is diffusion-controlled. For example, coarsening in the early stages of the precipitation process was found to follow the LSW-theory with an exponent of $n = 3$ [77]. On the other hand, a number of studies suggest that the coarsening exponent changes or even varies in different alloys when the elastic effects become more important. For example, [78] found coarsening in a number of Ni-base superalloys to be diffusion-controlled with $n = 3$, interface reaction controlled with $n = 2$ or controlled by both. Further, in Ref. [32], exponents ranging between 2 to 10 were observed during coarsening in Ni-base superalloys with varying compositions. Clearly, one can not randomly apply the LSW-theory to coarsening in Ni-base superalloys.

The focus of this subsection is to determine if Eq. (182) holds for the coarsening regime when the precipitates are large enough such that only the anisotropic elastic energy is dominant. We perform large-scale 2D phase-field simulation studies of coarsening in two alloys: CMSX4 and its derivative Alloy20. The composition of the two superalloys is given in Table 9.

To determine the exponent n , a plot of $\log(R(t))$ vs $\log(t + R_0^n/k)$ is constructed. We calculate the mean particle radius at each time step in the simulation as

$$R = \sqrt{V_f/\pi N(t)}, \quad (187)$$

where V_f is the total 2D volume of γ' -precipitates and $N(t)$ is the precipitate number. We redefine time $t = 0$ as shown by the dashed line in the insert of Fig 37. The time $t = 0$ is when the Gibbs-Thompson effect and the chemical driving forces have reached some equilibration, i.e. the volume fraction becomes constant (without elastic effects).

A drop in the actually observed volume fraction as compared to the thermodynamically calculated phase fraction is attributed to the initialization of the system starting from a uniform diffusion potential throughout the domain. Furthermore, in the presence of elastic effects, the drop in the phase fraction is augmented by the elastic hysteresis effect. In the framework of our large-scale 2D phase-field simulation studies on the temporal evolution of the precipitates, we start from a γ - γ' microstructure with 480 fine γ' -particles. The initial microstructure is generated directly from an SEM photograph of an as-heat treated sample of the commercial CMSX4 superalloy. The generation method has been described previously in detail in subsection 3.2.3. During the simulation, it was possible to monitor coarsening up to late times where the number of particles reduced to 16. During runtime of the simulation, the mean particle radius increased by a factor of about 5.5. These large-scale simulation with a large particle number were necessary to gain good statistics.

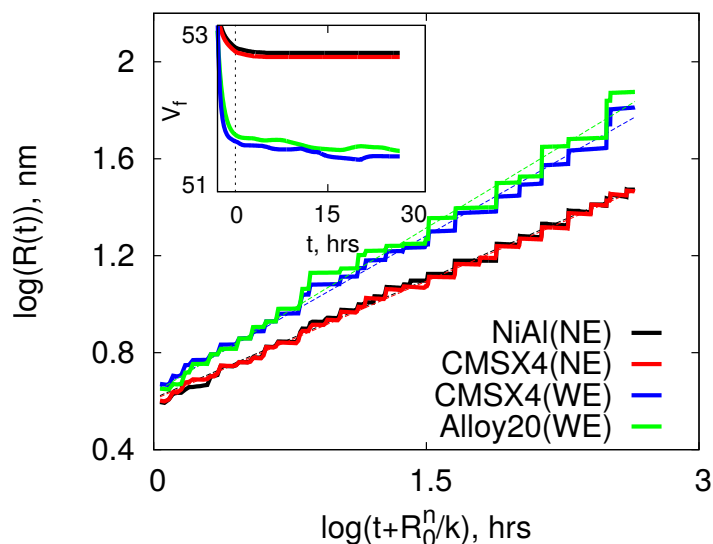


Figure 37: Log-log plot of coarsening kinetics. Here, NiAl(NE) denotes coarsening of NiAl without elastic effects, CMSX4(NE) without elastic effects, CMSX4(WE) with elastic effects and Alloy20(WE) with elastic effects. The composition of the two alloys is the same except for 0.98at.%Re in CMSX4 and 2at.%Re in model Alloy20. The coarsening exponent is $n = 3.07$ ($k = 0.0679$ nm/h) for NiAl(NE), $n = 3.08$ ($k = 0.0668$ nm/h) for CMSX4(NE), $n = 2.35$ ($k = 0.060$ nm/h) for CMSX4(WE) and $n = 2.2$ ($k = 0.0621$ nm/h) for Alloy20(WE). Insert: The fitting of the log-log plot starts at $t = 0$ when the volume fraction becomes constant.

The fitting for the evaluation of the coarsening exponent n is then done starting from the redefined time $t = 0$ when the constant volume fraction has been reached. We first determine the exponents for coarsening without elastic effects in Ni-20wt.%Al denoted as NiAl(NE) and a multi-component superalloy denoted as CMSX4(NE). The log-log

plot reveals an exponent of $n = 3.12$ for NiAl(NE) and $n = 3.1$ for CMSX4(NE). The exponents are almost equal to the exponent derived in Eq. (182) for the case of coarsening without elastic effects. The fitting is then done for the case of coarsening with elastic effects for the two alloys, denoted as CMSX4(WE) and Alloy20(WE). A coarsening exponent of $n = 2.38$ is found for CMSX4(WE) and $n = 2.33$ for Alloy20(WE). The different coarsening exponents for CMSX4(WE) and Alloy20(WE) is a result of the uncertainty in the fitting. The exponents identified in our simulations are in agreement with the simulations of Leo et al. [38] who by employing a scaling argument predicted that elastic effects change the exponent from $n = 3$ to $n = 2$, if the precipitates are harder (i.e., more rigid) than the matrix. Although, the assumption of self-similarity in [38] does not hold for Ni-base superalloys due to their largely anisotropic microstructures, the influence of elastic effects on coarsening kinetics was clearly highlighted. Given the presence of elements with low diffusivities in CMSX4 and Alloy20, e.g., Mo, Re, W etc, one would expect the coarsening process in these superalloys to be diffusion-controlled. However, an additional contribution from the misfit strains leads to a substantially faster coarsening evolution as compared to the prediction from the LSW-theory.

To analyze the sensitivity of the model in determining the coarsening exponents, phase-field simulations with a system of normal size (NS), with a relative grid size of $\Delta x/\xi = 0.2$ and a system of double size (DS) with $\Delta x/\xi = 0.4$ where Δx is the grid spacing and ξ is the interface width, are done. The deviation in the coarsening exponents for the two cases is evaluated as $\Delta n = (DS - NS)/NS$. The deviation is found in the order of 0.03. This implies that the calculated exponents are not influenced by the choice of the phase field interface width and grid spacing. Further, we assume Ostwald ripening to be the main mechanism of coarsening we observe, since it is known to be the dominant mechanism in the late stages of coarsening.

5.3 Influence of Re and Ru additions on cube→plate-like transformation

The addition of refractory elements has been known to influence the characteristics of late-stage solidification in Ni-base superalloys. The experimental work [36], found Re to increase the liquidus temperature although it has the tendency to increase the formation of topologically close packed phases. Ru was added as a substitute for Re but it was judged to have little effect on the solidification process. Here, we now perform a virtual experiment using the phase field based tool to determine the influence of Re and Ru on cube→plate-like transition. The phase field based simulation tool can be used as a cheap and fast acting tool for the optimization of alloys with respect to coarsening.

We investigate the cube→plate-like transition in 12 model Ni-base superalloys with compositions adopted from Heckl et al. [36]. The model Ni-base superalloys are derived from CMSX4 with a chemistry of 12.58Al, 9.26Co, 7.58Cr, 0.38Mo, 0.98Re, 2.18Ta, 1.98W and bal. Ni in at.%. The compositions of the alloys are systematically varied by stepwise additions of 0 to 2 at.% Re and 0 to 4 at.%Ru at the expense of the base element

Ni. The other elements are held constant, which allows for a systematic study of the influence of Re+Ru on the coarsening. The model superalloys are designated; Alloy00, Alloy01, Alloy02, Alloy10, Alloy11, Alloy12, Alloy13, Alloy14, Alloy20, Alloy21, Alloy22, Alloy23. The first digit in the model superalloy designation is the Re content whilst the second is the Ru content.

We limit the virtual experiment to the case of coarsening of an isolated and initially cuboidal γ' -precipitate under a load. The equilibrium γ' -precipitate volume fractions of Ni-base superalloys under study are probably different but for the sake of comparison, we initiate the simulations from one universal phase and concentration field. Rafting is induced by applying a compressive strain ($\varepsilon_a = -0.2\%$) parallel to the (010)-crystallographic plane. The CMSX4 and its derivative alloys used in this study have a negative anisotropy, i.e. $C_{11} - C_{12} - 2C_{44} < 0$, which implies that the elastically soft orientations corresponds to the $\langle 100 \rangle$ crystallographic directions. Due to the negative misfit and the compressive strain, the γ' -precipitate elongates along the energy minimizing [010]-crystallographic direction as in Fig. 38.

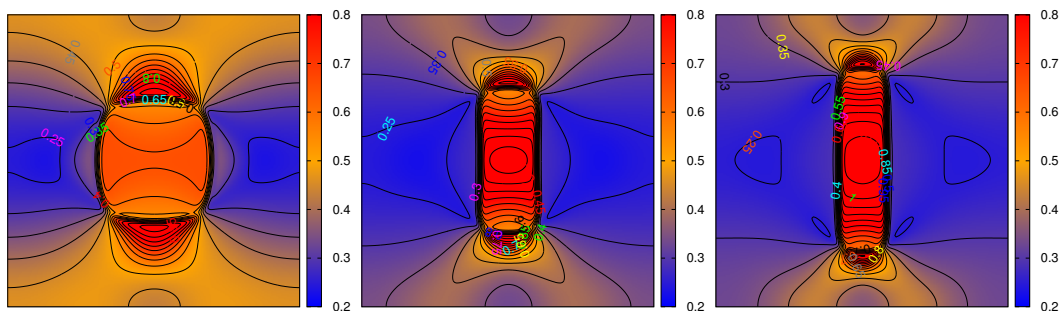


Figure 38: Elastic energy density during cube \rightarrow plate-like transition of precipitate after applying a compressive strain ($\varepsilon_a = -0.2\%$) parallel to the (010)-crystallographic plane. The precipitate elongates along the elastically soft [010]-crystallographic direction.

To quantify the influence of Re and Ru additions on the cube \rightarrow plate-like transition during rafting, we use the aspect ratio defined in Eq. (173). The aspect ratios obtained after 5 h of rafting are then plotted as a function of Ru for different constant Re. The larger(smaller) the aspect ratio, the smaller(larger) the influence of the Re+Ru content on rafting. Fig 39 (a)-(c) show the aspect ratios obtained after 5 h of rafting as a function of the Ru contents for different constant Re.

We first reproduce the sensitivity study done in chapter 4. We limit the sensitivity study by artificially modifying the diffusion coefficients of Mo in Alloy01 and Alloy02. The blue and grid points in Fig 39 (a) show the aspect ratios obtained during a sensitivity study with artificially changed diffusivities of Mo. The sensitivity study for the Re-free Alloy01 and Alloy02 alloys, shows that; first - the model responds to changes in the kinetic parameters; second - the element Mo has albeit small, a rate-limiting influence on the rafting kinetics and thus can be used just like Re for the fine tuning of alloy

microstructures. A more comprehensive sensitivity study considering several elements was done in the work [54]. We now perform study on the 12 alloys using the real thermodynamic and kinetic parameters.

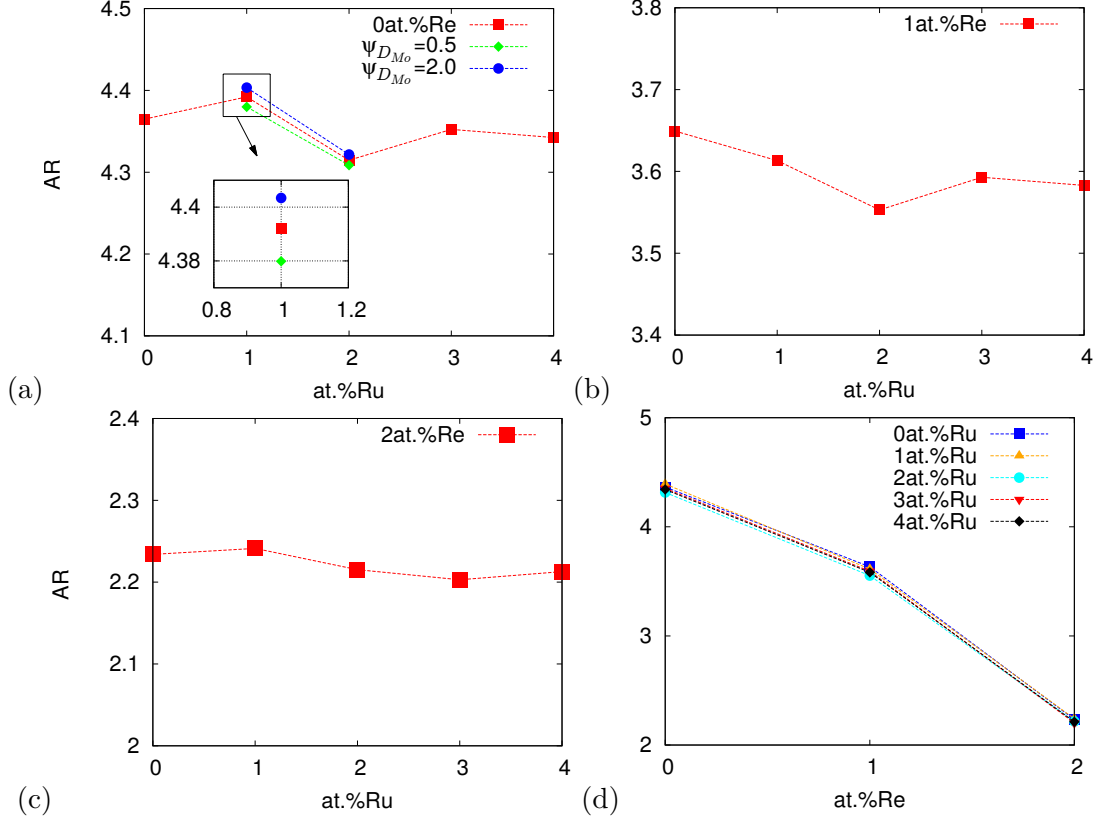


Figure 39: Aspect ratios after 5 h of rafting at 1273.15 K as a function of; (a)-(c) Ru contents for different constant Re; (d) Re contents for different constant Ru. A variation of Ru content has no significant effect on the γ' -morphology while but an increase in the Re content leads to a significant reduction of cube \rightarrow plate-like transition. The blue (circles) and green (diamond) lines-points in (a) show the aspect ratios obtained from a sensitivity study with artificially changed diffusivities of Mo. The sensitivity study shows that in the Re-free Alloy01 and Alloy02 alloys, the element Mo has albeit small, a rate-limiting influence on the rafting kinetics and thus can be used just like Re for the fine tuning of alloy microstructures and the respective coarsening kinetics.

The plots show that the rate of cube \rightarrow plate-like transition decreases as the Re content is increased from 0 to 2at.%. An aspect ratio of around 4.5 is obtained after 5 h when the Re content is 0at.%Re. The aspect ratio becomes 3.65 when 1at.%Re is added. Further additions to 2at.%Re reduces aspect ratio to 2.2. The presence of Re in the

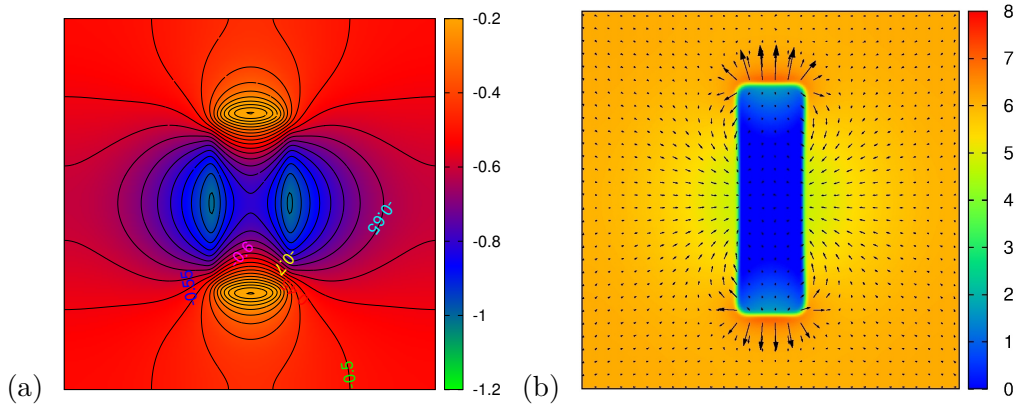


Figure 40: (a) Diffusion potential field of Re during rafting of a γ' -precipitate under a compressive strain ($\varepsilon_a = -0.2\%$) applied parallel to the (010)-crystallographic plane; under such a loading condition, the diffusion potential of Re is higher in the vicinity of the horizontal γ/γ' -interfaces than in the vicinity of the vertical γ/γ' interfaces - this favors the flux of Re from the horizontal channels to the vertical channels. (b) Concentration field (in wt.%); due to low solubility of Re in the γ' -precipitate and its low diffusivity, Re solutes accumulate in front of the elongating γ/γ' -interfaces. This effect slows down the the motion of the interface and consequently the elongation of the γ' -precipitate.

γ -matrix favors the preservation of the quasi-cuboidal morphology. Further simulations where done at an increased Re content up to 5at.% content, a similar trend in the reduction of cube \rightarrow plate-like transition was observed. Our work [54] has already revealed that the presence of Re enrichment zones in the γ -matrix hinders γ - γ' interface motion which lead to a reduction in rafting. Fig 40 shows the rate limiting effect of Re during rafting. Therefore, the trend observed in Fig. 39 where the rate of rafting decreases as the Re additions increase can be explained as follows: since diffusion depends on the composition, the higher the content of Re in the γ -matrix, the slower the γ - γ' interface motion. This simulation observation supports the experimental studies of [32, 86] where an influential role of Re on the microstructure and kinetics during coarsening in Ni-base superalloys was observed. The simulations reveal that Ru variations have no significant effect on the cube \rightarrow plate-like transition. Thus, Ru is not a good replacement for Re in terms of reducing the degradation of Ni-base superalloys through coarsening. As a result, in alloy optimization, the Ru content can be freely changed with regard to hindering the precipitation of topologically close packed phases as done by [36, 35], while maintaining the rate-limiting influence of Re on coarsening.

5.4 Conclusion

The coarsening kinetics of γ' -precipitates in single crystalline Ni-based superalloys was studied using phase-field simulations with inputs from CALPHAD-type thermodynamic and kinetic databases. Besides the explicit resolution of the $\gamma \rightarrow \gamma'$ transformations coupled to multi-component diffusion, the model used in the simulations also accounts for anisotropic elastic effects which emanate from misfit-strains at the coherent phase boundary.

Firstly, the temporal evolution of coarsening was discussed in the context of theoretical extension of the LSW-theory to multi-component alloys. Simulations were done to identify the coarsening exponent for elastically stressed Ni-base superalloys with the explicit inclusion of up to nine chemical components. The simulation studies showed that an additional influence from the coherency strain leads to a substantially faster coarsening-evolution compared to the predictions from the LSW-theory. The simulations also reveal that the influence of compositional effects on the coarsening kinetics is minor compared to the elastic ones.

Secondly, a virtual experiment to determine the influence of varying (Re) and (Ru) contents on the kinetics of cube to plate-like transition was performed. Consistent with previous results, we observed that a change in the Re content strongly alters the kinetics of cube to plate-like transition. On the contrary, it is found that Ru variations have no significant effect on the coarsening kinetics, which implies that in further alloy developments, the Ru content can be freely optimized with regard to other aspects e.g., to suppress the formation of the detrimental topologically close packed phases, while maintaining the rate-limiting influence of Re on coarsening. In general, the model can be used as a tool to systematically analyze coarsening in elastically stressed multi-component alloys and thus allows for true alloy design and related sensitivity studies of elements.

6 Summary

The general objective of this thesis was to perform computational studies of the morphological evolution and kinetics during aging heat treatment of single crystal Ni-base superalloys. To that end, an integrated computational tool based on the phase field method was respectively further developed. As a first step towards the creation of the computational tool, a step-wise formulation of a quantitative phase-field model for simulating microstructural evolution in multi-component systems was presented in the thesis. The step-wise development included the formulation and validation of multi-component thermodynamics, inclusion of anisotropic effects and the application to solid-state transformations in Ni-base superalloys. The computational tool was applied for the prediction of microstructural changes during the aging heat treatment of single crystal Ni-based superalloys. In addition to that, it was used to analyze the relative contributions of solute diffusivity and segregation to morphological evolution in chemically complex commercial single crystal superalloys with up to a dozen alloying elements.

A multi-component phase field model coupled to inputs from the commercial TTNi8 and MobNi1 databases for the thermodynamic and kinetic driving forces, respectively, was developed. The thermodynamic formulation of the multi-component phase field model was extended from the binary model based on the grand-potential formalism of Plapp [58]. As opposed to the well-known Kim-Kim-Suzuki (KKS) model [42], the need to solve the equilibrium condition at each time step is eliminated. By virtue of the concentration fields being a function of the diffusion potential, the equilibrium condition is automatically satisfied in the extended multi-component model. This greatly reduces the computational costs when it comes to simulating alloys with a multiple number of elements. The diffusion equations of the extended multi-component model take into account the cross interactions between all the solutes in the multi-component alloy, even the slow diffusing ones e.g, Re, W etc. The multi-component model uses a symmetric model for diffusion which assumes equal diffusion in both phases - which eliminates the need to incorporate the anti-trapping current in the diffusion equations. The consistency of the thermodynamic formulation was validated by comparing phase-field simulations to DICTRA sharp interface and ThermoCalc equilibrium simulations. To perform simulations similar to DICTRA, dimensionless phase-field equations excluding elastic effects were used in the validation. The DICTRA calculations naturally assume a sharp interface setting. The results showed an agreement of the time evolution of concentration profiles and volume fraction obtained by phase field and DICTRA as well as the equilibrium phase concentrations and volume fraction obtained by phase field and ThermoCalc. The observed agreement of the phase field simulations to DICTRA and ThermoCalc simulations demonstrated the feasibility of the phase-field model to efficiently and accurately predict of inter-diffusion limited transformations in Ni-base superalloys. It should be noted here that the choice of the interface width in the phase field is critical to the agreement to the DICTRA model. Provided that the phase-field model operates in a sharp interface limit, where the interface width is negligibly small compared with the diffusion length as well as the total length of the system, the resulting growth kinetics

are in good agreement with the DICTRA simulations.

As a second step towards the creation of the computational tool, different approaches of incorporating the anisotropies of the interfacial and elastic energies in the phase-field framework were formulated and tested. The general aim here was to show that the interfacial energy anisotropy and elastic anisotropy can both lead to the formation of precipitates with four-fold symmetry. To understand these effects, two independent studies were done. First, two approaches of including the anisotropy of the interfacial energy via an orientational dependence of the interfacial energy in phase-field framework: In the first anisotropic formulation, the interface width was considered to vary with the orientation, while in the second rather new model only the interfacial energy was chosen to be anisotropic, leading to a constant interface width. Applying to the quasi-one-dimensional case with a planar interface of fixed orientation, we demonstrated, that both approaches are suitable for quantitative modeling. However, in this respect, the varying interface formulation requires extra care due to the intrinsic kinetic anisotropy. To study equilibrium shapes, efficient volume conserving Allen-Cahn dynamics were used, where through a properly chosen time dependence of a spatially constant chemical potential growth or shrinking of the particle is prohibited. To remove the ill-posedness of the phase-field equations for high-energy orientations, which do not belong to the equilibrium shape, the convexification method of Eggleston et al. [16] was employed. For both anisotropic phase-field formulations, the computed equilibrium particle shapes, both with and without sharp corners, are in excellent agreement with the analytic Wulff construction. Special emphasis was given to the numerical implementation of the discussed anisotropic phase-field models. In this respect, we developed a new explicit finite-difference scheme using a stagnation grid formulation, due to the appearance of mixed spatial derivatives in the governing equations. Furthermore, we demonstrated that this scheme provides sufficient accuracy to be able to simulate even and odd symmetries as well as high angle rotations of the underlying crystalline orientation. We also discussed a formulation to incorporate the dependence of the total strain on the phase field. Elastic anisotropy and inhomogeneity were also introduced by postulating the cubic elastic constants to be dependent on the dimensionless phase field order parameter. The formulation was similar to Steinbach et al. [69] which assumes equal elastic stresses in the two bulk phases at the diffuse interface. The formulation resulted in an Allen-Cahn type second order equation coupled to a set of second order multi-component diffusion equations. The phase field equation and multi-component diffusion equations were solved on uniform square grids using explicit finite-difference methods. The phase field model also incorporated an Jacobi iterative algorithm for numerically solving the mechanical equilibrium of an elastically inhomogeneous system. For numerical stability, particular attention was paid to the numerical implementation of the mechanical equilibrium for the calculation of the displacement fields required to calculate the elastic driving force. The Jacobi relaxation scheme was based on the explicit finite difference with elastic variables on a staggered grid. The computed equilibrium cuboidal morphologies and $(100)_{\gamma}|| (100)_{\gamma'}$ orientation relationship was consistent with the typical “as-heat treated” microstructures of Ni-base superalloys. The sphere to cube

transition was attributed to the anisotropic growth rates of the interface along the $\langle 111 \rangle$ and $\langle 100 \rangle$ -crystallographic directions. The simulations showed that a high interfacial energy anisotropy and elastic anisotropy can both lead to the formation of precipitates with four-fold symmetry. However, challenges can arise when both anisotropies are incorporated in a model. Including both the anisotropy of the interfacial energy in a phase field model with elastic effects requires the precise knowledge of the relative weighting of the contributions from interfacial energy and elastic anisotropies. At the moment, this is tough to quantify due to the lack of experimental data of the anisotropy of the interfacial energies in Ni-base superalloys.

Phase field simulations of aging at 1000°C of Ni-base superalloys alloys containing varying amounts of Re and Ru were done to analyze the influence of anisotropic elastic effects which emanate from misfit-strains at the coherent phase boundary on the coarsening exponent. For quantitative analyses, the simulations were performed using initial microstructures obtained from SEM photographs of “as-heat treated” samples. To simulate the aging process, phase field simulations were done with contributions from the isotropic interfacial energy, misfit and elasticity inhomogeneity. The study was done for the binary NiAl and CMSX4 and its derivative alloys with up to eight elements. A degradation of the microstructure via coarsening of the precipitates was observed - the as “heat treated” cuboidal precipitates morphed into rather irregularly shaped precipitates with no preferential alignment orientation. The shape of the precipitates is determined by the elastic interactions with its nearest neighbors. Coalescence of some precipitates was observed in the early stages before Ostwald ripening became dominant in the later stages. We studied the applicability of the LSW law [49, 75] to coarsening in alloys with a coherent elastic misfit. The temporal evolution of coarsening was first studied in the context of theoretical extension of the LSW-theory to multi-component alloys. The temporal evolution was then studied in Ni-base superalloys with the explicit inclusion of up to nine chemical components using phase field simulations with and without elastic effects. Large-scale simulations of the aging process with up to 500 precipitates were done. The large particle number was particularly necessary to gain good statistics. The simulation studies showed that an additional influence from the coherency strain energy leads to a substantially faster coarsening-evolution compared to the predictions from the LSW-theory which was developed initially for stress-free binary alloys. The simulations also revealed that the influence of compositional effects on the coarsening exponent are minor compared to the elastic effects. Due to the relatively high volume fractions of around 50% and the thin matrix channels, a study was done to analyze if the multi-component model did not induce spurious coalescence between neighboring precipitates. To analyze the sensitivity of the phase field model in calculating the coarsening exponents, simulations with different relative grid sizes were done. The deviation in calculated exponents for the different relative grid sizes was found to be no larger than 3%. We safely concluded that the calculated exponents in the simulations were not influenced by the choice of the phase-field interface width and grid spacing. As such, the coalescence observed in the early stages of the coarsening process was essentially a result of long-range elastic interactions. The coalescence was limited mainly to the early stages

of the coarsening process, after which Ostwald ripening became the dominant mechanism. Thus, it is legitimate to consider Ostwald ripening to be the dominant effect for long term studies for the extraction of the coarsening exponents.

Studies were done to analyze the influence of alloying composition on γ' -rafting kinetics during exposure at 1000°C of Ni-base superalloys alloys with contributions from the isotropic interfacial energy, negative misfit, elasticity inhomogeneity and compressive strain applied along the [100]-direction. Under the compressive load, a transformation from the as “heat treated” cuboidal γ' -precipitates to plate-like structures aligned along the elastically soft [010]-direction, i.e., rafting, was observed. Coalescence and elongation of the precipitates was observed in the early stages before ripening became the dominant mechanism in the later stages. To characterize the rafting evolution, an integrated tool to quantify the evolution kinetics of microstructures with anisotropic γ' -precipitates and also to identify systematically the sensitivity of different elements on resulting morphologies was developed. The integrated characterization tool used the aspect ratio calculated on the basis of interface orientations as a quantitative measure. A unique feature of the integrated characterization tool is that it quantifies the coarsening kinetics of anisotropic and coalesced precipitates. Firstly, rafting was studied in the commercial CMSX4 and CMSX6. The simulations revealed that the rafting process is considerably slower in CMSX4 than in CMSX6. In this context, it was conclusively shown that the presence of slow diffusing elements in CMSX4, plays a major role in reducing the rate of γ' -coarsening. The results elucidated that Re slows the interface mobility by accumulating along the path of the moving interface. The fact that Re is not soluble in the precipitate and that its diffusivity is low leads to its accumulation along the paths of the moving $\gamma-\gamma'$ interfaces. The Re accumulation zones hinder the motion of $\gamma-\gamma'$ interfaces which slows down coarsening. One can conclude that the presence of Re in alloys hinders the formation of rafts in Ni-base superalloys. Whether raft formation is beneficial or not to the properties of Ni-base superalloys is still up for discussion in the materials science field. Secondly, a virtual experiment to determine the influence of varying Re and Ru contents on the kinetics of cube to plate-like transition was done. The simulation was done for 12 model superalloys derived from CMSX4. The compositions of the alloys were systematically varied by stepwise additions of 0–2 at% Re and 0–4 at% Ru at the expense of the base element Ni. The virtual experiment was done by systematically quantifying the relative contribution of each solute in the superalloys to rafting. The motivation to jointly vary the Re and Ru additions emanated from the notion that Ru could be a replacement for Re to retard the formation topologically close packed phases during solidification as suggested by Caron [12] and Heckl et al. [35, 36]. Consistent with previous results, it was observed that a change in the Re content strongly altered the kinetics of cube to plate-like transition. However, it was found that Ru variations have no significant effect on the coarsening kinetics, which implies that in further alloy developments, the Ru content can be freely optimized with regard to other aspects e.g., to suppress the formation of the detrimental topologically close packed phases, while maintaining the rate-limiting influence of Re on coarsening. Our studies allow a systematic quantification of the relative contribution of each solute in a superalloy to rafting.

This is the first step towards a simulation-based design and optimization of alloy compositions. The sensitivity and numerical techniques presented in this work can be used to develop composition-structure correlations in Ni-base superalloys.

The model developed in this thesis can be used as a tool to systematically optimize several elements in parallel for a desired microstructure. The advantages of the phase-field method were highlighted in that it allows to visualize how the different phenomena discussed in the literature evolve in time. Furthermore, it allows for the analysis of the changing influence of individual contributions to material degradation. The multi-component phase-field model can be further extended by coupling it through some interface to thermodynamic and kinetic databases to obtain the relevant driving forces.

7 Zusammenfassung

Turbinenschaufeln, die in heißen Regionen von Luft- und Raumfahrt oder in industriellen Gasturbinen benutzt werden, werden normalerweise als gegossene, einzelne kristalline Teile hergestellt. Allerdings ist das Abbauverhalten von den jeweils entstandenen Einzelkristall-Nickelbasis-Superlegierungen immer noch sehr komplex und beinhaltet eine Vielzahl von sehr verschiedenen mikroskopischen Effekten, selbst wenn Korngrenzen ausgeschlossen sind [R. Reed: Cambridge University Press, (2006)]. Einer dieser Effekte ist die diffusionsbegrenzte Vergrößerung der γ' -Ausscheidungen. Langzeit-Alterung oder Kriechbelastung entlang der $\langle 100 \rangle$ kristallographischen Orientierung resultiert in der anisotropen Aufrauung der γ' -Ausscheidungen. Am Ende enthält die Mikrostruktur große, unregelmäßig geformte oder tellerartige Ausscheidungen, die entweder parallel (P-Typ Platten) oder senkrecht (N-Typ Platten) zur Belastungsrichtung ausgerichtet sind. Dieses Verhalten ist nachteilig für die Eigenschaften dieser Stoffe, da ihre vorrangigen Eigenschaften von der Größe, der Morphologie und der Verteilung der γ' -Ausscheidungen ausgehen. Um diese Stoffe effizient zu konzipieren und zu optimieren sollte das Phänomen der Vergrößerung im Detail bekannt sein. Vor diesem Hintergrund ist das allgemeine Ziel dieser Arbeit, einen integrierten rechenstechnischen Ansatz zu entwickeln, mit dem man die morphologische Evolution in Einzelkristall-Nickelbasis-Superlegierungen simulieren kann. In einem ersten Schritt, wurde dazu ein Multikomponenten-Phasenfeldmodell formuliert, welches einem großkanonischen Potential-Formalismus basierend auf dem binären Modell von Plapp [Phys. Rev. E, 84: 031601 (2011)] folgt. Die dafür erforderliche Gesamtheit an thermodynamischen und kinetischen Inputdaten sind aus den kommerziell verfügbaren CALPHAD-Datenbanken TTNi8 und MobNi1 nach einer eigens für diesen Anlass entwickelten Schnittstelle gewonnen worden. Der thermodynamische Ansatz des Modells wurde durch Vergleiche zu ThermoCalc Gleichgewichtsberechnungen und zu DICTRA überprüft. Die mechanischen Effekte sind durch die Allen-Cahn Gleichung basierend auf Steinbach [Physica D, 217, 153 (2006)] und Fleck et al. [Philos. Mag., 90, 265 (2010)] in das Phasenfeldmodell integriert worden. Morphologische Entwicklung und Kinetik in Einzelkristall-Nickelbasis-Superlegierungen wurden untersucht. Um Einblicke in optimierte Legierungen zu erhalten, wurde ein systematisches, rechnerisches Maß in das Modell integriert, mit dem man die Entwicklung von anisotropen Mikrostrukturen beurteilen und verfolgen kann. Zuvor haben Heckl et al. [Metal. and Mater. Trans. A, 41, 202 (2010)], mit Fokus auf dem Erstarrungsverhalten, Ruthenium (Ru) als einen möglichen Kandidaten diskutiert, der Rhenium (Re) für die nächste Generation von Nickelbasis-Superlegierungen ersetzen könnte. Wir führten virtuelle Experimente des Vergrößerungsverhaltens in Legierungen, die Re und Ru enthalten, durch, indem wir Phasenfeldsimulationen angewandt haben. Die Simulationen zeigten, dass die Zersetzung der γ - γ' -Mikrostruktur durch Vergrößerung wesentlich langsamer in Superlegierungen ist, die Re enthalten. Wir beobachteten, dass ein Zuwachs des Re-Inhalts die γ' -Vergrößerungskinetik stark reduziert. Die Simulationsergebnisse zeigen, dass das Re, als das am langsamsten diffundierende Element, das Fortschreiten der Grenzfläche, durch eine Akkumulation des Elementes vor der Phasengrenze ausbremst. Die Tatsache das Re in den Ausscheidungspartikeln nicht löslich ist sowie auch die niedrige Diffusivität können so den Vergrößerungsprozess ausbremsen. Die Experimente erlaubten eine systematische Quantifizierung des relativen Beitrags jedes gelösten Stoffs in einer Superlegierung zu einer Vergrößerung. Dies kann als der erste Schritt zu einem simulationsbasierten Design und der Optimierung von der Zusammensetzung von Legierungen.

8 Appendix A: Model equations and simulation algorithm

Here, we summarize the model that is the basis for the simulation studies in chapters 2-5 of this PhD thesis. The model consists of the phase-field equation (188), the diffusion potential equations (189) and equations for the mechanical equilibrium (190). The evolution equations are coupled to each other via the phase field order parameter $\phi(\vec{x}, t)$. A detailed description of the coupling of the phase field $\phi(\vec{x}, t)$ to the diffusion potential fields μ_i is given in chapter 2. The coupling is further extended in chapter 3 by including elastic effects via the phase field dependent eigenstrain $\varepsilon_{ik}^0(\phi)$ and elastic constants $C_{ikl}(\phi)$. The evolution equations are obtained from a grand-potential functional through variational principles. The explicit phase field equation is given as

$$\begin{aligned} \frac{\partial \phi}{\partial t} = & K \left(\nabla^2 \phi - \frac{2}{\xi^2} g'_{dw}(\phi) \right. \\ & - \frac{\lambda}{3\sigma\xi} h'(\phi) \left(\sum_i \left(\frac{1}{2} \sum_j (\chi_{ij}^\gamma - \chi_{ij}^{\gamma'}) \mu_j - (A_i^\gamma - A_i^{\gamma'}) \right) \mu_i + (B^\gamma - B^{\gamma'}) \right) \\ & \left. - \frac{\lambda}{3\sigma\xi} h'(\phi) \left(\frac{\partial \omega_{el}}{\partial h} \right) \right) \end{aligned} \quad (188)$$

The equations for the evolution of a set of n diffusion potential fields,

$$\frac{\partial \mu_i}{\partial t} = \sum_j D_{ij} (\nabla^2 \mu_j) - \frac{\Delta A_i}{\chi_i} \frac{\partial h}{\partial \phi} \frac{\partial \phi}{\partial t}, \quad (189)$$

The diffusion potential has a source term that includes the phase field term $\partial \phi / \partial t$. The phase field equation (188) and diffusion equations (189) are solved on uniform square grids using explicit finite-difference methods. Second order discretization schemes are used for the spatial derivatives and a first order scheme is used for the time derivatives. The discretization of these evolution equations is given in (201) and (202). Periodic boundary conditions are applied for the fields ϕ and μ_i in all directions. It is always assumed that the system is locally at the interface at equilibrium

$$\frac{\delta \Omega}{\delta u_k} = \sum_k \frac{\partial \sigma_{ik}(\phi)}{\partial x_k} = 0, \quad (190)$$

The mechanical equilibrium is solved using a Jacobi relaxation (Eqs. (191) and (192)) based on the explicit finite difference with elastic variables on a staggered grid. On the staggered grid, eigenstrain and elastic constants are defined on the grid points and the displacement in between them (see Fig 16). Periodic boundary conditions are applied for the u_x and u_y displacement fields in all directions. The mechanical equilibrium (190) is solved independently from the phase field (188) and the set of diffusion equations (189). The mechanical equilibrium is solved first in order to obtain the displacement fields and the corresponding elastic strains. The elastic strains are then used to calculate

the elastic driving force which are then used in Eqs. (188) and (189).

Algorithm based on Jacobi relaxation

We now explain in detail the algorithm used for the simulation studies in this work. The algorithm works as follows:

(1) Initialization of new run: there are two types of initialization modes (i) “reading in” an existing phase field ϕ from old simulations (ii) describing a new phase field configuration.

(2) For the given phase field configuration, the mechanical equilibrium (Eq. (190)) is solved. The mechanical equilibrium is solved iteratively by means of a Jacobi relaxation using a staggered grid (Eqs. (191) and (192)) to obtain the displacement fields u_x and u_y , respectively. At the n time step, the algorithm

(a) calculates the initial solution of

$$\begin{aligned}
\frac{\partial u_x}{\partial t^*} = & \left(C_{11}(i+1, j)([u_x(i+1, j) - u_x(i, j)] - \varepsilon_{xx}^0(i+1, j)) \right. \\
& - C_{11}(i, j)([u_x(i, j) - u_x(i-1, j)] - \varepsilon_{xx}^0(i, j)) \\
& + \lambda(i+1, j)([u_y(i+1, j) - u_y(i+1, j-1)] - \varepsilon_{yy}^0(i+1, j)) \\
& - \lambda(i, j)([u_y(i, j) - u_y(i, j-1)] - \varepsilon_{yy}^0(i, j)) \\
& - \lambda(i+1, j)\varepsilon_{zz}^0(i+1, j) + \lambda(i, j)\varepsilon_{zz}^0(i, j) \\
& + 2\mu(i+1/2, j+1/2)([u_x(i, j+1) - u_x(i, j)] \\
& - \varepsilon_{xy}^0(i+1/2, j+1/2)) - 2\mu(i+1/2, j-1/2)([u_x(i, j) - u_x(i, j-1)] \\
& \left. - \varepsilon_{xy}^0(i+1/2, j-1/2)) \right) / \Delta x^2, \tag{191}
\end{aligned}$$

for the u_x displacement field and

$$\begin{aligned}
\frac{\partial u_y}{\partial t^*} = & \left(\lambda(i, j+1)([u_x(i, j+1) - u_x(i-1, j+1)] - \varepsilon_{xx}^0(i, j+1)) \right. \\
& - \lambda(i, j)([u_x(i, j) - u_x(i-1, j)] - \varepsilon_{xx}^0(i, j)) \\
& + C_{11}(i, j+1)([u_y(i, j+1) - u_y(i, j)] - \varepsilon_{yy}^0(i, j+1)) \\
& - C_{11}(i, j)([u_y(i, j) - u_y(i, j-1)] - \varepsilon_{yy}^0(i, j)) \\
& - \lambda(i, j+1)\varepsilon_{zz}^0(i, j+1) + \lambda(i, j)\varepsilon_{zz}^0(i, j) \\
& + (2\mu(i+1/2, j+1/2)([u_y(i+1, j) - u_y(i, j)] \\
& - \varepsilon_{xy}^0(i+1/2, j+1/2)) - 2\mu(i-1/2, j+1/2)([u_x(i, j) - u_x(i-1, j)] \\
& \left. - \varepsilon_{xy}^0(i-1/2, j+1/2)) \right) / \Delta x^2, \tag{192}
\end{aligned}$$

and for u_y displacement field, where i, j are spatial indices. Here, t^* is the pseudo time.

The relaxation scheme has the property that

$$\frac{\partial u_i}{\partial t^*} = \sum_k \frac{\partial \sigma_{ik}(\phi)}{\partial x_k} = 0, \quad (193)$$

as $t^* \rightarrow \infty$ which satisfies the condition of the mechanical equilibrium.

(b) refines the solution of Eq. (191) and (192) until the residuum is less than a given value η (typically, less than 5×10^{-2} for this work). For the 2D case, we use the L^2 norm in defining the residuum: let the total number of grid points in the x and y -directions be M and N , respectively. The residuum of the given simulation configuration at a given pseudo time t^* is calculated as

$$\text{Residuum} = \int_V dV \left(\sum_i \text{fabs} \frac{\partial u_i}{\partial t^*} \right) \frac{1}{MN}, \quad (194)$$

Since this is an iterative method, it is possible to use the displacements from the previous time step as the starting point and thus expedite the iterative refinement procedure of the solution. Thus, in the implementation, from the second time step onwards, the solution from the previous step is used as the starting point for refinement of the solution.

(3) Once the relaxed displacement fields u_x and u_y are found;

(i) the corresponding elements of the strain tensor at the n time step are calculated as

$$\varepsilon_{xx}^n(i, j) = (u_x^n(i, j) - u_x^n(i - 1, j)) / \Delta x, \quad (195)$$

$$\varepsilon_{yy}^n(i, j) = (u_y^n(i, j) - u_y^n(i, j - 1)) / \Delta x, \quad (196)$$

$$\varepsilon_{xy}^n(i, j) = \frac{1}{2\Delta x} (u_x^n(i, j + 1) - u_x^n(i, j) + u_y^n(i + 1, j) - u_y^n(i, j)). \quad (197)$$

(ii) the elements of the strain tensor ε_{xx} , ε_{yy} and ε_{xy} are then used to calculate the elastic driving force for phase transformation

$$\begin{aligned}
\frac{\partial \omega_{el}}{\partial h} = & 0.5 \Delta C_{11} \left((\varepsilon_{xx}^n(i, j) - [1 - h_{cc}] \varepsilon_{xx}^0) (\varepsilon_{xx}^n(i, j) - [1 - h_{cc}] \varepsilon_{xx}^0) \right. \\
& + (\varepsilon_{yy}^n(i, j) - [1 - h_{cc}] \varepsilon_{yy}^0) (\varepsilon_{yy}^n(i, j) - [1 - h_{cc}] \varepsilon_{yy}^0) \\
& - ([1 - h_{cc}] \varepsilon_{zz}^0) ([1 - h_{cc}] \varepsilon_{zz}^0) \left. \right) + \Delta \lambda \left((\varepsilon_{xx}^n(i, j) - [1 - h_{cc}] \varepsilon_{xx}^0) \right. \\
& (\varepsilon_{yy}^n(i, j) - [1 - h_{cc}] \varepsilon_{yy}^0) + (\varepsilon_{yy}^n(i, j) - [1 - h_{cc}] \varepsilon_{yy}^0) \\
& (- [1 - h_{cc}] \varepsilon_{zz}^0) + (\varepsilon_{xx}^n(i, j) - [1 - h_{cc}] \varepsilon_{xx}^0) (- [1 - h_{cc}] \varepsilon_{zz}^0) \left. \right) \\
& + \Delta \mu \left((\varepsilon_{xy}^n(i, j) - [1 - h_{cc}] \varepsilon_{xy}^0) (\varepsilon_{xy}^n(i, j) - [1 - h_{cc}] \varepsilon_{xy}^0) \right. \\
& - ([1 - h_{cc}] \varepsilon_{xz}^0) ([1 - h_{cc}] \varepsilon_{xz}^0) - ([1 - h_{cc}] \varepsilon_{yz}^0) ([1 - h_{cc}] \varepsilon_{yz}^0) \left. \right) \\
& + (C_{11}(i, j) \left((\varepsilon_{xx}^n(i, j) - [1 - h_{cc}] \varepsilon_{xx}^0) (\varepsilon_{xx}^0) + (\varepsilon_{yy}^n(i, j) - [1 - h_{cc}] \varepsilon_{yy}^0) (\varepsilon_{yy}^0) \right. \\
& - ([1 - h_{cc}] \varepsilon_{zz}^0) (\varepsilon_{zz}^0) \left. \right) + \lambda(i, j) \left((\varepsilon_{xx}^n(i, j) - [1 - h_{cc}] \varepsilon_{xx}^0) (\varepsilon_{yy}^0 + \varepsilon_{zz}^0) \right. \\
& + (\varepsilon_{yy}^n(i, j) - [1 - h_{cc}] \varepsilon_{yy}^0) (\varepsilon_{xx}^0 + \varepsilon_{zz}^0) - ([1 - h_{cc}] \varepsilon_{zz}^0) (\varepsilon_{xx}^0 + \varepsilon_{yy}^0) \left. \right) \\
& + 2\mu(i, j) \left((\varepsilon_{xy}^n(i, j) - [1 - h_{cc}] \varepsilon_{xy}^0) (\varepsilon_{xy}^0) - ([1 - h_{cc}] \varepsilon_{xz}^0) (\varepsilon_{xz}^0) \right. \\
& \left. - ([1 - h_{cc}] \varepsilon_{yz}^0) (\varepsilon_{yz}^0) \right), \tag{198}
\end{aligned}$$

where $\Delta C_{11} = C_{11}^\gamma - C_{11}^{\gamma'}$, $\Delta \lambda = \lambda^\gamma - \lambda^{\gamma'}$, $\Delta \mu = \mu^\gamma - \mu^{\gamma'}$, $h_{cc} = h(\phi(i, j))$ and the discretized elastic constants and eigenstrain are given in Eqs. (137)-(140).

(iii) Using the elastic driving force calculated in (198), the phase field and diffusion potential fields are calculated. The phase field ϕ and diffusion potential fields μ_i are calculated at the time step $n + 1$ as

$$\phi^{n+1}(i, j) = \phi^n(i, j) + \frac{\Delta \phi^n(i, j)}{\Delta t} \Delta t, \tag{199}$$

$$\mu^{n+1}(i, j) = \mu^n(i, j) + \frac{\Delta \mu^n(i, j)}{\Delta t} \Delta t, \tag{200}$$

where

$$\begin{aligned}
\frac{\Delta\phi^n(i, j)}{\Delta t} = & \frac{K}{\Delta x^2} (\phi^n(i+1, j) + \phi^n(i-1, j)) \\
& + \frac{K}{\Delta x^2} (\phi^n(1, j+1) + \phi^n(i, j-1)) \\
& - \frac{K}{\Delta x^2} (4\phi^n(i, j)) - \frac{2}{\xi^2} g'_{dw}(\phi^n) \\
& - \frac{K}{3\sigma\xi} h'(\phi^n) \left(\sum_i \left(\frac{1}{2} \sum_j \Delta\chi_{ij}\mu_j - \Delta A_i \right) \mu_i + \Delta B \right) \\
& - \frac{K}{3\sigma\xi} h'(\phi^n) \left(\frac{\partial\omega_{el}}{\partial h} \right),
\end{aligned} \tag{201}$$

$$\begin{aligned}
\frac{\Delta\mu^n(i, j)}{\Delta t} = & \sum_j \frac{D_{ij}}{\Delta x^2} (\mu^n(i+1, j) + \mu^n(i-1, j)) \\
& + \sum_j \frac{D_{ij}}{\Delta x^2} (\mu^n(1, j+1) + \mu^n(i, j-1)) \\
& - \sum_j \frac{D_{ij}}{\Delta x^2} (4\mu^n(i, j)) - h'(\phi^n) \frac{\Delta A_i}{\chi_i} \frac{\Delta\phi^n(i, j)}{\Delta t}.
\end{aligned} \tag{202}$$

are the spatial derivatives of Eq. (188) and (189), respectively.

(5) The steps (2)-(3) are repeated to move in time for the given number of time steps.

9 Appendix B: Coupling of eigenstrain to concentration fields

We now give a possible extension of the formulation for incorporating misfit strain effects presented in section 3.2.1. The idea here is to extend the **Eigenstrain-Phasefield** coupling (**EP**¹¹) coupling for the inclusion of misfit-strain effects in Eqs. (101-165), to a more physically motivated coupling of the eigenstrain to some weighted average of the local concentrations. Then, by giving the slow diffusing elements - a relatively large weight (because of there relatively large atomic volume), a rather different mechanical background arises, which results from the nontrivial distribution of misfit strains related to the large depletion and accumulation zones of solutes. We denote the possible model

¹¹Eigenstrain-Phasefield coupling

extension as **Eigenstrain-Phasefield-Concentration** coupling (**EPC**¹²),

$$\varepsilon_{jk}^0(\phi, c) = (1 - h(\phi)) \left(\varepsilon_{jk}^0 + \sum_i \frac{\partial \varepsilon_{jk}^{0,\gamma'}}{\partial \mu_i} (\mu_i - \mu_i^{eq}) \right) \quad (203)$$

The coupling is done via the application of Vegard's law, telling that the local equilibrium volume of the elementary cell depends linearly on the local concentration. The Vegard's law is an approximate empirical rule which holds that a linear relation exists, at constant temperature, between the crystal lattice constant of an alloy and the concentrations of the constituent elements [12]. Consistent with Vegard's law, the lattice parameters at room temperature from the γ and γ' lattice parameters that are estimated using the formulas $a^\gamma = a_{Ni} + \sum V_i c_i$ and $a^{\gamma'} = a_{Ni_3Al} + \sum V'_i c_i$ where a_{Ni} and a_{Ni_3Al} are the lattice parameters of pure Ni and pure Ni_3Al , respectively. The values are $a_{Ni} = 3.524$ and $a_{Ni_3Al} = 3.57$. V_i and V'_i are the Vegard's coefficients in pure Ni and Ni_3Al respectively and, c_i and c'_i are the atomic fractions of species i in γ and γ' phases. For a multi-component system, the lattice parameters at room temperature for the precipitate phase is estimated as a sum of the chemical contributions [12]

$$\begin{aligned} a^\gamma(\text{\AA}) &= 3.524 + 0.0196c_{co} + 0.110c_{cr} + 0.478c_{mo} + 0.444c_w + 0.441c_{re} \\ &\quad + 0.3125c_{ru} + 0.179c_{al} + 0.422c_{ti} + 0.7c_{ta} + 0.7c_{Nb}, \end{aligned} \quad (204)$$

$$\begin{aligned} a^{\gamma'}(\text{\AA}) &= 3.57 - 0.04c_{co} - 0.04c_{cr} + 0.208c_{mo} + 0.194c_w + 0.262c_{re} \\ &\quad + 0.133c_{ru} + 0.5c_{ta} + 0.258c_{ti} + 0.46c_{Nb}. \end{aligned} \quad (205)$$

From here, we can calculate the eigenstrain as

$$\varepsilon_{ik}^0 = \frac{a^{\gamma'}}{0.5(a^{\gamma'} + a^\gamma)} \delta_{ij}. \quad (206)$$

We postulate the elastic constants a linear mixture

$$C_{ijkl}(\phi) = h(\phi)C_{ijkl}^\gamma + (1 - h(\phi))C_{ijkl}^{\gamma'}. \quad (207)$$

The elastic energy contribution for this formulation becomes

$$\omega_{el}(\phi, \vec{u}, c) = \frac{1}{2} \sum_{iklm} (\varepsilon_{ij} - \varepsilon_{ij}^0(\phi, c)) C_{ijkl}(\phi) (\varepsilon_{kl} - \varepsilon_{kl}^0(\phi, c)). \quad (208)$$

Inserting Eq. (208) into (92) gives the elastic energy integrated over the whole volume for the EPC coupling. For the EPC coupling, the phase-field equation becomes

¹²Eigenstrain-Phasefield-Concentration coupling

$$\begin{aligned}
\frac{\partial \phi}{\partial t} = & K \left(\nabla^2 \phi - \frac{2}{\xi^2} g'_{dw}(\phi) \right) \\
& - \frac{\lambda}{3\sigma\xi} h'(\phi) \left(\sum_i \left(\frac{1}{2} \sum_j (\chi_{ij}^\gamma - \chi_{ij}^{\gamma'}) \mu_j - (A_i^\gamma - A_i^{\gamma'}) \right) \mu_i + (B^\gamma - B^{\gamma'}) \right) \\
& - \frac{\lambda}{3\sigma\xi} h'(\phi) \left(\sum_{iklm} \left(\Delta C_{iklm} (\varepsilon_{ik} - \varepsilon_{ik}^0(\phi, c)) (\varepsilon_{lm} - \varepsilon_{lm}^0(\phi, c)) \right) \right).
\end{aligned} \tag{209}$$

The resulting diffusion equations have an elastic contribution

$$\begin{aligned}
\frac{\partial \mu_i}{\partial t} = & \sum_j \vec{\nabla} \left(M_{ij} \vec{\nabla} \mu_j \right) - \frac{\Delta A_i}{\chi_i} \frac{\partial h}{\partial \phi} \frac{\partial \phi}{\partial t} \\
& - \sum_j \vec{\nabla} M_{ij} \vec{\nabla} \left(\sum_{iklm} \frac{\partial \varepsilon_{ik}^0(\phi, c)}{\partial \mu_j} \left(C_{iklm}(\phi) [\varepsilon_{lm} - \varepsilon_{lm}^0(\phi, c)] \right) \right).
\end{aligned} \tag{210}$$

We assume that the contribution $\partial \varepsilon_{jk}^{0,ph} / \partial \mu_i$ in (210) for each solute i to correspond as the Vegard's coefficients given in (205). The mechanical equilibrium

$$\sum_k \frac{\partial \sigma_{ik}(\phi, c)}{\partial x_k} = 0. \tag{211}$$

has to be solved for the elastic variables.

Comparison of EP and EPC

In this section, the two methods of coupling mechanical effects in the phase field model are compared; first is the coupling of the eigenstrain to the phase field (Eqs. (101-165)) denoted as EP and second is the extension by coupling to the concentration fields (Eqs. (203-211)) denoted as EPC. The two formulations are compared via simulations of the evolution of a single precipitate in a matrix at 1273.15 K. To test the consistency of the models, simulations are done for four simulation domain sizes denoted as 1 for $251 \times 251 \Delta x$, 2 for $351 \times 351 \Delta x$, 3 for $451 \times 451 \Delta x$ and 4 for $551 \times 551 \Delta x$ where, $\Delta x = 8.6$ nm. The composition of the CMSX4 given in Table 3 is used for the simulations.

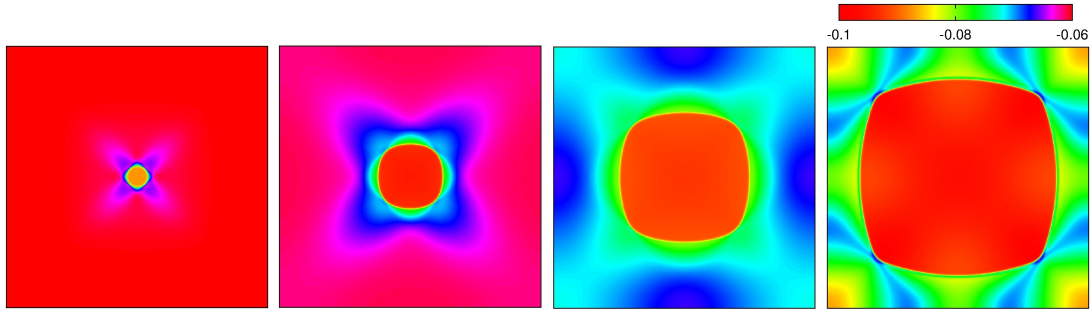


Figure 41: Simulation of γ' -growth using EP (Eqs. (101-165)) and system number 2 of size of $351 \times 351 \Delta x$ at $t=0, 2.5, 4.5$ and 9.0 hr. The color depicts the elastic driving force for phase transformation.

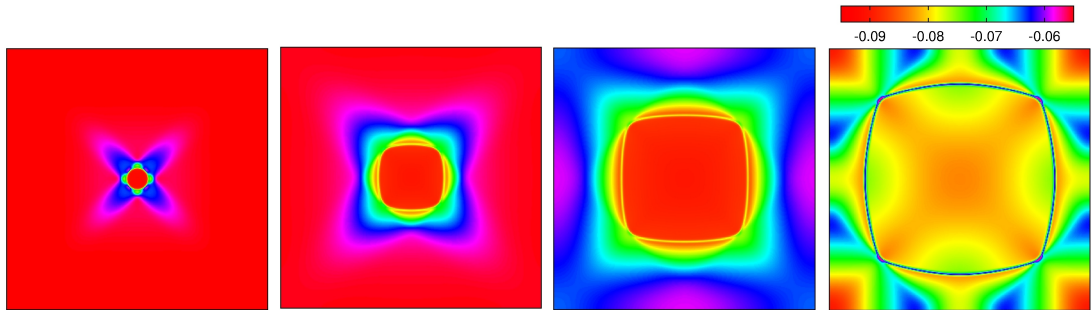


Figure 42: Simulation of γ' -growth using EPC (Eqs. (203-211)) and system number 2 of size of $351 \times 351 \Delta x$ at $t=0, 3.5, 6.5$ and 11 hr.

The Figs 41 and 42 show the evolution of a precipitate using EP and EPC, respectively. In both cases, a sphere to cube transition is observed. The color depicts the elastic driving force for phase transformation. The elastic driving force along the $\langle 111 \rangle$ directions is larger than along the $\langle 100 \rangle$ directions due to the increasing contribution from the coherent strain energy. This leads to anisotropic growth rates along $\langle 111 \rangle$ and $\langle 100 \rangle$ directions which gradually transforms the precipitate morphology from a sphere to a cube. The influence of mechanics on the morphology has been explained in detail in subsection 3.2.2.

To test the consistency of the models, simulations are done using the four aforementioned system sizes. The behavior of γ to γ' transformation does not deviate with a change in domain size. The equilibrium volume fraction and morphologies are similar for different simulation domain sizes. The equilibrium volume fraction obtained by EP is 53% and 49% by EPC. This difference is due to different mechanical effects in the two models. It takes more CPU time for EPC to reach the equilibrium volume fraction than EP. For example, it takes 18 hours for EPC with a simulation domain size of $551 \times 551 \Delta x$ to reach the equilibrium volume fraction as compared to 13.5 hours for EP.

The plot in Fig 43 shows a comparison of the CPU time required to reach the equi-

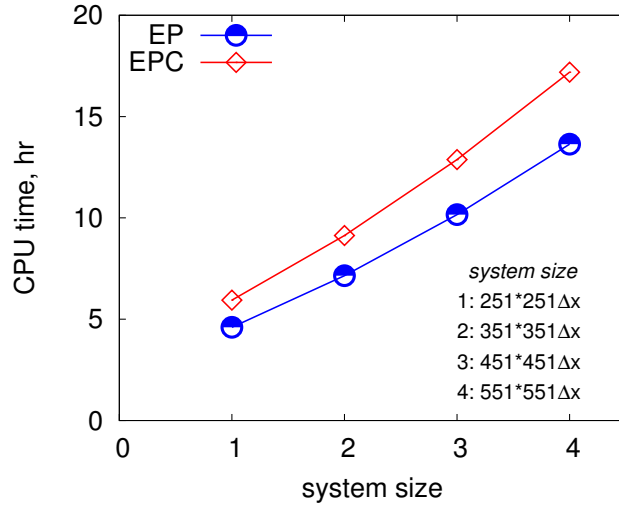


Figure 43: CPU time to reach the equilibrium precipitate volume fraction for different system sizes for EP (in blue) and EPC (in red). The CPU time for any system size to reach equilibrium is faster for EP than EPC.

librium volume fraction for simulations done with EP (in blue) and EPC (in red) for different system sizes. The difference in the CPU time to equilibrium is attributable to the relaxation of the elastic fields. This difference is due to the number of iterations in relaxation loop needed for refinement of the solution to Eq. (193) until $\eta < 5 \times 10^{-2}$. The number of iterations for convergence, depends mainly on the ratio of the elastic constants between phases and to a lesser extent the eigenstrain. The larger the difference the between the elastic constants between the phases, the greater the number of iterations required. Since the coupling of elastic constants is similar for both EP and EPC, the difference in the number iterations for convergence is due to the coupling of the eigenstrain. The different mechanical effects lead to different relaxation times which lead to different CPU times to equilibrium. The similarity in the final stage morphologies motivate the application of the EP formulation in the following. The EPC is suitable for problems where stationary evolution is crucial such as in strongly metastable conditions. Details for such situations need to be elaborated further in more detailed studies.

References

- [1] M. Asta, C. Beckermann, A. Karma, W. Kurz, R. Napolitano, M. Plapp, G. Purdy, M. Rappaz, and R. Trivedi. Solidification microstructures and solid-state parallels: Recent developments, future directions. *Acta Mater.*, 57:941, 2009.
- [2] A. Baldan. Review Progress in Ostwald ripening theories and their applications to nickel-base superalloys Part I: Ostwald ripening theories. *J. Mater. Sci.*, 37:2171, 2002.
- [3] A. Baldan. Review Progress in Ostwald ripening theories and their applications to nickel-base superalloys Part II: Nickel-base superalloys. *J. Mater. Sci.*, 37:2379, 2002.
- [4] W.J. Boettinger, J.A. Warren, C. Beckermann, and A. Karma. Phase-field simulation of solidification. *Annu. Rev. Mat. Res.*, 32:163, 2002.
- [5] G. Boussinot and E. A. Brener. Achieving realistic interface kinetics in phase field models with a diffusional contrast. *Phys. Rev. E Rapid Comm*, 89:060402(R), 2014.
- [6] G. Boussinot, Y. Le Bouar, and A. Finel. Phase field simulations with inhomogeneous elasticity: comparison with an atomistic-scale method and applications to superalloys. *Acta Mater.*, 58:4170, 2010.
- [7] E. A. Brener and G. Boussinot. Kinetic cross coupling between nonconserved and conserved fields in phase field models. *Phys. Rev. E*, 86:060601, 2012.
- [8] I.N. Bronshtein and K.A. Semendyayev. *Handbook of Mathematics*. New York: Springer-Verlag, 3rd edition, 1997.
- [9] I.N. Bronstein, K.A. Semendjaev, G. Musiol, and H. Mühlig. *Taschenbuch der Mathematik (Verlag Harri Deutsch, 2001)*.
- [10] W.K. Burton, N. Cabrera, and F.C. Frank. The growth of crystals and the equilibrium structure of their surfaces. *Philos. Trans. R. Soc. London A*, 243:299–358, 1951.
- [11] G. Caginalp and P.C. Fife. Higher order phase field models and detailed anisotropy. *Phys. Rev. B*, 34:4940, 1986.
- [12] P. Caron. High gamma prime solvus new generation of nickel-based superalloys for single crystal turbine blade applications. *Superalloys*, 2000.
- [13] J. C. Chang and S. M. Allen. Elastic energy changes accompanying γ' -rafting in nickel-base superalloys. *J. Mater. Res.*, 6:1843, 1991.
- [14] J. A. Danzig and M. Rappaz. *Solidification*. EPFL PRes, 2009.

- [15] J.-M. Debievre, A. Karma, F. Celestini, and R. Gurin. Phase-field approach for faceted solidification. *Phys. Rev. E*, 68:041604, 2003.
- [16] J.J. Eggleston, G.B. McFadden, and P.W. Voorhees. A phase-field model for highly anisotropic interfacial energy. *Physica D*, 150:91, 2001.
- [17] H. Emmerich. Advances of and by phase-field modelling in condensed-matter physics. *Adv. Phys.*, 57, 2008.
- [18] M. Fähmann, P. Fratzl, O. Paris, E. Fähmann, , and W.C. Johnson. Influence of coherency stress on microstructural evolution in model Ni-Al-Mo alloys. *Acta Metall. Mater.*, 43:1007, 1995.
- [19] M. Fleck. *Solid-state transformations and crack propagation : a phase field study*. PhD thesis, RWTH Aachen, Institut für Festkörperforschung, Theorie der Strukturbildung, Forschungszentrum Jülich, 2011.
- [20] M. Fleck. *Solid-state transformations and crack propagation : a phase field study*. PhD thesis, RWTH Aachen, Institut für Festkörperforschung, Theorie der Strukturbildung, Forschungszentrum Jülich, 2011.
- [21] M. Fleck, E. A. Brener, R. Spatschek, and B. Eidel. Elastic and plastic effects on solid-state transformations: A phase field study. *Int. J. Mater. Res.*, 101:462, 2010.
- [22] M. Fleck, E. A. Brener, R. Spatschek, and B. Eidel. Elastic and plastic effects on solid-state transformations: A phase field study. *Int. J. Mater. Res.*, 101:462, Apr 2010.
- [23] M. Fleck, C. Hüter, D. Pilipenko, R. Spatschek, and E. A. Brener. Pattern formation during diffusion limited transformations in solids. *Philos. Mag.*, 90:265, 2010.
- [24] M. Fleck, L. Mushongera, D. Pilipenko, K. Ankit, and H. Emmerich. On phase-field modeling with a highly anisotropic interfacial energy. *Eur. Phys. J. Plus*, 126:95, 2011.
- [25] R. Folch and M. Plapp. Quantitative phase-field modeling of two-phase growth. *Phys. Rev. E*, 72:011602, 2005.
- [26] P. Fratzl, O. Penrose, and J.L Lebowitz. Modelling of phase separation in alloys with coherent elastic misfit. *J. Stat. Phys.*, 95, 1999.
- [27] C.L Fu, R Reed, A Janotti, and M Krcmar. On the diffusion of alloying elements in the nickel-base superalloys. *Superalloys*, page 867, 2004.
- [28] A. L. Garcia. *Numerical Methods for Physics*. Prentice Hall, Englewood Cliffs NJ, Mineola, New York 11501, 2nd edition, 2000.
- [29] H. Garcke, B. Nestler, and B. Stoth. On anisotropic order parameter models for multi phase systems and their sharp interface limits. *Physica D*, 115:87, 1998.

- [30] A. Gaubert, Y. Le Bouar, and A. Finel. Coupling phase field and viscoplasticity to study rafting in ni-based superalloys. *Philos. Mag.*, 90:375, 2010.
- [31] A. Gaubert, Y. Le Bouar, and A. Finel. Coupling phase field and viscoplasticity to study rafting in ni-based superalloys. *Philos. Mag.*, 90:375, 2010.
- [32] A.F. Giamei and D.L. Anton. Rhenium additions to a ni-base superalloy : Effects on microstructure. *Metall. Trans. A*, 16A, 1985.
- [33] M. P. Gururajan and T. A. Abinandanan. Phase field study of precipitate rafting under uniaxial stress. *Acta Mater.*, 55:5015, 2007.
- [34] F. Hausser and A. Voigt. A discrete scheme for parametric anisotropic surface diffusion. *J. Sci. Comp*, 30:223235, 2007.
- [35] A. Heckl, R. Rettig, S. Cenanovic, M. Goken, and R.F. Singer. Investigation of the final stages of solidification and eutectic phase formation in Re and Ru containing nickel-base superalloys. *J. Cryst. Growth*, 312(14):2137, 2010.
- [36] A. Heckl, R. Rettig, and R.F. Singer. Solidification characteristics and segregation behavior of nickel-base superalloys in dependence on different rhenium and ruthenium contents. *Metall. Mater. Trans. A*, 41(1):202, 2010.
- [37] S.Y. Hu and L.Q. Chen. A phase-field model for evolving microstructures with strong elastic inhomogeneity. *Acta Mater.*, 49:1879, 2001.
- [38] H.J. Jou, P.H. Leo, and J.S. Lowengrub. Microstructural evolution in inhomogeneous elastic media. *J. Comput. Phys.*, 131:109, 1997.
- [39] M. Kamaraj. Rafting in single crystal Ni-base superalloys - An overview. *Sadhana*, 28:115, 2003.
- [40] A. Karma and W.-J. Rappel. Quantitative phase-field modeling of dendritic growth in two and three dimensions. *Phys. Rev. E*, 57:4323, 1998.
- [41] A.G. Khachaturyan. *Theory of Structural Transformation in Solids*. Dover Publications, Inc., Mineola, New York 11501, 2nd edition, 2008.
- [42] S.G. Kim, W.T. Kim, and T. Suzuki. Phase-field model for binary alloys,. *Phys Rev E*, 60:7186, 1999.
- [43] R. Kobayashi, J.A. Warren, and W.C. Carter. Vector-valued phase field model for crystallization and grain boundary formation. *Physica D*, 119:415, 1998.
- [44] J. Kundin, L. Mushongera, T. Goehler, and H. Emmerich. Phase-field modeling of the γ' -coarsening behaviour in nickel based superalloys. *Acta Mater.*, 60:3758, 2012.
- [45] J. Kundin, J.L.L. Rezende, and H. Emmerich. Phase field modeling of the coarsening in multicomponent systems. *Metal. and Mat. Trans. A*, 45A:1068, 2014.

- [46] J. Kundin and R. Siquieri. Phase-field model for multiphase systems with different thermodynamic factors. *Physica D*, 240:459, 2011.
- [47] J. S. Langer. Instabilities and pattern formation in crystal growth. *Rev. Mod. Phys.*, 52:1, 1980.
- [48] D.Y. Li and L.Q. Chen. Shape evolution and splitting of coherent particles under applied stresses. *Acta Mat.*, 47(1):247, 1999.
- [49] I.M. Lifshitz and V.V. Slyosov. The kinetics of precipitation from supersaturated solid solutions. *J. Phys. Chem Sol*, 19:35, 1961.
- [50] A.C. Lund and P.W. Voorhees. The effects of elastic stress on coarsening in the ni-al system. *Acta Mater.*, 50:2085, 2002.
- [51] N. Ma, Q. Chen, and Y. Wang. Simulating microstructural evolution with high interfacial energy anisotropy using the phase field method. *Scripta Mater.*, 54:1919, 2006.
- [52] G.B. McFadden, A.A. Wheeler, R.J. Braun, S.R. Coriell, and R.F. Sekerka. Phase-field models for anisotropic interfaces. *Phys. Rev. E*, 48:2016, 1993.
- [53] H. Müller-Krumbhaar. *Phasenübergänge: Ordnung und Fluktuationen*, volume 24. Ferienkurs: Magnetismus von Festkörpern und Grenzflächen, chapter 10. Forschungszentrum Jülich - Zentralbibliothek, 1993.
- [54] L. Mushongera, M. Fleck, J. Kundin, Y. Wang, and H. Emmerich. Phase-field simulation of directional γ' -coarsening in commercial single crystal Ni-base superalloys. *Acta Mater.*, 60:3758, 2015.
- [55] F.R.N. Nabarro, C.M. Cress, and P. Kotschy. The thermodynamic driving force for rafting in superalloys. *Acta Mater.*, 44:3189, 1996.
- [56] B. Nestler, F. Wendler, M. Selzer, B. Stinner, and H. Garcke. Phase-field model for multiphase systems with preserved volume fractions. *Phys. Rev. E*, 78:011604, 2008.
- [57] D. Pilipenko, M Fleck, and H. Emmerich. On numerical aspects of phase field fracture modeling. *Eur Phys. J. Plus*, 126, 2011.
- [58] M. Plapp. Unified derivation of phase-field models for alloy solidification from a grand-potential functional. *Phys. Rev. E*, 84:031601, 2011.
- [59] D.A. Porter and K.E. Easterling. *Phase transformations in metals and alloys*. Chapman and Hall, 2nd edition, 1992.
- [60] F. Pyczak, B. Devrient, and H. Mughrabi. The effects of different alloying elements on the thermal expansion coefficients, lattice constants and misfit of nickel-based superalloys investigated by x-ray diffraction. *Proc 10th Int Symp Superalloys*, page 827, 2004.

- [61] F. Pyczak, B. Devrient, F.C. Neuner, and H. Mughrabi. The influence of different alloying elements on the development of the γ/γ' microstructure of nickel-base superalloys during high-temperature annealing and deformation. *Acta Mater.*, 53:3879, 2005.
- [62] M. Rappaz and M.J. Boettinger. On dendritic solidification of multicomponent alloys with unequal liquid diffusion coefficients. *Acta Mater.*, 47:3205, 1999.
- [63] J. Rüsing, N. Wanderka, C. Czubayko, V. Naundorf, D. Mukherki, and J. Rosler. Rhenium distribution in the matrix and near the particle-matrix interface in a model Ni-Al-Ta-Re superalloy. *Scripta Mater.*, 46:235, 2002.
- [64] I. Schmidt and D. Gross. Directional coarsening in Ni-base superalloys: analytical results for an elasticity-based model. *Proc. Roy. Soc., A*, 455:3085, 1999.
- [65] D. Sieborger, H. Knake, and U. Glatzel. Temperature dependence of the elastic moduli of the nickel-base superalloy CMSX-4 and its isolated phases. *Mater. Sci. Eng., A*, 298:26, 2001.
- [66] B. Sonderegger and E. Kozeschnik. Generalized nearest-neighbor broken-bond analysis of randomly oriented coherent interfaces in multicomponent fcc and bcc structures. *Metall. Mater. Trans. A*, 40:499, 2009.
- [67] R. Spatschek, C. Müller-Gugenberger, E. Brenner, and B. Nestler. Phase field modeling of fracture and stress-induced phase transitions. *Phys. Rev. E*, 75:066111, 2007.
- [68] B.J. Spencer. Asymptotic solutions for the equilibrium crystal shape with small corner energy regularization. *Phys. Rev. E*, 69:011603, 2004.
- [69] I. Steinbach and M. Apel. Multiphase model for solid state transformation with elastic strain. *Physica D*, 217, 2006.
- [70] J.E. Taylor and J.W. Cahn. Diffuse interfaces with sharp corners: Phase field models with strongly anisotropic surfaces. *Physica D*, 112:381, 1998.
- [71] S. Torabi, J. Lowengrub, A. Voigt, and S. Wise. A new phase-field model for strongly anisotropic systems. *Proc. R. Soc. A*, 456:1337, 2009.
- [72] Y. Tsukada, T. Koyama, Y. Murata, N. Miura, and Y. Kondo. Estimation of γ/γ' diffusion mobility and three-dimensional phase-field simulation of rafting in a commercial nickel-based superalloy. *Comput. Mater. Sci*, 83:371, 2014.
- [73] A. Volek, F. Pyczak, R.F. Singer, and H. Mughrabi. Partitioning of Re between gamma and gamma prime phase in nickel-base superalloys. *Scripta Mater.*, 52(2):141, 2005.
- [74] P.W. Voorhees. The theory of ostwald ripening. *J. Stat. Phys.*, 38, 1985.

- [75] C.Z. Wagner. Theory of the aging of precipitates by dissolution-precipitation (ostwald ripening). *Electrochem.*, 65:5811, 1961.
- [76] T. Wang, G. Sheng, Z.K. Liu, and L.Q. Chen. Coarsening kinetics of gamma prime precipitates in the Ni-Al-Mo system. *Acta Mater.*, 56:5544, 2008.
- [77] T. Wang, G. Sheng, Z.K. Liu, and L.Q. Chen. Coarsening kinetics of gamma prime precipitates in the Ni-Al-Mo system. *Acta Mater.*, 56:5544, 2008.
- [78] W.Z. Wang, T. Jin, J. L. Liu, X. F. Sun, H.R. Guan, and Z.Q. Hu. Role of Re and Co on microstructures and gamma prime coarsening in single crystal superalloys. *Mater. Sci. Eng., A*, 479:148, 2008.
- [79] Y. Wang, D. Banerjee, C.C. Su, and A.G. Khachaturyan. Field kinetic model and computer simulation of precipitation of l12 ordered intermetallics from f.c.c. solid solution. *Acta Mater.*, 46:2983, 1998.
- [80] Y. Wang and J. Li. Phase field modeling of defects and deformation. *Acta Mater.*, 58:1212, 2010.
- [81] J.A. Warren and W.J. Boettinger. Prediction of dendritic growth and microsegregation patterns in a binary alloy using the phase-field method. *Acta Metall. Mater*, 43:689, 1995.
- [82] Y.H. Wen, J.V. Lill, S.L. Chen, and J.P. Simmons. A ternary phasefield model incorporating commercial CALPHAD software and its application to precipitation in superalloys. *Acta Mat.*, 58:875, 2010.
- [83] A.A. Wheeler. Phase-field theory of edges in an anisotropic crystal. *Proc. Roy. Soc., A*, 462:3363, 2006.
- [84] S. Wise, J. Kim, and J. Lowengrub. Solving the regularized, strongly anisotropic Cahn-Hilliard equation by an adaptive nonlinear multigrid method. *J. Comp. Phys*, 226:414, 2007.
- [85] D.H. Yeon, P.R. Cha, J.H. Kim, M. Grant, and J.K. Yoon. A phase field model for phase transformation in an elastically stressed binary alloy. *Modelling Simul.Mater.Sci.Eng.*, 13:299, 2005.
- [86] K.E. Yoon, R.D. Noebe, and D.N. Siedman. Effect of rhenium addition on the temporal evolution of the nanostructure and chemistry of a model Ni-Cr-Al superalloy II: analysis of coarsening behaviour. *Acta. Mater.*, 55:1159, 2007.
- [87] L. Zhang, I. Steinbach, and Y. Du. Phase-field simulation of diffusion couples in the Ni-Al system. *Int. J. Mater. Res.*, 102:371, 2011.
- [88] N. Zhou, C. Shen, M.J. Mills, and Y. Wang. Phase field modeling of channel dislocation activity and gamma prime rafting in single crystal Ni-Al. *Acta Mater.*, 55:5369, 2007.

- [89] N. Zhou, C. Shen, M.J. Mills, and Y. Wang. Contributions from elastic inhomogeneity and from plasticity to gamma prime rafting in single crystal Ni-Al. *Acta Mater.*, 56:6156, 2008.
- [90] N. Zhou, C. Shen, M.J. Mills, and Y. Wang. Large-scale three dimensional phase field simulation of gamma prime rafting and creep deformation. *Philos. Mag.*, 90:405, 2010.
- [91] N. Zhou, C. Shen, P.M. Sarosi, M.J. Mills, T. Pollock, and Y. Wang. Gamma prime rafting in single crystal blade alloys: a simulation study. *Mater. Sci. Tech*, 25:205, 2009.
- [92] J.Z. Zhu, T. Wang, A.J. Ardell, S.H. Zhou, Z.K. Liu, and L.Q. Chen. Three-dimensional phase field simulations of coarsening kinetics of gamma prime particles in binary Ni-Al alloys. *Acta Mater.*, 52:2837, 2004.

Acknowledgements

First and foremost, I wish to express my sincere gratitude to my advisor, Prof. Dr.-Ing Heike Emmerich who introduced me to the amazing world of materials engineering and supported me through the years. I also wish to thank Dr. Micheal Fleck for his guidance through my research. Not only did I acquire new and valuable knowledge in materials and numerical methods from him, but I also learned methodical ways to tackling problems in research. Special thanks to members of Materials & Process Simulation (MPS) for the stimulating discussions which always inspired me to broaden my knowledge. I would also like to thank Prof. Yunzhi Wang of the Ohio State University for the opportunity to work in his research group. Last but not least, I would like to express my deepest gratitude to my wife Kate, son Tafadzwa, parents, brothers and their spouses for their unconditional love.

This work was supported by the German Research Foundation (DFG) via the Research Training Group 1229 for High Temperature Materials.

List of publications

- L. Mushongera, M. Fleck, J. Kundin, and H. Emmerich. Effect of Re on directional γ' -coarsening in commercial single crystal Ni-base superalloys: A phase field study, *Acta Mater.*, 93:60, 2015
- L. Mushongera, M. Fleck, J. Kundin, F. Querfurth, and H. Emmerich. Phase-field study of anisotropic γ' -coarsening kinetics in Ni-base superalloys with varying Re and Ru contents, *Adv. Eng. Mater.*, DOI: 10.1002/adem.201500168, 2015.
- J. Kundin, L. Mushongera, and H. Emmerich. Phase-field modeling of microstructure formation during rapid solidification in Inconel 718 superalloy, *Acta Mater.* 95, 343, 2015.
- J. Kundin, L. Mushongera, T. Göehler, and H. Emmerich. Phase-field modeling of the gamma prime coarsening behavior in nickel based superalloys. *Acta Mater.*, 60:3758, 2012.
- M. Fleck, L. Mushongera, D. Pilipenko, K. Ankit, and H. Emmerich. On phase-field modeling with a highly anisotropic interfacial energy. *Eur. Phys. J. Plus*, 126:95, 2011.

Curriculum Vitae

Personal

Name: Leslie Tafadzwa Mushongera
Date of birth: 12.12.1980
Nationality: Zimbabwean
Status: Married
Email: lesliemushongera@yahoo.com

Professional & Academic

06.2010 - present: Research Assistant
Lehrstuhl für Material- und Prozesssimulation,
Universität Bayreuth, Germany

06.2013 – 08.2013: Research Scholar
Department of Materials Science and Engineering,
Ohio State University, USA

2008 - 2009: MSc in Mechanical Engineering
Dalarna University, Sweden

2004 - 2008: BEng & Tech in Technological Machinery and Equipment
St Petersburg State Technological University, Russia

Leslie Tafadzwa Mushongera